Title

Timing and Nucleation of Membrane Protein Condensation by Single Peptide-MHC:T Cell Receptor Complex Control Antigen Discrimination

Author

O'Dair, Mark Kendal

Publication Date

2021

Peer reviewed|Thesis/dissertation

Timing and Nucleation of Membrane Protein Condensation by Single Peptide-MHC:T Cell Receptor Complex Control Antigen Discrimination

by

Mark K O'Dair

A dissertation submitted in partial satisfaction of the

requirements for the degree of

Doctor of Philosophy

in

Chemistry

in the

Gradual Division

of the

University of California, Berkeley

Committee in change:

Professor Jay T. Groves, Chair
Professor Alanna Schepartz
Professor David F. Savage

Fall 2021

Abstract

Timing and Nucleation of Membrane Protein Condensation by Single Peptide-MHC:T Cell Receptor Complex Control Antigen Discrimination

by

Mark K O'Dair

Doctor of Philosophy in Chemistry

University of California, Berkeley

Professor Jay T. Groves, Chair

An adaptive immune response begins with a T cell accurately identifying a pathogen-derived peptide loaded into MHC protein on the surface of an antigen presenting cell (APC). T cells engage pMHC with their T cell receptor (TCR) and must discriminate between agonist pMHC molecules, present on APC surfaces at extremely low copy numbers (e.g., tens of molecules), and hundreds to thousands of self pMHC. To be both highly sensitive and precise, T cells have evolved elaborate signaling systems to minimize error. Antigen discrimination is largely based on the binding duration kinetics (dwell time) of pMHC:TCR complexes with agonist pMHC exhibiting long dwell times. LAT is an integral membrane scaffold protein that is intrinsically disordered, and upon its phosphorylation by the kinase Zap70 at multiple tyrosine sites, LAT undergoes a condensation phase transition, being crosslinked by various adaptor and signaling proteins. LAT condensation is a critical feature of productive TCR signaling.

Using single molecule imaging techniques, we observe that an individual LAT condensate is induced by a single pMHC:TCR complex and constitutes a unit of productive TCR signaling. Accumulation of a sufficient number of these condensates is correlated with whole cell activation. LAT condensates form abruptly after an extended delay from the onset of pMHC:TCR binding. Condensate lifetime and size carry no antigen information as they are completely uncorrelated with the dwell time of the originating pMHC:TCR complex. Instead, dwell time correlates with the probability of LAT condensate formation. Condensate delay time is shortened by accelerating the phosphorylation of a unique tyrosine site on LAT, Y136, that exclusively binds the PIP_2 lipase PLCγ1. Perturbing delay time kinetics subsequently alters antigen specificity.

We discover that PLCγ1 plays a novel structural role in nucleating LAT condensates while locked in its autoinhibited conformation by facilitating early crosslinking of LAT. PLCγ1 recruits to LAT coincident with condensate formation, and altering the cytosolic concentration of PLCγ1 modulates condensation delay time and probability, indicating that condensate nucleation is a major kinetic bottleneck step.

Nucleation occurs when PLCγ1 binds LAT at Y136 and an unknown binding partner, through likely SLP-76, with its SH3 domain, suggesting that LAT must be tetravalent for in vivo condensates to form. Thus, PLCγ1 works cooperatively with LAT Y136 phosphorylation to control LAT condensation and antigen discrimination in T cells for accurate immune response.

Dedication

I dedicate this dissertation to all my family and friends who have believed in me, inspired me to believe in myself, and dedicated so much of themselves to bring me to this point. In particular, I dedicate this to my wife Kelli and my children James, Sarah, and Julia for being my constant lighthouse for this great adventure and for their endless love and support. For my parents for raising me with a good moral compass, expecting me to gain a quality education, and giving endless support. For my uncle Joe for spending so much of his time inspiring me to work hard and helping me get to graduate school. For the friends I made in this journey that made it an inspiring and enjoyable chapter of growth. For all that have gone before me that have suffered and sacrifice so much, so I could have what they never could.

Acknowledgements

First and foremost, I acknowledge and thank Jay T. Groves for being my doctorate advisor and for being an outstanding example of an open and critical yet very constructive scientist. I thank all those that helped train me, assisted in performing the experiments and analyses of this work, engaged in countless hours of productive discussion and brainstorming, and whom I consider my friends, including the following: Darren McAffee, Joey DeGrandchamp, Kiera Wilhelm, Albert (Yu-Hsien) Lee, Gabriele Kockelkoren, Eleftheria Kazepidou, Orion Weiner, John Kuriyan, Sungi Kim, Shumpei Morita, Nugent Lew, Neil (Nyuneil) Kim, Summer (Simou) Sun, Laura Nocka, Supraja Chittari, William Huang, Scott Hansen, Jean Chung, Young Kwang Lee, Steven Alvares, Jenny Lin, Shalini Low-Nam, Dongmyung Oh, Emily Laubscher, and many more.

I acknowledge and thank my collaborators that have made my scientific experience truly enriching, including the Orion Weiner, Dimitrios Stamou, and Art Weiss laboratories. I acknowledge Rinat for making and providing bispecific antibodies and BCMA constructs. I thank the Art Weiss lab and Barker Hall stockroom for the Jurkats used in these studies.

I thank the University of California, Berkeley and the Department of Chemistry for providing an excellent space and environment to perform scientific research and to grow intellectually, academically, and professionally. I thank all funding sources and the contributing taxpayers that make this work possible.

I thank the Science Policy Group at Berkeley and the UC Berkeley Graduate Assembly for the opportunity to stretch and grow intellectually and professionally outside of the laboratory. In particular, I thank Juliana Chase for being an excellent friend that anyone could ask for as well as my partner in various science policy projects. I thank Andrew Bremer for pushing me outside of my comfort zone, Danny Broberg for welcoming me into the Science Policy Group, as well as Vetri Velan, Eric Lee, and several others for welcoming and inspiring me to find new ways to use science to benefit humankind. I also thank all my peers and friends from the Graduate Assembly. In total, I thank all who helped me grow in incredible ways and made my graduate experience full of light, laughter, and learning.

Table of Contents

Dedication i

Acknowledgements ii

Table of Contents iii

List of Figures v

List of Abbreviations vii

1 | Introduction 1

2 | Discrete LAT condensates encode antigen information from single TCR binding events 9

Abstract 9

Introduction 10

Single pMHC:TCR binding events trigger discrete LAT condensates 11

LAT condensate size and lifetime are agnostic to pMHC:TCR dwell time 17

Probability of LAT condensate formation increases with pMHC:TCR dwell time 18

LAT condensation occurs after an extended delay 18

Phosphorylation kinetics at the PLCγ1 binding site on LAT control condensation delay time 22

The relation between LAT condensates and T cell activation 22

Discussion 24

Supplementary Figures 27

3 | PLCγ1 non-enzymatically nucleates LAT condensates by specific crosslinking 29

Abstract 29

Introduction 30

Single pMHC:TCR induced PLCγ1 recruitment is contemporaneous with LAT condensation 31

PLCγ1 in vivo abundance modulates the timing and probability of LAT condensation 34

PLCγ1 nucleates LAT condensation by early crosslinking 36

Condensate nucleation requires the PLCγ1 SH3 domain 40

Crosslinking through Y136 is essential for condensation 43

Discussion 47

4 | LAT condensate regulation and using supported bilayers to study immunotherapeutics 53

Abstract 53

Introduction 54

Calcium-induced negative feedback loop on LAT condensation timing 56

LAT condensation in Jurkat T cells 61

Polyclonal T cell activation by bispecific antibody on supported lipid membranes 67

Cortical actin actively accumulates at spontaneous LAT condensates and is depolarized by CD28 triggering 76

5 | Methods and Analyses 82

Methods 82

Quantification and Statistical Analysis 88

6 | References 94

List of Figures

Figure 1-1: T cells probe APCs for agonist pMHC. 2

Figure 1-2: TCR signaling pathway. 3

Figure 1-3: LAT tyrosine architecture and interactions. 4

Figure 1-4: PLCγ1 structure and the tertiary complex. 5

Figure 1-5: Protein-functionalized fluid supported lipid bilayers mimic APC surface. 6

Figure 2-1: Studying single TCR-induced LAT condensates with a supported lipid bilayer platform. 11

Figure 2-2: Detecting single pMHC:TCR complexes by differential diffusion. 12

Figure 2-3: Single pMHC:TCR binding events trigger discrete LAT condensates. 13

Figure 2-4: Performing FRAP on LAT condensates reveals dynamic exchange. 15

Figure 2-5: pMHC:TCR-Induced LAT condensates are not formed from LAT-containing vesicles. 16

Figure 2-6: LAT condensate lifetime and size are uncorrelated with pMHC dwell time. 17

Figure 2-7: pMHC:TCR dwell time correlates with probability of LAT condensate formation. 19

Figure 2-8: LAT condenses after an extended delay and is tuned by Y136 phosphorylation rate. 20

Figure 2-9: Concomitant Grb2-LAT is not due to failed P2A sleavage. 21

Figure 2-10: Modulating LAT condensate delay time alters antigen discrimination thresholds. 23

Figure 2-11: Condensate delay time is not affected by LAT expression level. 27

Figure 2-12: Simulation of LAT timing as a function of antigen density. 28

Figure 3-1: Single pMHC:TCR binding events induce discrete recruitment and clustering of PLCγ1. 32

Figure 3-2: PLCγ1 recruits simultaneous with LAT condensation. 33

Figure 3-3: PLCγ1 overexpression accelerates condensate delay time. 34

Figure 3-4: PLCγ1 knock-down decreases probability of LAT condensation. 36

Figure 3-5: PLCγ1 nucleates LAT condensate by early crosslinking via its SH domains. 38

Figure 3-6: nSH2 domain recruitment is simultaneous with LAT condensation. 40

Figure 3-7: Crystal structure of autoinhibited PLCγ1$_{FL}$ suggests cSH2 is sterically occluded. 41

Figure 3-8: Deletion of SH3 domain inhibits condensation under single molecule stimulation. 42
Figure 3-9: tdSH2(PG) vs tdSH2(GG) construct LAT binding diagram. 44
Figure 3-10: tdSH2(PG) appears similar to PLCγ1$_{FL}$ while tdSH2(GG) fails to robustly cluster. 45
Figure 3-11: tdSH2(PG) facilitates robust LAT condensation but not tdSH2(GG). 46
Figure 3-12: Models of PLCγ1-mediated LAT condensate nucleation with SLP-76. 50
Figure 3-13: LAT valency of four enhances LAT condensation. 52
Figure 4-1: Calcium influences LAT condensate delay time. 57
Figure 4-2: EGTA treatment precludes NFAT translocation. 58
Figure 4-3: Model of calcium-induced negative feedback. 60
Figure 4-4: Basal LAT condensation in Jurkats cells. 62
Figure 4-5: Pervanadate inhibits LAT condensation while increasing tyrosine phosphorylation. 64
Figure 4-6: Typical IgG antibody vs bispecific antibody architecture. 68
Figure 4-7: Height differences between pMHC:TCR complexes and CD45 ectodomain. 69
Figure 4-8: Tuning the intermembrane spacing by increasing ligand height. 70
Figure 4-9: Atto647N-labeled biAb characterization. 71
Figure 4-10: Modulating ligand height exhibits no appreciable effect on cellular activation. 73
Figure 4-11: Bispecific antibody effectively binds and activates polyclonal T cells. 74
Figure 4-12: Csk regulates active Lck population. 76
Figure 4-13: Csk^{AS} inhibition causes pMHC-independent LAT phosphorylation but not Ca^{2+} flux. 77
Figure 4-14: T cells require actin remodeling for activation by 3-IB-PP1. 78
Figure 4-15: Actin accumulation at non-TCR induced LAT condensates is mitigated by CD28. 79
Figure 4-16: Model for actin-mediated regulation of non-TCR-Induced LAT condensates. 81
Figure 5-1: Western blot of PLCγ1 abundance in J.P1 (PLCγ1-knock Down) Jurkats. 88
Figure 5-2: NFAT titration curves based on solution incubation concentration. 92
Figure 5-3: Concentration to density calibration curves for BCMA of different heights. 92

List of Abbreviations

Ab	–	antibody
ADAP	–	adhesion and degranulation-promoting adapter protein
APC	–	antigen presenting cell
ATP	–	adenosine triphosphate
BCMA	–	B cell maturation agent
BiAb	–	bispecific antibody
BSA	–	bovine serum albumin
CAR	–	chimeric antigen receptor
c-Cbl	–	E3 ubiquitin-protein ligase
cSH2	–	C-terminal SH2 domain of PLCγ1
Csk	–	C-terminal Src kinase (Src-family tyrosine kinase)
C2	–	calcium-dependent negative lipid binding domain
CD3	–	cluster of differentiation 3, TCR-associated membrane protein chain containing cytosolic ITAM motifs
CD4	–	cluster of differentiation 4, TCR co-receptor in helper T cells
CD45	–	cluster of differentiation 45, integral membrane PTP type C
CD80	–	cluster of differentiation 80, co-stimulatory receptor binding CD28
CytoD	–	cytochalasin D
DAG	–	diacylglycerol
DLS	–	dynamic light scattering
ERK	–	extracellular-signal-regulated kinase

Fab	–	fragment antigen bind
Gads	–	Grb2-related adaptor (also known as GRAP2) (domain architecture: SH3-SH2-SH3)
GEF	–	guanine nucleotide exchange factor
GGTI	–	geranylgeranyl transferase 1 inhibitor
Grb2	–	growth factor receptor-bound protein 2 (domain architecture: SH3-SH2-SH3)
HBS	–	HEPES buffered saline
His	–	histidine
IL-2	–	interleukin-2
IP_3	–	inositol trisphosphate
ITAM	–	immunoreceptor tyrosine-based activation motif
Itk	–	interleukin-2-inducible T-cell kinase (Tec-family tyrosine kinase)
LAT	–	linker for activation of T cells
Lck	–	lymphocyte-specific protein tyrosine kinase (Src-family tyrosine kinase)
MAPK	–	Mitogen-activated protein kinase 1
MCC	–	moth cytochrome C (strong agonist peptide to AND TCR)
mCh	–	mCherry
mNG	–	mNeonGreen
mSci	–	mScarlet-i
NFAT	–	nuclear factor of activated T-cells
nSH2	–	N-terminal SH2 domain of PLCγ1
PBS	–	phosphate buffered saline
PDF	–	probability density function
PD-1	–	programmed cell death protein 1
PD-L1	–	programmed death ligand 1
perV	–	pervanadate

PIP_2	–	phosphatidylinositol 4,5-bisphosphate
PIP_3	–	phosphatidylinositol (3,4,5)-trisphosphate
$PLC\gamma1_{(FL)}$	–	phospholipase C gamma 1 (full length)
(p)MHC	–	(peptide) major histocompatibility complex
PP2	–	selective Src-family kinase inhibitor
PTP	–	protein tyrosine phosphatase
(p)Tyr/(p)Y	–	(phospho)tyrosine
PH	–	pleckstrin homology domain
PR	–	proline rich region
Rap1	–	Ras-related protein 1
Ras	–	small GTPase from Ras-superfamily
SKAP1	–	Src kinase-associated phosphoprotein 1
SLB	–	supported lipid bilayer
SLP-76	–	lymphocyte cytosolic protein 2 (also known as LCP2)
SHarray	–	nSH2-cSH2-SH3 of PLCγ1
SH2	–	Src Homology Domain 2
SH3	–	Src Homology Domain 3
SOS1/2	–	Son of Sevenless 1/2 (GEF for Ras)
TBS	–	Tris-buffered saline
TCR	–	T Cell Receptor
TCR:CD3	–	complex of the TCR and CD3 chains
tdSH2(GG)	–	SH2(Grb2)-SH2(Grb2)
tdSH2(PG)	–	nSH2(PLCγ1)-SH2(Grb2)
VAMP7	–	vesicle associated membrane protein 7
Vav1	–	Vav guanine nucleotide exchange factor 1
Zap70	–	zeta chain of T cell receptor associated protein kinase 70 (Syk-family tyrosine kinase)

1 | Introduction

To offer its full protection, the immune system must first recognize the presence of disease-causing pathogens in the body, including viral, bacterial, or fungal infections, and initiate proper and specific signaling pathways to induce a productive immune response. The adaptive immune system is one of two major subsystems of the complete immune system found in vertebrates. While the innate immune subsystem responds to a broad category of pathogens in a pre-programmed fashion, the adaptive immune system mounts highly specific responses to each pathogen and retains an immunological memory of the disease to defend against repeated infection. This specific recognition and long-term memory are critical for vaccine function against various diseases. Understanding how the signaling machinery of immune cells discriminates pathogens from non-pathogens on a fundamental, microscopic level is vital to improving the design of therapeutics against disease.

The adaptive immune system operates primarily through T and B lymphocytes, each carrying out specifically evolved roles. $CD4^+$ helper T cells play a critical function in identifying signatures of pathogens, called antigen, and alerting the immune system to mount a specialized response. $CD4^+$ T cells probe the surface of antigen presenting cells (APC), another specialized immune cell, in search of pathogen-derived peptide fragments (i.e., antigen) loaded into the protein major histocompatibility complex (MHC) class II (**Figure 1-1**). A healthy adaptive immune response depends on the ability of T cells to discriminate between non-self, agonist peptide-MHC (pMHC) ligands and the vastly more abundant host-derived self pMHC, both presented on the surface of APCs. It has long been recognized that antigen discrimination is based on the binding kinetics of pMHC to the T cell receptor (TCR), especially the kinetic off-rate (or, equivalently, the mean binding dwell time) (*1*–*3*). This task is complicated by the fact that agonist and self-ligands may differ only slightly in their binding kinetics, requiring a highly precise discrimination mechanism (*4*–*9*). Furthermore, T cells can accurately discriminate pMHC ligands based on only a small number (tens) of individual molecular binding events (*10*–*15*). Precise tuning of the T cell signaling system is crucial for a proper immune response. Mutations

in early signaling proteins that increase TCR sensitivity are associated with autoimmune diseases, while mutations that decrease TCR sensitivity are associated with immunodeficiency (*16*).

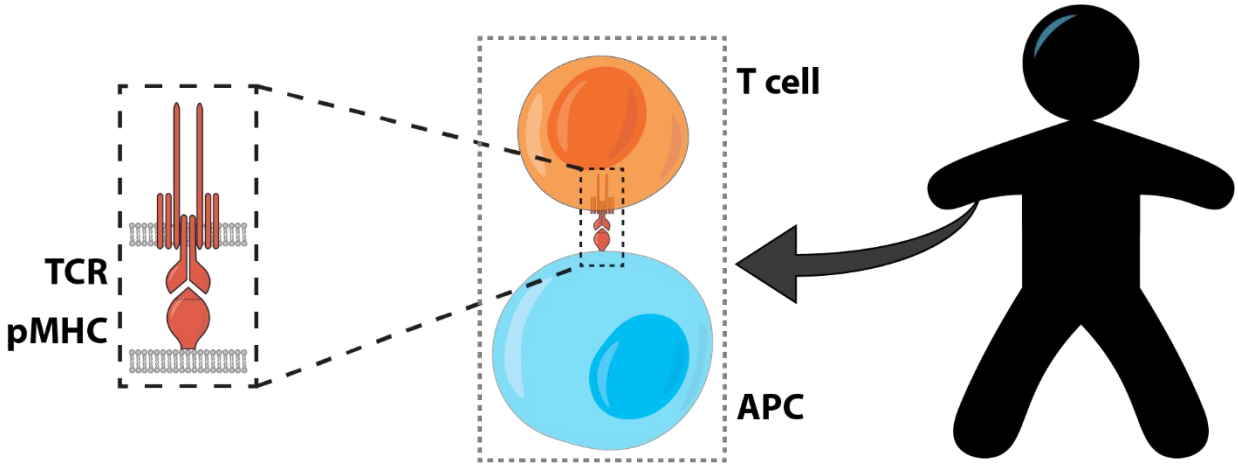

Figure 1-1: T cells probe APCs for agonist pMHC.
T cells use their TCR to probe the surface of APCs in search of MHC loaded with foreign peptide. T cells are capable of detecting single agonist pMHC molecules on the surface of an APC, leading to a global immune response.

Binding of pMHC to TCR initiates a signaling process, the first several steps of which rely on sustained engagement of the pMHC:TCR complex (**Figure 1-2**) (*1*, *17*, *18*). This establishes a kinetic proofreading mechanism, in which only sufficiently long dwelling pMHC:TCR binding events successfully trigger the full downstream signaling response (*8*, *19*). Following the initial formation of the pMHC:TCR complex, immune receptor tyrosine-based activation motifs (ITAMs) on the TCR CD3 chains are phosphorylated by the Src-family tyrosine kinase Lck, creating docking sites for the Syk-family tyrosine kinase Zap70 (*17*, *20*). Zap70 arrives to the TCR in an initially autoinhibited state, but is activated after phosphorylation by Lck, and subsequently phosphorylates substrates, including the scaffolding protein linker for activation of T cells (LAT) (*21*–*24*). A distinctive feature of the TCR signaling mechanism is that LAT is a poor substrate for most tyrosine kinases (*25*) and, thus, relies primarily on Zap70. This requisite series of kinase activation steps, leading up to Zap70 activation at the TCR, constitutes the first stage of kinetic antigen discrimination.

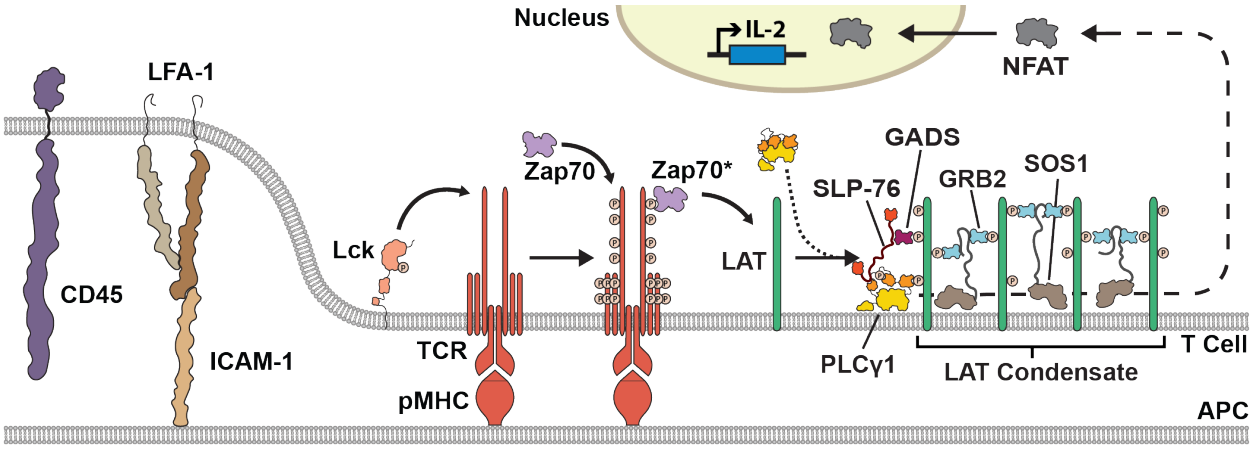

Figure 1-2: TCR signaling pathway.
After pMHC binds to a TCR, the tyrosine kinase Lck phosphorylates ITAMs on the TCR-associated cytoplasmic CD3 chains. Zap70 recruits to phospho-ITAMs, and after its activation by phosphorylation by Lck, Zap70 phosphorylates LAT at four critical tyrosine residues (Y136, Y175, Y195, Y235). Grb2 binds the phospho-LAT and, in association with SOS, clusters LAT on the plasma membrane resulting in a 2D protein condensation phase transition. Grb2 also possesses the ability to homodimerize, providing a SOS-independent mechanism of crosslinking. Gads also binds to phospho-LAT and the adaptor protein SLP-76. PLCγ1 exclusively binds LAT Y136 with its nSH2 domain and simultaneously binds SLP-76 with its SH3 domain. PLCγ1 becomes activated by phosphorylation of Y783 by kinase Itk, which recruits to SLP-76. SOS activates the small GTPase Ras, which signals into the MAPK pathway. Activated PLCγ1 initiates the calcium/NFAT pathway. LFA-1:ICAM:-1 interactions, among other integrin molecules, provide adhesion between T cells and APCs. CD45 is an example of a PTP that exerts constant dephosphorylation pressure on the TCR signaling process.

Under the control of phosphorylation by Zap70, LAT scaffolds a signaling hub from which both the calcium (Ca^{2+}) and MAPK signaling pathways branch (*26*–*29*). LAT is an intrinsically disordered protein anchored to the membrane via a single transmembrane domain and up to two palmitoylations (*30*). LAT contains 9 tyrosine phosphorylation sites, at least 4 of which (Y136, Y175, Y195, Y235 in murine LAT) are utilized in T cell signaling (**Figure 1-3**). The Src-homology 2 (SH2) domain-containing adaptor Grb2 binds to the three C-terminal phosphotyrosine (pTyr) LAT residues (i.e., Y175, Y195, Y235) and subsequently recruits the Ras guanine nucleotide exchange factor (GEF), Son of Sevenless (SOS), which activates Ras and the MAPK pathway. The Grb2-related adapter protein Gads binds to Y175 and Y195, sharing these phosphotyrosine sites with Grb2 (*31*–*33*). Phosphorylation at Y136 on murine LAT (Y132 on human LAT) is unique from the other tyrosine residues in that it generates an exclusive binding site for phospholipase C gamma 1 (PLCγ1) recruitment (*31*, *34*, *35*). PLCγ1 ultimately activates Ca^{2+} signaling. In T cells, MAPK and Ca^{2+} signaling respectively lead to ERK and NFAT nuclear translocation and, along with other transcription factors, ultimately control IL-2 production, T cell differentiation, and other effector functions (*36*). To maintain its high precision, TCR signaling is highly regulated. For instance, various protein tyrosine phosphatases (PTPs), such as CD45, exert constant negative phosphatase pressure (*37*).

It has long been known that the high phosphotyrosine multivalency of LAT enables extended LAT clustering into an elaborate signaling complex when crosslinked by various adaptor proteins (*38*–*41*). More recent studies of LAT, Grb2, and SOS reconstituted on

supported membranes have revealed a two-dimensional protein condensation phase transition governed by tyrosine phosphorylation (*42*, *43*). It was further discovered that formation of this condensate facilitates release of autoinhibition in SOS, thus enabling Ras activation and possibly providing a signal gating function in T cells (*44*).

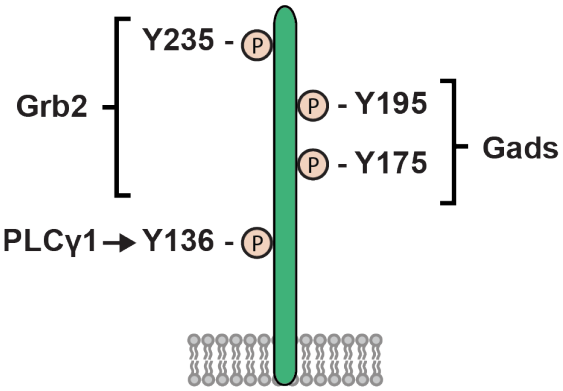

Figure 1-3: LAT tyrosine architecture and interactions.
Zap70 phosphorylates at least four critical tyrosine residues on LAT at Y136, Y175, Y195, and Y235. Grb2 binds the three C-terminal residues (Y175, Y195, Y235) while Gads binds the middle two (Y175 and Y195). The most membrane-proximal of these residues, LAT Y136, is exclusively reserved for PLCγ1 recruitment.

PLCγ1 is a complex and highly regulated multi-domain enzyme whose primary known function is to catalyze the cleavage of PIP_2 lipids into diacylglycerol (DAG) and inositol triphosphate (IP_3). DAG remains embedded in the plasma membrane, acting as a second messenger to recruit and activate downstream signaling proteins such as PKCθ and RasGRP, while soluble IP_3 induces calcium flux into the cytosol (*45*, *46*). To prevent spontaneous calcium flux, PLCγ1 is heavily autoinhibited. Its catalytic TIM barrel, composed of the X- and Y-box, is split by a series of domains that is specific to PLCγ isozymes (*47*). This domain array consists of a split PH domain, two consecutive SH2 domains, followed by an SH3 domain, and constitutes the regulatory unit (**Figure 1-4A**). This regulatory unit folds onto the catalytic and flanking lipid-binding domains, locking PLCγ1 in an autoinhibited conformation by preventing the active site from making productive contact with PIP_2 substrate in the plasma membrane (*48*). In T cells, PLCγ1 binds phosphorylated LAT Y136 with the N-terminal SH2 (nSH2) domain of the regulatory unit. Interestingly, Y136 exhibits the slowest phosphorylation rate of the four LAT tyrosines (*49*–*51*). To maintain the autoinhibited conformation, the C-terminal SH2 (cSH2) domain makes critical interactions with the catalytic unit. With its SH3 domain, PLCγ1 binds SLP-76, which recruits to LAT via Gads (*52*–*54*). Thus, PLCγ1, SLP-76, and Gads form a tertiary complex with LAT (**Figure 1-4B)**. After phosphorylation by Zap70, SLP-76 recruits the Tec-family tyrosine kinase Itk, which phosphorylates PLCγ1 at Y783. Autoinhibition is released when the cSH2 domain releases from the catalytic unit and intramolecularly binds phospho-Y783 (*48*, *55*, *56*). This induces a massive structural rearrangement allowing PLCγ1 to adopt an active conformation. PLCγ1 is indispensable for successful TCR signal propagation as depleting PLCγ1 in Jurkat T cells results in significant loss of IL-2 gene transcription (*57*). While PLCγ1 has primarily been

investigated for its enzymatic function, one recent study suggests PLCγ1 is capable of participating in LAT crosslinking, using the SH domain array of the regulatory unit (*58*).

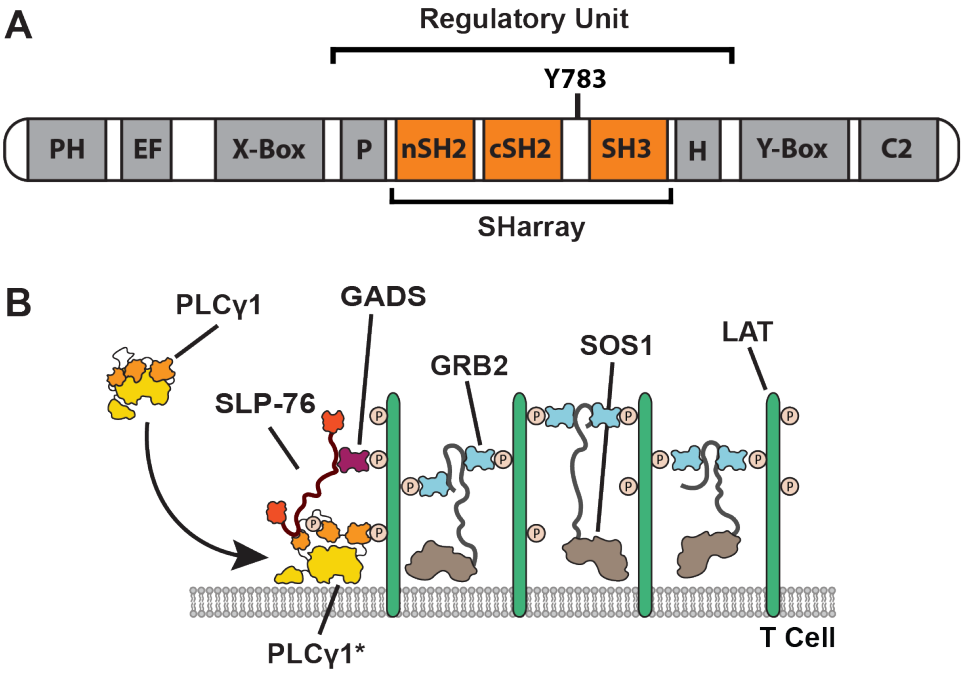

Figure 1-4: PLCγ1 structure and the tertiary complex.
(A) The domain map of PLCγ1. The catalytic TIM barrel of PLCγ1 consists of the X-Box and Y-Box, which are split by a series of domains that are important for regulating PLCγ1 autoinhibition, referred to as the regulator unit. The regulatory unit is made up of a PH domain split by an array of Src homology (SH) domains. This "SHarray" (shown in orange) is composed of two successive SH2 domains (nSH2 and cSH2) followed by an SH3 domain. The X and Y boxes are flanks by lipid binding domains (PH at the N-terminus and C2 at the C-terminus) and a series of EF motifs. (B) PLCγ1 recruits to LAT Y136 via its nSH2 domain and forms a tertiary complex between PLCγ1:SLP-76:Gads:LAT.

It is critical to note that the true physiological context of TCR signaling is a T cell juxtaposed with the surface of an APC that is presenting only tens of agonist pMHC molecules. Fluid supported lipid bilayers (SLBs) provide an excellent platform for studying signaling pathways that occur at the plasma membrane. SLBs can be functionalized with a variety of signaling proteins with control over protein density. Thus, SLBs functionalized with a range of agonist pMHC densities (including low, physiological densities) and native integrin ligands, such as intercellular adhesion molecule-1 (ICAM-1), form a surrogate APC surface for interactions with primary mouse T cells. This experimental platform has long been used in studies of T cell signaling in the context of the immunological synapse (*59*–*68*) and provides an optimal configuration for single molecule imaging by the surface selective imaging technique total internal reflection fluorescence (TIRF) microscopy (*12*–*14*, *57*).

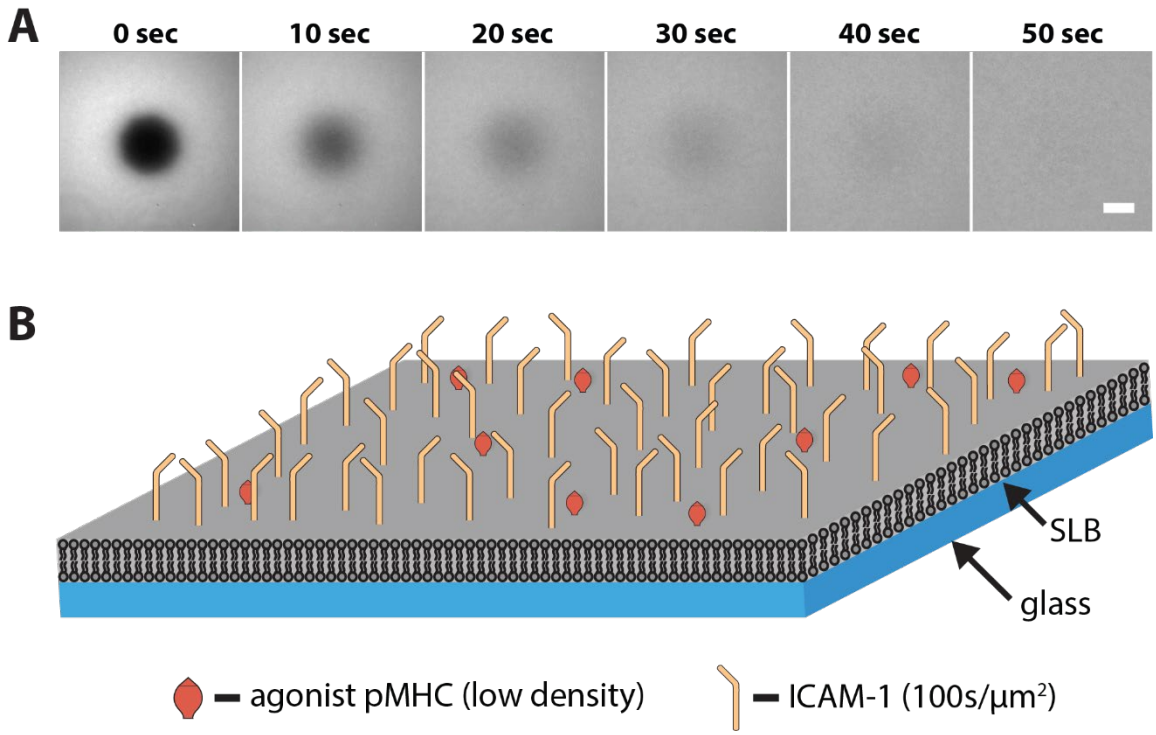

Figure 1-5: Protein-functionalized fluid supported lipid bilayers mimic APC surface.
(A) Fluorescence recovery after photobleaching (FRAP) of a supported lipid membrane. Prior to forming SLBs, lipid vesicles were incubated with the membrane-intercalating dye DiI. A small region of the supported membrane was photobleached with high laser power, after which fluorescent recovery was observed, verifying supported membrane mobility. Bar is 10μm. (B) Schematic of a supported membrane functionalized with APC surface proteins. ICAM-1 is displayed at high density to facilitate natural adhesion with primary T cells. Agonist pMHC is presented at low single molecule densities (e.g., 0.2-0.4 molecules/μm^2). Such SLBs act as a surrogate APC surface.

T cells are highly sensitive to antigen and can robustly activate at agonist pMHC densities around 0.2 molecules/μm^2 (*11*, *12*, *69*). At these densities, pMHC ligands are spaced microns apart and can be readily resolved by single molecule imaging. Using TIRF microscopy, individual pMHC molecules on the supported membrane can be tracked with high spatial (50 nm) and temporal (20 ms) resolution. In these experiments, freely diffusing pMHC molecules exhibit simple two-dimensional Brownian motion on the supported membrane with diffusion coefficients of 0.55 μm^2/s. Nonspecifically immobilized pMHC represent a negligibly small fraction (< 2%). We can directly visualize the TCR-bound state of individual pMHC. When pMHC binds TCR on the T cell, its motion changes dramatically, allowing clear distinction of bound pMHC:TCR complexes from free pMHC ligand (*12*, *13*). Here, we use this single molecule imaging strategy to track the formation, duration, and movement of single pMHC:TCR complexes while simultaneously monitoring LAT condensation or PLCγ1 recruitment (as well as the localization or signaling state of other signaling proteins) in response to a single pMHC:TCR binding event. This unique experimental strategy allows us to map a specific pMHC:TCR binding event to direct signaling outcomes, such as LAT condensation, inside the T cell.

Most experiment work studying T cell signaling has been performed by stimulating T cells with high concentrations of anti-TCR antibody, either in solution or immobilized on glass surfaces (*38*, *41*, *58*, *70*). While such overstimulation studies are highly informative, they should be interpreted judiciously, particularly when studying protein clustering at the plasma membrane. Such methods have the potential to cause artificial protein clustering and skew assembly kinetics. Therefore, it is imperative that T cells are studied under physiological conditions to accurately understand the LAT condensation process. In the work described here, we examine the molecular signaling process from the initial binding of individual pMHC:TCR complexes to the formation of the associated LAT condensate and how signaling proteins such as PLCγ1 play a role in its nucleation and regulation.

Our data reveal that a single pMHC:TCR binding event is sufficient to induce the formation of a LAT condensate on the plasma membrane. These condensates are self-limiting, with condensate size and lifetime being completely uncorrelated with the dwell timing of the originated pMHC:TCR. Thus, once formed, all condensates function independently from the originating binding event. Only the probability of forming a LAT condensate is related to pMHC:TCR binding dwell time. We report quantitative measurements of this probability function that reveal an additional layer of kinetic proofreading, beyond the TCR, that is provided by the LAT condensation phase transition. We report that the delay time from pMHC:TCR binding to initiation of LAT condensation is widely distributed and on the order of tens of seconds. We further observe that condensate delay time is strongly controlled by the phosphorylation of Y136 on LAT, which binds PLCγ1. A LAT mutation that accelerates Y136 phosphorylation (G135D in mouse, G131D in human) (*50*) significantly decreases the LAT delay time while increasing T cell antigen sensitivity, thus suggesting a connection between delay time and antigen discrimination. Whole cell activation, measured by NFAT nuclear translocation, correlates with the number of LAT condensates formed, implying that LAT condensates represent quanta of information in the T cell signaling pathway.

PLCγ1 recruitment and LAT condensation occur simultaneously in response to single pMHC:TCR binding with PLCγ1 recruiting to LAT at the precise moment it begins to condense. LAT condensation is highly dependent on PLCγ1 cellular abundance. Increasing cytosolic PLCγ1 concentration by exogenous overexpression accelerates LAT condensate delay time kinetics. Likewise, decreasing PLCγ1 levels by knock-down reduces the probability of condensation. Together, these data suggest that PLCγ1 nucleates in vivo LAT condensation. Mutation and truncation experiments reveal that nucleation is facilitated by the Src homology (SH) domain array (SHarray) of PLCγ1 while the enzyme is locking in the autoinhibited conformation. This indicates that nucleation occurs by early crosslinking of LAT to form a small LAT nucleate which rapidly grows into a mature condensate. We uncover that this crosslinking must specifically occur through the nSH2 domain binding LAT Y136 and the SH3 domain engaging an unconfirmed binding partner, though likely SLP-76. These results show that PLCγ1 must nucleate LAT since only PLCγ1 binds Y136. Our data also suggest that LAT must be tetravalent, as experiments allowing only trivalent crosslinking produce small, unstable condensates.

Additionally, we present several preliminary results with promising prospects. First, we report that PLCγ1-induced calcium flux appears to activate a negative feedback loop in addition to propagating TCR signaling as a second messenger. Depleting extra- and intra-cellular calcium reservoirs dramatically shortens LAT condensate delay time from single pMHC:TCR binding. We suspect that increasing cytosolic calcium levels through calcium flux produces the inverse effect, constituting a negative feedback loop on subsequent upstream signaling.

We observe that some Jurkat T cell lines produce copious LAT clusters in the absence of TCR stimulation. Inhibiting various biochemical pathways suggests that integrin signaling through ICAM-1:LFA-1 is responsible, at least in part, for the high levels of basal clustering. Interestingly, parental Jurkat lines from other sources exhibit minimal basal LAT clustering, similar to resting primary T cells. This underscores the importance of thoroughly characterizing Jurkat lines and prudently interpreting clustering studies performed in Jurkats.

Utilizing the supported lipid bilayer platform, we characterized an antibody-based cancer immunotherapeutic agent. Bispecific antibodies (biAb) crosslink TCR with target tumor-associated antigen on the surface of a cancer cell. In these experiments, the SLB mimics a tumor cell surface. Our data show that biAb molecules effectively bind and activate T cells, determined by NFAT nuclear translocation, regardless of TCR clonotype. Finally, biAb is capable of effectively activating T cells within a small range of SLB:T cell intermembrane spacing, suggesting it is compatible against a small range of tumor antigens heights.

Finally, we report that cortical actin cytoskeleton actively accumulates at sites of non-TCR induced LAT condensation, presumably to block PLCγ1 access to PIP_2 substrate, as suggested by Csk inhibition studies. This accumulation is mitigated by CD28-induced actin remodeling, producing a uniform actin distribution across the SLB:T cell interface. This implicates that actin provides a safety mechanism, preventing spurious signaling from LAT, which is released with additional signal input.

Collectively, these results reveal that LAT condensation plays a central role in translating antigen information and that many well-known signaling proteins and second messengers play critical auxiliary roles regulating condensate formation, timing, and signaling. Particularly, PLCγ1 functions in a structural capacity to nucleate condensation. LAT condensates contain hundreds of LAT molecules and associated signaling proteins, thus establishing a significant amplification from the single originating pMHC ligand. We propose that the LAT condensation phase transition, and the processes regulating its nucleation, have evolved in TCR signaling as means to achieve the signal amplification and noise suppression necessary for the single molecule ligand sensitivity exhibited by T cells. This is particularly evident considering the unique relationship between PLCγ1 and the unique binding specificity and phosphorylation kinetics of LAT Y136, which provide control over timing and nucleation of LAT condensation and thus antigen discrimination.

2 | Discrete LAT condensates encode antigen information from single TCR binding events

Abstract

LAT assembly into a two-dimensional protein condensate is a prominent feature of antigen discrimination by T cells. Here, we use single molecule imaging techniques to resolve the spatial position and temporal duration of each pMHC:TCR molecular binding event while simultaneously monitoring LAT condensation. Individual binding events are sufficient to trigger LAT condensates, which are self-limiting, and neither their size nor lifetime is correlated with the duration of the originating pMHC:TCR binding event. Only the probability of the LAT condensate forming is related to the pMHC:TCR binding dwell time. LAT condenses abruptly but after an extended delay from the originating binding event. A LAT mutation that accelerates phosphorylation at the PLCγ1 recruitment site shortens the delay time to LAT condensation and alters T cell antigen specificity. These results identify a role for the LAT protein condensation phase transition in setting antigen discrimination thresholds in T cells.

Introduction

LAT condensation phase transition is a critical signaling feature of TCR signaling. LAT is thought to condense through crosslinking provided by Grb2 and SOS (*38*). The SH2 domain of Grb2 binds any of the three C-terminal phosphotyrosine residues on LAT, while its flanking SH3 domains interact with the proline rich regions (PR) of SOS. Thus, a single crosslink takes the form of LAT:Grb2:SOS:Grb2:LAT, with many such interactions resulting in a two-dimensional network. LAT condensates recruit many signaling proteins that activate various signaling pathways. The phase transition properties of condensates likely provide unique advantages in accurately discriminating antigen. Utilizing the supported membrane platform, we investigated the formation of discrete LAT condensates produced from single molecule antigen stimulation.

Our observations reveal that a single pMHC:TCR binding event is sufficient to trigger formation of a condensate containing hundreds of LAT molecules. LAT condensation occurs abruptly, but after an extended delay from the originating binding event, exhibiting signatures of a phase transition. The resulting LAT condensates are self-limiting, and neither their size nor their lifetime is correlated with the duration of the originating pMHC:TCR binding event. Only the probability of forming a LAT condensate is related to pMHC:TCR binding dwell time. We report quantitative measurements of this probability function that reveal extended kinetic discrimination of ligand into the tens of seconds of pMHC:TCR binding dwell times. This represents an additional layer of kinetic proofreading, beyond the TCR, provided by the LAT condensation phase transition. We further observe that a LAT mutation (G135D in mouse, G131D in human), which enhances the kinetics LAT Y136 phosphorylation (the PLCγ1 recruitment site) by Zap70 (*50*), decreases the delay time to LAT condensation and alters T cell antigen specificity. Whole cell activation, measured by NFAT translocation, correlates with the number of LAT condensates formed after exposure to pMHC, suggesting that LAT condensates represent quanta of information in the T cell signaling pathway.

Collectively, these results reveal a central role for LAT condensation in translating antigen information from individual pMHC:TCR to downstream signaling pathways. LAT condensates contain hundreds of LAT molecules and establish significant amplification from the single originating pMHC ligand. Additionally, the self-limiting characteristics of condensates discretize information into a binary output. A pMHC:TCR binding event either produces a LAT condensate or it does not, but once formed, all condensates function independently of the originating binding event. We propose that the LAT condensation phase transition has evolved as means to achieve the amplification and noise suppression necessary for the single molecule ligand sensitivity exhibited by T cells.

Single pMHC:TCR binding events trigger discrete LAT condensates

We characterized LAT condensation in response to single pMHC:TCR binding events using a hybrid live cell-supported membrane experimental platform (*61*, *71–74*) (**Figure 2-1**). The supported lipid bilayer (SLB), consisting primarily of DOPC lipids, is functionalized with pMHC (0-100 molecules/μm^2) and ICAM-1 (200-600 molecules/μm^2), both of which are linked to the membrane via His-tag-protein:Ni-chelating-lipid interactions (*67*, *75*). In the experiments described here, we utilize multicolor TIRF imaging to track LAT condensation at the plasma membrane in response to T cell engagement with pMHC and ICAM-1 functionalized SLBs. Experiments are generally performed using primary T cells harvested from mice with transgenic TCR(AND) (*76*). Splenocytes from the TCR(AND) mice, hemizygous for H2^k, were pulsed with 1 μM MCC peptide and cultured with the T cells for two days. The T cell blasts were treated with IL-2 from the day after harvest to the fifth day after harvest, at which point the cells were used in experiments. Fluorescent fusion proteins of interest were expressed using the PLAT-E retroviral platform (*77*). For experiments requiring expression of two different fluorescent fusion proteins, we utilized a self-cleaving P2A peptide (*78*). RICM imaging monitored the supported membrane:T cell contact independently from the fluorescence channels (*79*). Epifluorescence was used for imagining the cell interior.

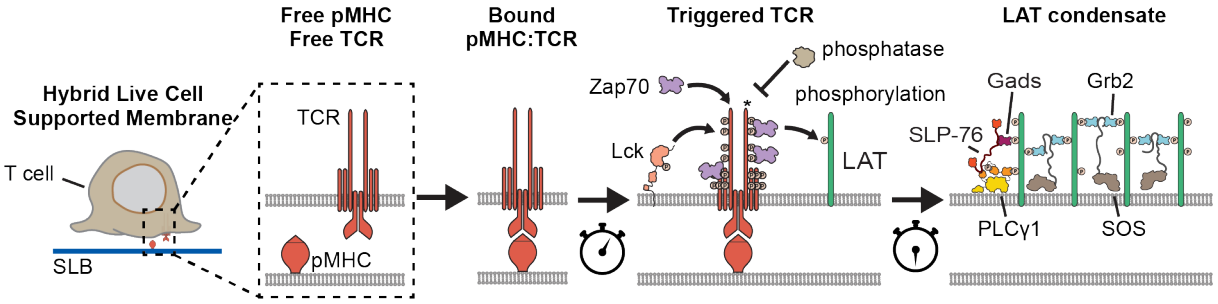

Figure 2-1: Studying single TCR-induced LAT condensates with a supported lipid bilayer platform. *After the plasma membrane of the T cell interfaces with the supported lipid bilayer, T cell signaling occurs downstream of pMHC:TCR binding. Primary observables include single pMHC:TCR binding/unbinding and LAT condensation in the T cell plasma membrane after a series of kinetic steps.*

TIRF microscopy of the SLB:live cell interface provides robust imaging capabilities down to the single molecule level (*80–82*). At low agonist pMHC densities (0.1 – 0.4 molecules/μm^2), individual pMHC molecules are resolvable and can be tracked undergoing free lateral Brownian motion in the membrane. When pMHC binds to a TCR on a T cell, its diffusion changes dramatically to conform with the much slower movement of the TCR. Under long exposure times (500 ms) and low excitation powers (0.4 mW/cm^2), individual pMHC:TCR complexes appear as well defined spots, whereas free pMHC moves too quickly to be clearly resolved and appears as a diffuse fluorescent background (**Figure 2-2A-B**). This imaging method offers selective tracking of pMHC:TCR complexes in living cells with a time resolution of ≈1 sec. and spatial resolution of ≈ 0.5 μm (*12*, *13*).

Trajectories for each individual pMHC:TCR complex were tracked to measure the specific pMHC:TCR binding dwell time, their spatial movement within the T cell membrane, and their direct cellular response as measured by fluorescent fusion proteins of interest.

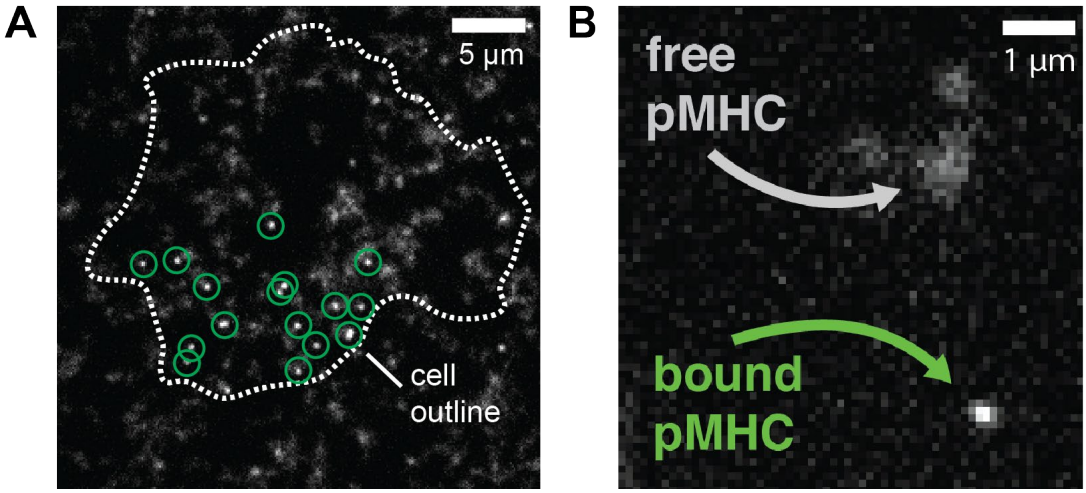

Figure 2-2: Detecting single pMHC:TCR complexes by differential diffusion.
(A) Detection of pMHC:TCR binding events. TIRF image of MCC(Atto647)-MHC on a supported membrane imaged at 500 ms. A primary T cell (while dotted outline) interacts with a supported lipid bilayer containing MCC-MHC and ICAM-1. Long imaging exposure time allows detection and distinction of slow diffusing TCR-bound pMHC, which appear as localized bright spots (circled in green), and freely diffusing unbound pMHC, seen as diffuse fluorescence. (B) Zoom-in of MCC(Atto647)-MHC on a supported membrane imaged by TIRF with a 500 ms exposure. This exemplifies the distinction between the diffuse fluorescence of unbound, "free" pMHC (top) and the localized fluorescence of bound pMHC (bottom).

Representative TIRF images of LAT-EGFP expressed in primary T cells interacting with stimulatory bilayers presenting various densities of agonist pMHC are illustrated in **Figure 2-3A**. LAT condensation is readily visible as localized increases in LAT density, and corresponding time traces of the overall extent of LAT condensation are plotted in **Figure 2-3B**. At high agonist pMHC densities (10-40 molecules/μm^2), LAT condensation is observed throughout the SLB:T cell interface within seconds of touchdown. This is consistent with numerous reports of LAT clustering and condensation in T cell interactions with APCs displaying high agonist pMHC density (*59*, *83–85*) as well as T cells interacting with activating anti-TCR antibody coated surfaces (*41*, *70*). At these high antigen densities, however, LAT phosphorylation and subsequent condensation are driven by multiple TCR activation events, which are also intrinsically unsynchronized in time and superimposed in the images. The observed LAT condensation cannot be directly mapped to the individual pMHC:TCR binding events that triggered it, and much information is lost. At lower agonist pMHC densities (**Figure 2-3A**, middle panel), the overall amount of LAT condensation is significantly lower; however, similarly high local densities of LAT are still observed to form stochastically and widely distributed throughout the interface. Although the total amount of LAT condensation remains low, and appears to form on a much longer timescale, T cells still activate robustly at these pMHC densities (*10–12*, *69*). In control experiments with zero pMHC in the membrane (**Figure 2-3A**, right panel), very few LAT condensates are observed, and T cells do not activate.

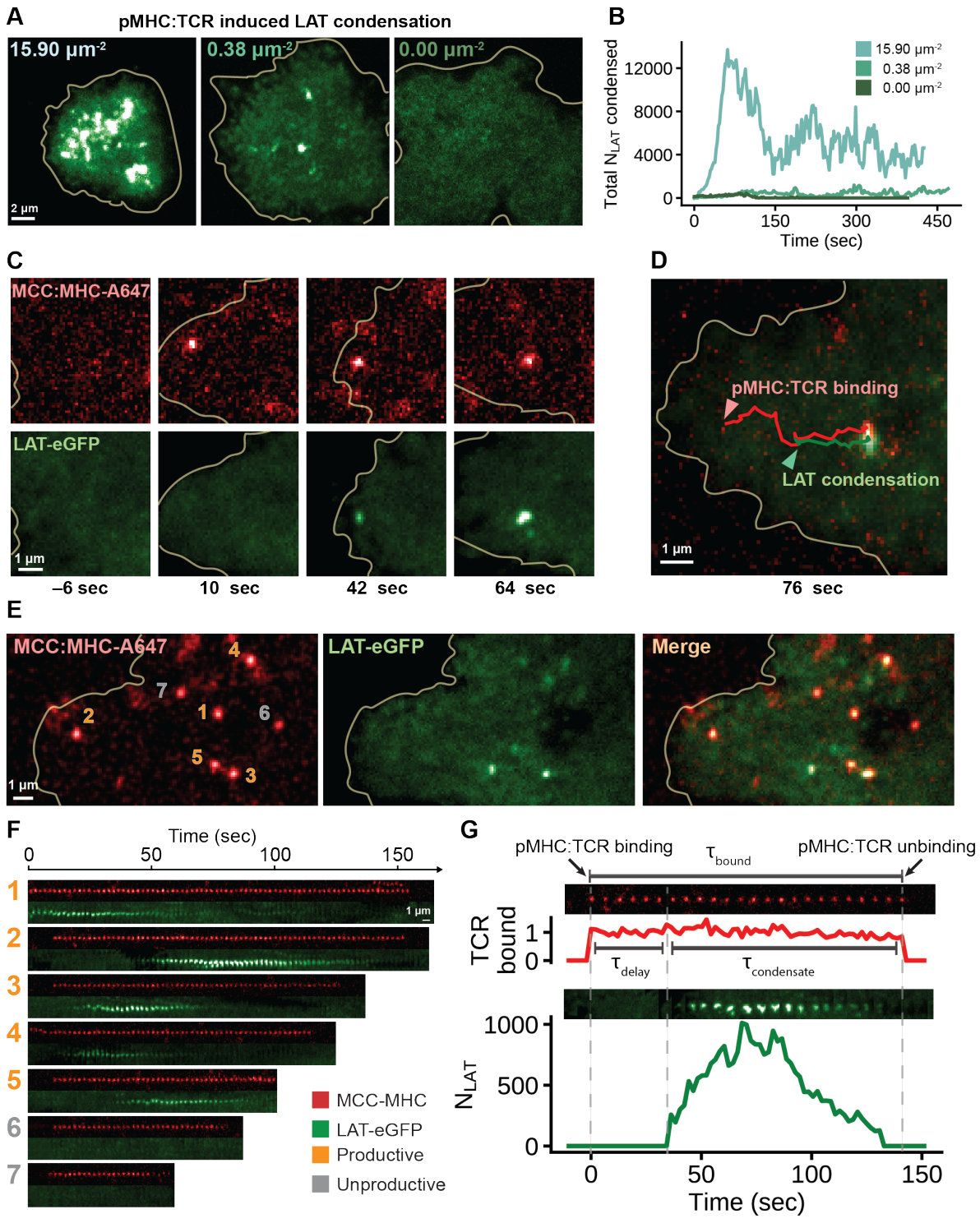

Figure 2-3: Single pMHC:TCR binding events trigger discrete LAT condensates.
(A) TIRF images of primary murine CD4⁺ T cells expressing AND TCR and LAT-EGFP deposited onto SLBs with varying densities of MCC(Atto647)-MHC. (B) The amount of condensed LAT through time for cells in (A) was calculated by dividing the total condensed area intensity by the intensity of single LAT-EGFP molecules, see Methods. (C) Representative image of a spatially isolated pMHC:TCR binding event that maintains >1 μm distance from any other binding event and produces a highly localized LAT condensate within 50 nm at onset of condensation. Time stamps are relative to the moment of pMHC:TCR binding. (D)

Overlay of MCC(Atto647)-MHC and LAT-EGFP channels showing the co-localized trajectories of both the pMHC:TCR binding event and its associated LAT condensate, as well as the centripetal motion of both towards the center of the cell. (E) A wider view of the T cell shows a constellation of binding events spread out in space. Separate binding events are enumerated. (F) Temporal sequence of images for the binding events in (E). Binding events visible in the first acquisition frame are not considered for subsequent analyses. Some binding events are productive, while others fail to produce a localized LAT condensate. (G) Intensity traces of productive binding events displaying several quantities - the number of condensed LAT produced (N_{LAT}), the delay time until LAT condensation (τ_{delay}), as well as the lifetime of the LAT condensate ($\tau_{condensate}$).

At low pMHC densities (0.1-0.4 molecules/μm^2), individual pMHC:TCR binding events are spaced microns apart and can remain distinctly separated for the entire lifetime of the bound complex (**Figure 2-3E**, left panel). These individual binding events can induce discrete LAT condensation. A time sequence of images illustrating the binding and movement of a single pMHC:TCR complex, along with the corresponding LAT condensate it formed, are illustrated in **Figure 2-3C**. LAT condensation begins within tens of nanometers of the originating pMHC:TCR complex, and condensates generally remain within a 100–300 nm neighborhood of the complex as both undergo colocalized transport towards the center of the SLB:T cell interface (**Figure 2-3D**). This retrograde transport of single pMHC:TCR complexes with their corresponding LAT condensate is very similar to the retrograde transport of TCR clusters that occurs at high pMHC density (*68*, *86*–*88*). This method is also sensitive enough to distinguish very rare putative pMHC dimer binding from the predominant monomer pMHC binding, which we focus on in this study. Over the entire cell interface, multiple such pMHC:TCR binding events and corresponding LAT condensates can be observed (**Figure 2-3E**). The LAT condensates form quickly and ultimately dissipate, generally independently of each other. Usually, only a few LAT condensates exist at any one moment in time. A collection of time sequence images tracking pMHC:TCR binding, along with the corresponding LAT condensate formation and subsequent dissipation, for the seven binding events from the cell pictured in **Figure 2-3E** are shown in **Figure 2-3F**. Note that two binding events failed to produce LAT condensates in this particular set.

Detailed analysis of a productive binding event is presented in **Figure 2-3G**, illustrating the wealth of information that is gathered from each such event. The total pMHC:TCR binding dwell time (τ_{bound}) is observed in the top (red) sequence of images. The sequence of images below (green) tracks the corresponding LAT condensate, with a calibrated trace plotting the number of LAT molecules in the condensate through time. LAT condensation occurs abruptly, but after a relatively long delay time ($\approx$ 40 sec. delay in this trace; mean delay: $\langle\tau_{\mathrm{delay}}\rangle \approx 23.2$ sec.). The LAT condensates are self-limiting and, as seen here, can dissipate prior to the pMHC:TCR complex dissociating. Fluorescence recovery after photobleaching measurements on the LAT condensates (**Figure 2-4**) indicate they are highly dynamic, with individual LAT molecules turning over throughout the lifetime of the condensate (see *FRAP of LAT condensates* in Methods). We determined the total number of LAT molecules in pMHC:TCR-induced condensates using quantitative immunoblots, FACS, and quantitative fluorescence imaging (see Methods).

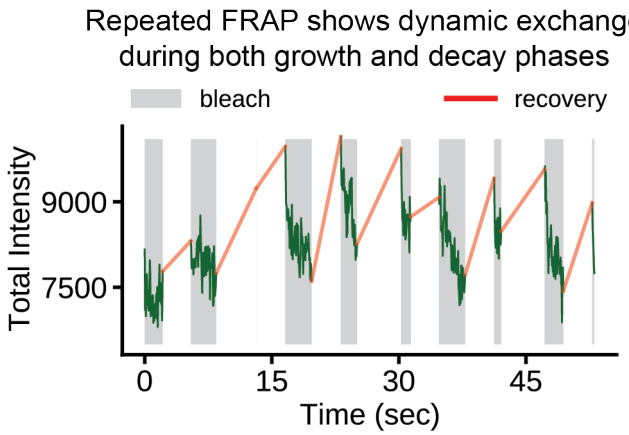

Figure 2-4: Performing FRAP on LAT condensates reveals dynamic exchange.
Periodic bleaching of the LAT condensate shows rapid recovery throughout the lifetime of the LAT condensate.

The background distribution of LAT in primary T cell membranes is extremely uniform (as seen in **Figures 2-3A** and **2-3C-E**). Individual pMHC:TCR binding events produce distinctly resolved LAT condensates against this smooth background. Experimental examination reveals that these pMHC:TCR-induced LAT condensates form from plasma membrane-associated LAT and are distinct, in both composition and their association with agonist pMHC, from LAT containing-vesicles arriving at the plasma membrane from the cytosol, a small number of which can also be observed. Delivery of cytosolic LAT to the plasma membrane has been reported via VAMP7-associated vesicles (*83*, *89*). To confirm that pMHC:TCR-induced condensates studied here are distinct, we performed experiments on T cells simultaneously expressing LAT-mScarleti (LAT-mSci) and mNeonGreen-VAMP7 (mNG-VAMP7) (i.e. LAT-mSci-P2A-mNG-VAMP7). LAT condensates associated with pMHC:TCR binding events did not show any appreciable inclusion of VAMP7 (**Figure 2-5A**). However, at later time points after cell contact with pMHC-containing SLBs, some dense features of LAT did appear in TIRF images that were not associated with pMHC:TCR but contained VAMP7 (**Figure 2-5B**). Some LAT features were also observed that lacked VAMP7 and were also not associated with detectable pMHC:TCR (**Figure 2-5C**). These possibly correspond to pMHC:TCR-induced condensates in which the fluorescence label on pMHC has been bleached or some other form of LAT clustering such as an ICAM-1:LFA-1 mediated mechanism. The immune adaptor protein SKAP1 has been identified as a potential marker for ICAM-1:LFA-1 induced LAT clusters (*90*). While we observe SKAP1 present in all condensates (observed by expressing of the construct MSCV-LAT-mSci-P2A-SKAP1-mNG), in many cases SKAP1 clusters at the membrane prior to LAT in non-TCR induced clusters (**Figure 2-5D**), suggesting that some “orphan” condensates are nucleated by an entirely different mechanism (e.g., ICAM-1:LFA-1 signaling). In this study, we focus on LAT condensates that are directly triggered by pMHC:TCR binding events. We also note that Jurkat T cells can exhibit greater variability and can have significant levels of LAT condensation in the absence of any TCR activation (**Figure 2-4A**). LAT condensation in Jurkat T cells is discussed in greater detail in Chapter 4.

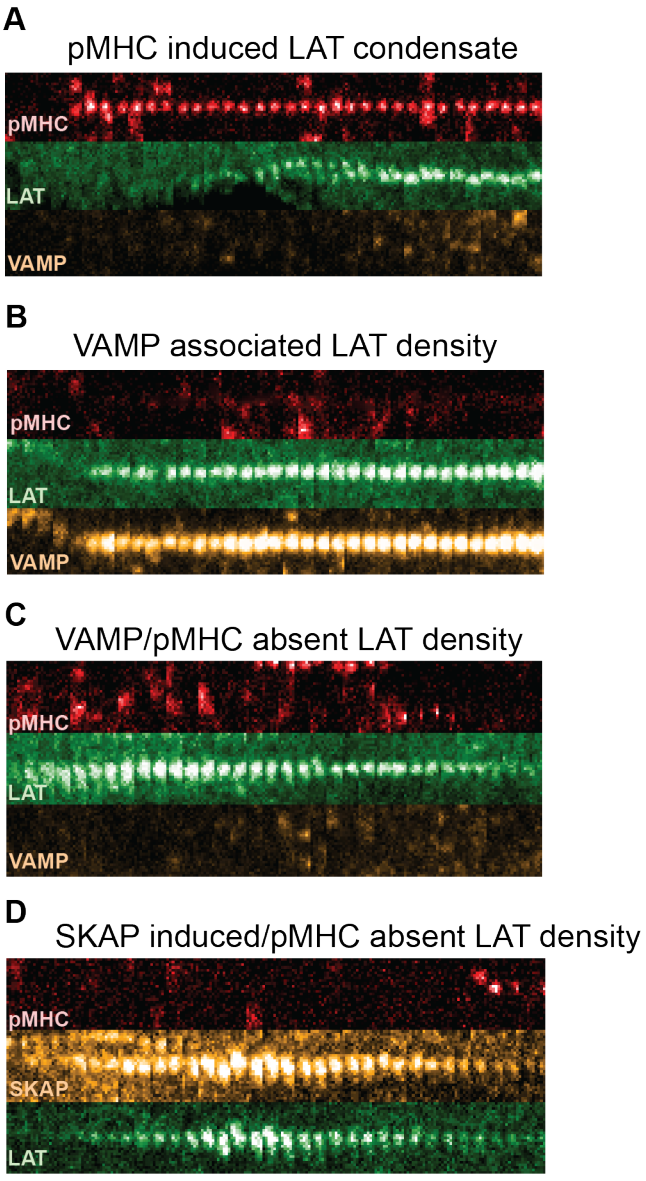

Figure 2-5: pMHC:TCR-Induced LAT condensates are not formed from LAT-containing vesicles. *(A) Condensation of LAT was observed in response to pMHC:TCR binding events, but lacked any notable VAMP dynamics. (B) Some VAMP-associated densities of LAT were visible at the membrane. Mostly, these failed to correspond to any MCC-MHC signal. (C) There remain some LAT clustering features at the membrane that are either associated with dark MCC-MHC binding or have an alternate origin, independent of VAMP and pMHC. (D) In clusters with no apparent pMHC binding event, SKAP1 begins to cluster before LAT.*

LAT condensate size and lifetime are agnostic to pMHC:TCR dwell time

We assessed whether condensate size (i.e., number of incorporated LAT molecules) or lifetime possess information of the originating pMHC antigen and is, therefore, important for discrimination. We measured condensate properties from many TCR-induced LAT condensation events (e.g., **Figure 2-3G**) from many cells to determine if single pMHC:TCR dwell time kinetics is encoded in condensate size or lifetime. As seen in **Figure 2-6**, LAT condensate lifetime and maximum size are completely uncorrelated with pMHC:TCR dwell time. This result indicates that after condensates form, they carry no antigen information and act independently of the inducing pMHC ligand. Therefore, antigen information is contained in the steps preceding, and perhaps including, condensate nucleation.

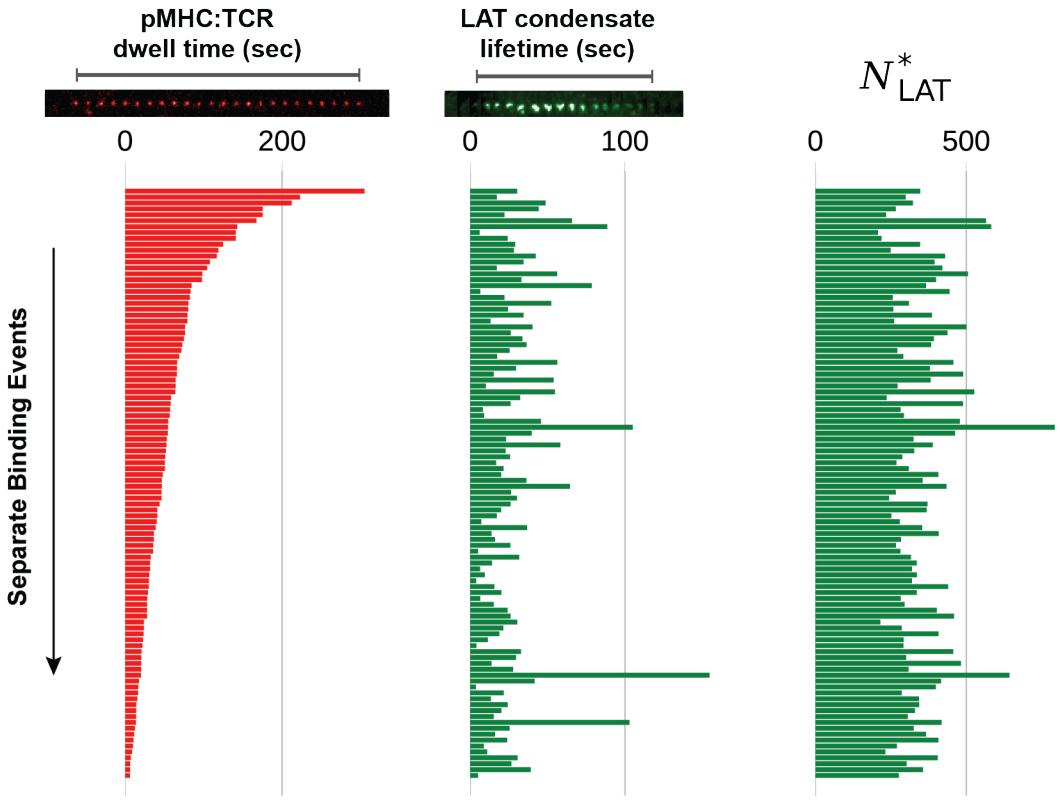

Figure 2-6: LAT condensate lifetime and size are uncorrelated with pMHC dwell time.
Three bar plots showing the lack of correlation between pMHC:TCR dwell time (left) with either the LAT condensate lifetime (middle) or the number of LAT within its associated condensate (right). N^*_{LAT}, as computed above, is rescaled using an estimate for physiological LAT density of $601 \pm 150\ (SD)/\mu m^2$.

Probability of LAT condensate formation increases with pMHC:TCR dwell time

Binding events between pMHC and TCR either resulted in LAT condensation or did not, indicating that TCR signaling to LAT is binary (**Figure 2-3F**). By binning the dwell times of productive (i.e., that produced a LAT condensate) and unproductive pMHC:TCR binding events as shown in **Figure 2-7** (top panel for MCC-MHC), and dividing the number of productive events by the total number of pMHC:TCR binding events within each dwell time bin, we can calculate the single TCR input-response function (**Figure 2-7**, bottom panel). This ability has never been possible before. The probability function in **Figure 2-7** (bottom panel) demonstrates that, while condensate size and lifetime are independent of pMHC:TCR binding duration, the probability of LAT condensate formation is related to pMHC:TCR dwell time. This is true whether triggering the TCR with the strong agonist MCC peptide ($\tau_{bound} \approx$ 48 seconds) or the weaker agonist T102S peptide ($\tau_{bound} \approx$ 10 seconds) (**Figure 2-7**, middle and bottom panel). Interestingly, the input-response probability function is identical for MCC and T102S, indicating that this is an intrinsic property of the TCR and not the ligand. It is simply more difficult for short dwelling pMHC ligands, such as T102S, to reach high probability of LAT condensation. These data reveal that kinetic discrimination of antigen extends into the tens of seconds of binding dwell times, beyond the TCR, provided by the LAT condensation. Interestingly, the probability function plateaus far short of 100% (~25% for the TCR(AND)).

LAT condensation occurs after an extended delay

For productive binding events, LAT condensation occurs after a notably long delay from the originating pMHC:TCR binding event. When the LAT condensation begins, the growth rate rapidly transitions from zero to rates near 100 LAT molecules per second (see **Figures 2-3G**), and this growth is sustained as hundreds of LAT molecules join the condensate until a maximum is reached. The abrupt transition to LAT condensation establishes a well-defined delay time (τ_{delay}) between the originating pMHC:TCR binding event and the beginning of LAT condensation (**Figure 2-8A**). A histogram of 385 delay times measured from productive MCC-MHC:TCR binding events reveal that condensation occurs after a surprisingly long delay, displaying a broad distribution, with the rise and fall shape of a gamma distribution, and a mean delay time of $23.2 \pm 1.6\ (\mathrm{SE})$ seconds (**Figure 2-8B**). These measurements have a time resolution of 2 seconds, which is set by the time-lapse used in the image sequences. Control experiments confirm that the identity of the fluorophore on the LAT has no effect on LAT condensation, nor was the delay time affected by LAT expression levels (**Figure 2-11**).

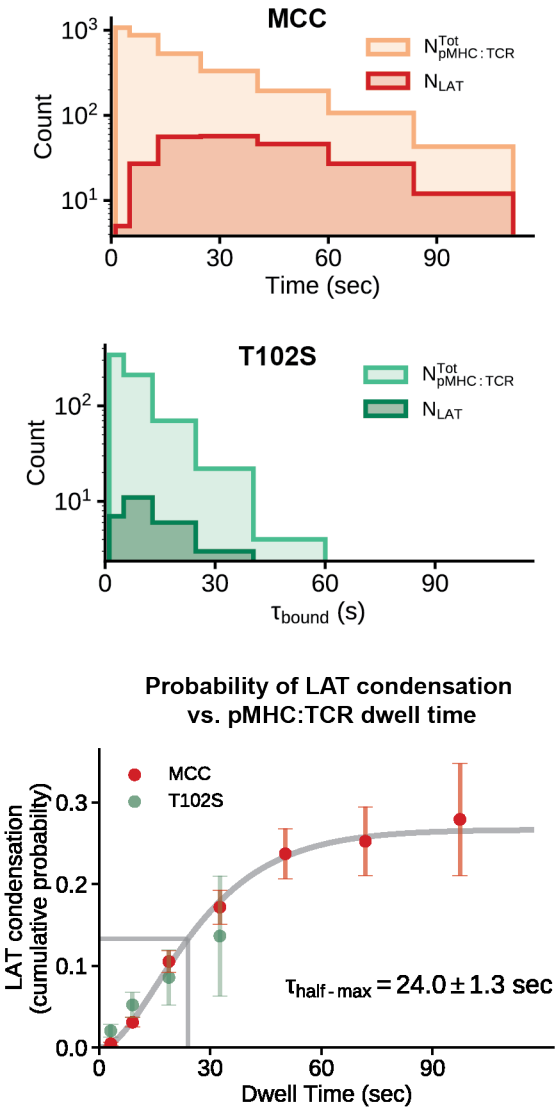

Figure 2-7: pMHC:TCR dwell time correlates with probability of LAT condensate formation. *(Top) Histograms of the observed MCC-MHC:TCR dwell time distribution (orange) and the productive dwell time distribution (red). The former is fit to an exponential distribution with a decay rate of* $k_{obs} = k_{off} + k_{bleach} = 28.2\ sec.$ *(Middle) Histograms of the observed T102S-MHC:TCR dwell time distribution (aquamarine) and the productive dwell time distribution (green). The former is fit to an exponential distribution with a decay rate of* $k_{obs} = k_{off} + k_{bleach} = 12.5\ sec.$ *(Bottom) The probability of a pMHC:TCR binding event producing a localized LAT condensate as a function of dwell time. For each bin of the histograms in (A) and (B), the fraction of binding events that are productive is plotted as a point. The error bars are the standard error of the mean for a binomial variable. Fitting is the cumulative probability density function.*

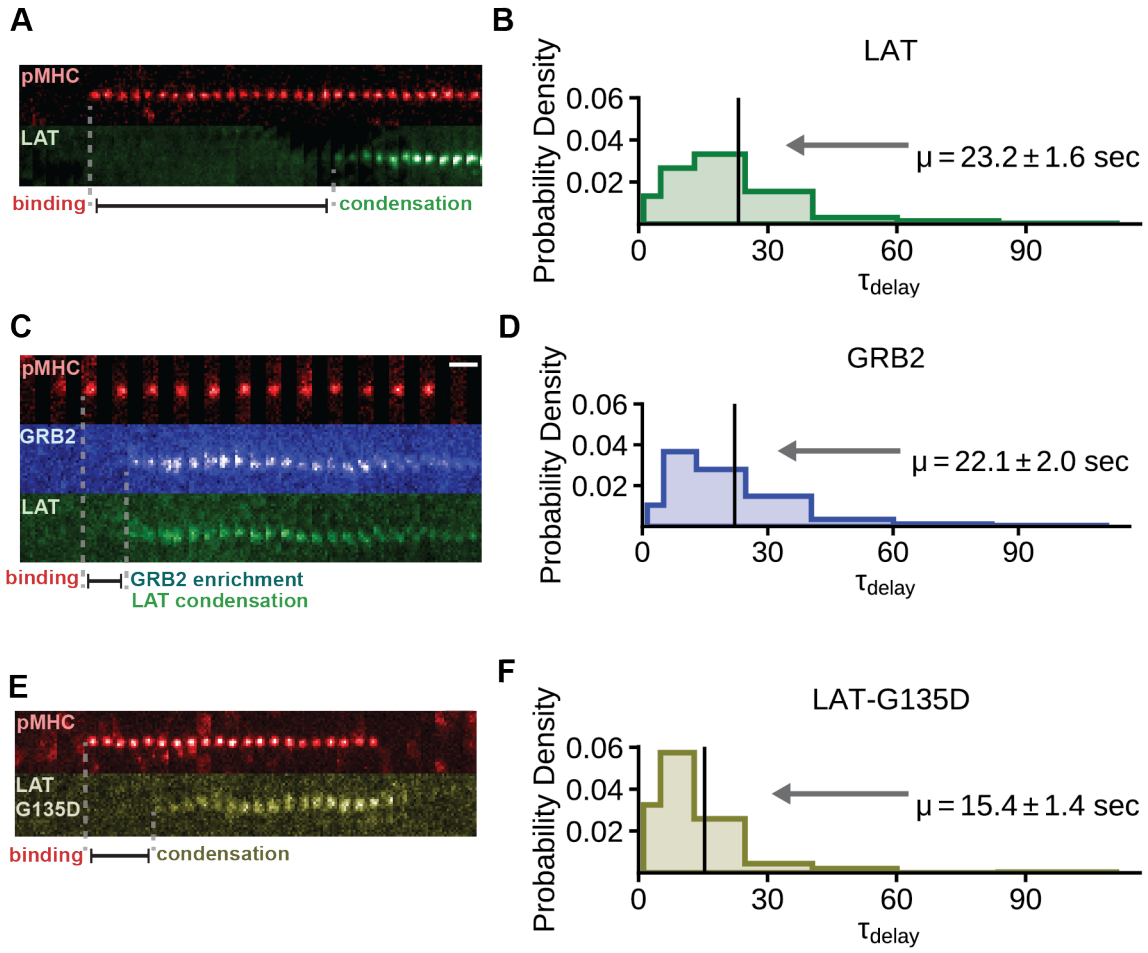

Figure 2-8: LAT condenses after an extended delay and is tuned by Y136 phosphorylation rate. *(A) TIRF images of LAT-EGFP condensation within primary murine T cells in response to a single pMHC:TCR binding event. LAT condensation occurs near the binding event after a long delay measured relative to the moment of pMHC:TCR binding. (B) Histogram of distinct LAT condensate delay times. (C) TIRF images of LAT-EGFP and mSci-Grb2 clustering within primary murine T cells in response to a single pMHC:TCR binding event. Delay times of LAT clustering and GRB2 clustering relative to pMHC binding were equivalent within the resolution of this experiment (< 2 seconds). (D) Histogram of Grb2 clustering delay times from primary murine T cells expressing mNG-Grb2 only. (E) TIRF images of LAT(G135D)-EGFP condensation within primary murine T cells in response to a single pMHC:TCR binding event. (F) Histogram of delay times after pMHC binding until LAT(G135D) condensation.*

We next addressed the question of what is causing the long delay to LAT condensation by examining the localized concentration of phosphorylated LAT prior to condensation. Grb2 primarily binds the three most C-terminal phosphorylated tyrosine residues on LAT (Y175, Y195, and Y235 in mouse) and does so independently of LAT condensation in in vitro experiments (*35*). Grb2 has been used as a precision probe for detailed kinetic studies of LAT phosphorylation (*35*, *43*), and here we used Grb2 to monitor LAT phosphorylation in T cells. In this experiment, primary AND T cells were transduced with a bicistronic P2A vector containing LAT-EGFP and mSci-Grb2. TIRF imaging experiments were performed as described before, but now simultaneously

monitoring single pMHC:TCR binding events, LAT condensation, and Grb2 recruitment in three channels. Enrichment of Grb2 was always observed simultaneously with LAT condensation with generally no detectable Grb2 enrichment prior to condensation (**Figure 2-8C**). To rule out potential artifacts from possible low cleavage efficiency of the P2A peptide, we performed further experiments with LAT(4F)-EGFP and mSci-Grb2 linked by the P2A peptide. The LAT(4F) mutant has all three primary Grb2 tyrosine binding sites (Y175, Y195, Y235) as well as the PLCγ1 site (Y136) mutated to phenylalanine. Mutant LAT(4F) failed to participate in any condensates while the simultaneously expressed Grb2 was observed to condense with endogenous LAT(WT) (**Figure 2-9**). As an additional control experiment, monocistronic mNG-Grb2 was also used to compile a histogram of Grb2 enrichment delay times, which provides an alternative measure of LAT condensation (**Figure 2-8D**). The resulting distribution, with a mean delay time of $22.1 \pm 2.0\ (\mathrm{SE})$ seconds, is nearly identical to the measured distribution using LAT imaging as the readout (**Figure 2-8B**).

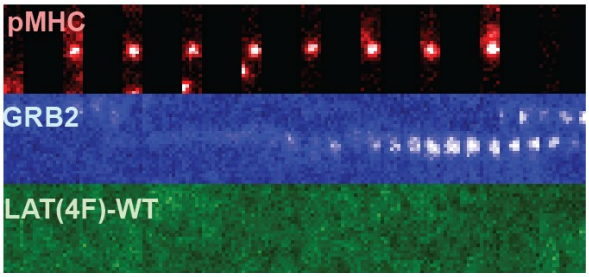

Figure 2-9: Concomitant Grb2-LAT is not due to failed P2A sleavage.
Representative trace of a cell expressing LAT(4F)-EGFP-P2A-mSci-Grb2, showing that LAT(4F) fails to participate in pMHC triggered condensation events of endogenous LAT if it does not possess its 4 distal tyrosines. mSci-Grb2, however, actively participates in condensates formed with endogenous LAT.

These results indicate that competition from phosphatases dephosphorylating LAT and diffusion of LAT away from an active pMHC:TCR complex are sufficient to maintain phosphorylated LAT densities undetectable above background. This observation rules out one possible cause of the delay between pMHC:TCR binding and LAT condensation: that it takes a sustained period of Zap70 kinase activity to build up a sufficient density of phosphorylated LAT before the phase transition can occur. It is possible that a composition fluctuation from the competing kinase-phosphatase reactions themselves contributes to the nucleating event. This conclusion is further supported by the broad distribution of measured delay times, some of which are as short as a few seconds. A deeper investigation into the mechanism of LAT condensate nucleation is described in Chapter 3.

Phosphorylation kinetics at the PLCγ1 binding site on LAT control condensation delay time

Although the delay time to LAT condensation is insensitive to both LAT and Grb2 expression levels (**Figure 2-8D** and **Figure 2-11**), we find that a LAT point mutation that modulates phosphorylation kinetics of a single, specific tyrosine residue by Zap70 substantially reduces the delay time. In human wild type LAT, the glycine immediately upstream of Y132, the PLCγ1 binding site, makes Y132 a poor substrate for Zap70 compared to Y171, Y191, and Y226 (Grb2 binding sites). By substituting the glycine for a negatively charged aspartate, the rate of Y132 phosphorylation by Zap70 dramatically increases (*25*, *50*). In our experiments, we performed the homologous mutation in murine LAT, G135D, in order to enhance the phosphorylation rate of Y136. Primary T cells expressing LAT(G135D)-EGFP over a background of endogenous wild type LAT exhibited LAT condensation events (observed by the incorporation of the labeled LAT(G135D) mutant) in response to single pMHC:TCR binding events (**Figure 2-8E**). However, the delay time between pMHC:TCR binding and LAT(G135D) condensation was dramatically reduced (**Figure 2-8F**). The resulting distribution, with a mean delay time of $15.4 \pm 1.4\ (\mathrm{SE})$ seconds, was narrower than that of LAT(WT); and the acceleration was achieved despite the presence of large amounts of endogenous wild-type LAT. This result is surprising since Y136 does not participate in canonical Grb2:SOS crosslinking of LAT. These data strongly indicate that Y136 phosphorylation plays a critical role in controlling the nucleation, and thus timing, of LAT condensates.

The relation between LAT condensates and T cell activation

LAT condensation (referred to as clustering in older publications) has long been recognized as a critical element of T cell activation by TCR (*32*, *38*, *39*). However, most prior work has examined bulk LAT condensation in response to high antigen exposure, where hundreds to thousands of times more TCR are activated than are necessary to trigger a full T cell response (*42*, *70*, *84*, *91*). Here we examine low, physiological antigen densities to measure how the sparsely distributed LAT condensates stemming from individual pMHC:TCR binding events relate to T cell activation.

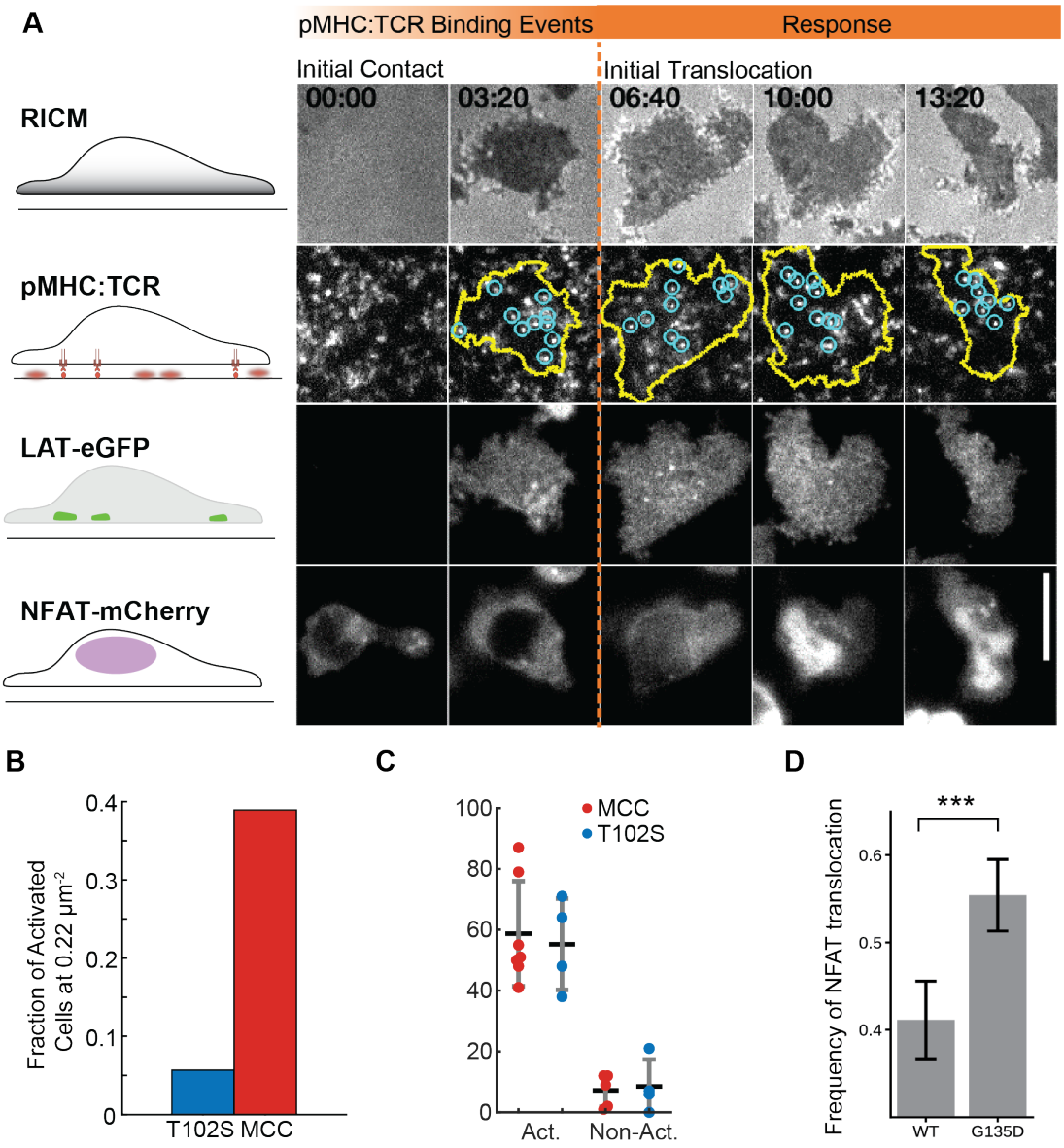

Figure 2-10: Modulating LAT condensate delay time alters antigen discrimination thresholds. *(A) Images of key molecular steps leading to NFAT translocation through time within primary T cells. T cells co-expressing LAT-EGFP and NFAT-mCh were deposited onto supported membranes containing ICAM-1 and MCC(Atto647)-MHC. First row, RICM detects cell spreading and ensures the T cell has good contact with the supported membrane. Second row, TIRF images of individual pMHC:TCR binding events (circled in blue) are recorded within the cell perimeter (yellow). Third row, TIRF images of LAT-EGFP are monitored for condensation events. Fourth row, epifluorescence images of NFAT to track moment of translocation. Bar is 10μm. (B) Bar plot showing the fraction of T cells that undergo NFAT translocation for either T102S or MCC at a fixed peptide-MHC density of 0.22 molecules/μm^2. (C) Plot showing the number of distinct LAT condensates formed prior to NFAT translocation (Act.) or the number of LAT condensates formed prior to 300 seconds if no translocation was observed (Non-Act.) (D) Bar plot showing the frequency of NFAT translocation for T cells on T102S-MHC bilayers (at 1.1 moleculesμm^2) after 30 minutes as a function of the LAT construct expressed, either WT or G135D.*

To quantify the relation between LAT condensation and T cell activation, we simultaneously monitored the formation of LAT condensates and NFAT translocation in response to pMHC:TCR binding events (**Figure 2-10A**). NFAT translocation to the nucleus occurs downstream of Ca^{2+} activation in T cells and has successfully been used as a read-out of early T cell activation (*92*–*94*). Here, we expand on an assay previously developed by our lab that mapped patterns of pMHC:TCR binding to NFAT translocation (*12*) by incorporating LAT-EGFP into the expression vector using a P2A peptide. In this manner, we can simultaneously monitor T cell adhesion, pMHC:TCR binding, LAT condensation, and the cellular activation state in real time (**Figure 2-10A**). For these experiments, T cells were incubated on bilayers with ICAM-1 and either MCC-MHC ($\tau_{bound} \approx 48$ seconds) or the shorter dwelling agonist T102S-MHC ($\tau_{bound} \approx 10$ seconds) at 0.22 molecules/μm^2 for approximately 20 min, after which we measured the final activation state (**Figure 2-10B**). Even though a smaller proportion of cells activated in response to T102S-MHC, those cells which did activate experienced a similar number of LAT condensates as T cells activated in response to MCC-MHC (**Figure 2-10C**). These data indicate that it takes 45–75 LAT condensation events within ~20 minutes to generate sufficient signal to induce NFAT translocation. The actual minimum number of LAT condensates may be lower due to the lag time of NFAT translocation.

Finally, we assessed how the delay time between pMHC:TCR binding and LAT condensation affects antigen discrimination using the LAT(G135D) mutant. The G135D mutation has been shown to enhance both Ca^{2+} and ERK activity in response to weaker agonists, particularly at low stimulation thresholds (*50*). Results comparing NFAT translocation rates between T cells overexpressing LAT(WT) or LAT(G135D) reveal that the presence of LAT(G135D) increased NFAT translocation rates by approximately fifteen percentage points (**Figure 2-10D**). These experiments were done using the weaker T102S-MHC agonist at its activation threshold density (i.e., the density of half-maximal activation), 1.1 molecules/μm^2 (*12*). While the observed effect is modest, it provides important evidence that modulating LAT condensate delay kinetics, which occur on the 20-30 second timescale, change T cell responsiveness to significantly shorter dwelling pMHC ligands.

Discussion

Ever since the application of kinetic proofreading to explain the selectivity of T cells to pMHC kinetic off-rate (*8*), many studies have sought to identify the dominant rate limiting reactions associated with TCR ligation (*19*, *50*, *95*–*97*). In this study, we show that LAT condensation events can be associated with individual pMHC:TCR ligations after a long delay time, $\langle \tau_{delay} \rangle \approx 23$ seconds. Notably, the measurements for $p_{half-max} = 24.0 \pm 1.3\ (\mathrm{SD})$ sec. (**Figure 2-7**, bottom panel) and $\langle \tau_{delay} \rangle \approx 23$ sec. are intimately related to each other (see *TCR Productivity Input-Response Function and LAT Delay*

Times in Methods). We then found that the LAT condensation delay time is connected to the ability of T cells to discriminate antigen. Introduction of the LAT(G135D) mutant, known to affect antigen discrimination (*50*), nearly halved the LAT condensate delay time, suggesting that phosphorylation of Y136 (or Y132 in humans) is a rate-limiting step to trigger LAT condensation and subsequent downstream signaling. In contrast, overexpression of Grb2 did not alter the observed condensation delay time (**Figure 2-8D**), meaning that Grb2 recruitment and crosslinking is not rate-limiting. This raises the question of what occurs after Y136 phosphorylation to enable rapid LAT condensation. It is possible that LAT may have an allosteric state that is sensitive to Y136 phosphorylation (*35*) or that PLCγ1 recruitment and crosslinking facilitates the nucleation of LAT condensates. Zeng and colleagues found that PLCγ1 can crosslink LAT in in vitro reconstituted LAT phase transition experiments on SLBs (*58*).

As the T cell lands, spreads, and crawls on the stimulatory surface, it experiences stochastic binding and unbinding events by agonist. At high agonist densities, these separate ligand binding events generate signaling trajectories that begin to overlap in space and time, producing a convoluted, composite cell response (**Figure 2-12A**). In a key study, Huse and colleagues constructed a photoactivatable MCC agonist in order to synchronize the activation of the T cell more accurately (*84*). They presented T cells to spatially fixed biotinylated MCC-MHC and subsequently started the TCR signaling reaction by UV exposure. At high ligand densities, they found an offset time of $\tau_{\mathrm{offset}} \approx 5$ seconds between photoactivation and GRB2/LAT condensation. This result is consistent with the data collected in our single pMHC experiments. Utilizing measurements of MCC-MHC on-rate, delay time (τ_{delay}), and LAT condensate duration (τ_{cluster}), we performed a basic simulation (see Methods) of the composite LAT response of thousands of T cells and extracted the mean total offset time as a function of ligand density (**Figure 2-12**), recovering a $\tau_{\mathrm{offset}} \approx 5$ seconds at high ligand densities. These results show how the scale of the system can dramatically affect the kinetics that are observed. We recapitulated how antigen density strongly affects condensation kinetics in our live cell experiments (**Figure 2-3A** and **B**).

Recently, Yi and colleagues measured kinetic delay times at a smaller scale (*70*). Depositing T cells onto static antibody coated coverslips, they measured the delay between successive clustering responses at the micron scale. They reported long delay times of ≈ 10 seconds between TCRζ clustering and Zap70 clustering and ≈ 13 seconds of delay between Zap70 clustering and GRB2 clustering (at $37°\mathrm{C}$), suggesting a composite delay time of ≈ 23 seconds between TCRζ clustering and LAT/GRB2 condensation. This result is superficially similar to the one reported here and merits further explanation. Yi and colleagues measured the time between normalized half-maximal clustering responses, meaning that the growth rate and relative cooperativity of TCRζ clusters and GRB2 clusters strongly affects the measurement. Also, there is no estimation of when ligation occurred. What remains clear, however, is that Yi and colleagues found a surprisingly long delay at the first stage of kinetic proofreading (Zap70 recruitment and activation) and at subsequent stages of signal transduction, which is consistent with our results.

For LAT to participate in a bona fide second stage of kinetic proofreading, LAT must have a physical interaction with a ligated TCR complex (*19*). Previously, we have shown that LAT condensates form within 80 nm of pMHC:TCR binding events (*19*), which is within the spatial resolution of our imaging system, suggesting close proximity of TCR and LAT at the onset of LAT condensation. Other studies have observed proximity of LAT clustering and TCRζ clustering under high density stimulation (*98*, *99*). However, those high densities obfuscate tracking LAT associated with pMHC binding. Using our single molecule ligation assay, we found that LAT condensates can experience excursion from their originating binding event. The average distance between the center of the LAT condensate and the pMHC:TCR binding event throughout their co-trajectory was 273 ± 174 (SD) nm. This distance away from the condensate likely allows Zap70 to have greater access to unphosphorylated LAT. Full incorporation of pMHC:TCR, the locus of active Zap70, within the condensate would likely quench the reaction. In addition to providing greater access to unphosphorylated LAT, the few hundred nanometers of distance tolerated by LAT condensation from ligated TCR should also allow multiple distinct binding events within $\approx 1\ \mu m^2$ to contribute to the same LAT condensate. In this manner, the LAT condensation phase transition may serve a dual role in T cell signal detection. At low agonist densities, the onset of LAT condensation serves as an extra layer of kinetic proofreading, giving the T cell greater selectivity among the noise of sparse agonist presentation. While at medium to high agonist densities, the LAT condensate may amplify T cell sensitivity by cooperatively integrating the response of separate binding events that have successfully completed the first stage of kinetic proofreading.

At low agonist densities, long dwelling binding pMHC:TCR binding events generate discrete LAT condensates spaced microns apart. Each LAT condensate represents the successful completion of kinetic proofreading by the TCR and significant signal amplification ($1\ pMHC \rightarrow \approx 250\ LAT$). Importantly, this signal is self-limiting and largely independent of pMHC:TCR after formation. Thus, at low agonist densities, LAT operates as a discrete to discrete transformation, transducing discrete pMHC:TCR binding events into discrete LAT condensates. While at higher agonist densities, the overlap of LAT condensation results in an analog output (**Figure 2-3A**). Moreover, it is the discrete number of LAT condensates formed under low agonist conditions that correlates with the cellular decision to translocate NFAT (**Figure 2-10C**). This further corroborates interpreting the LAT condensate as a fundamental unit of information used by the cell.

Many immunotherapy techniques utilize antibody fragments (*100*) or bispecific antibodies (*101*), both of which have a high affinity for the tumor antigen/TCR and produce long dwelling binding events. Here, we show that strong binders of TCR are potent producers of LAT condensates; however, lesser affinity ligands may spatially cooperate to produce LAT condensates. One form of immunotherapeutic toxicity is “off-target”, which can arise from immunotherapeutic antibody fragments having a measurable affinity for off-target antigens. In this case, the density of presentation may allow multiple lower affinity events to cooperate, triggering unwanted T cell activation (*102*). A potential solution to this may arise from the control of lateral density, both through concentration of presentation (expression level) or engineered lateral spacing as in the in vitro example utilizing DNA origami (*103*). If sufficient lateral spacing is achieved, this could preserve

specificity for on-target antigen while reducing false triggering by lower affinity off-target effects. Another form of immunotherapeutic toxicity is “on-target / off-tumor”, which arises from tumor antigens having some degree of low expression in healthy tissues (*104*, *105*). In this case, it may be useful to lower the affinity of the antibody fragment, relying on the spatial cooperativity of bound antigen to produce LAT condensation and T cell activation. In fact, there have already been some preliminary attempts to refine CAR design in this direction (*106*). The low density of off-tumor antigen expression may then be insufficient to spatially cooperate at the $1\ \mu m^2$ scale. In other cases, on-target tumor antigen is only present at low densities. However, CARs exhibit far less sensitivity to antigen compared to TCR (*107*). A recent study attempting to make CARs more sensitive to antigen found that CAR stimulation promoted weak phosphorylation of LAT. By including the Grb2 SH2 domain on the cytoplasmic CAR tail, researchers enhanced sensitivity to low density antigen. Combining these ideas, one could potentially make a CAR with similar affinity and sensitivity to TCR. In summary, the results we report here elucidate fundamental mechanisms regulating early T cell activation, which have applicability for engineering control of T cell activation.

Supplementary Figures

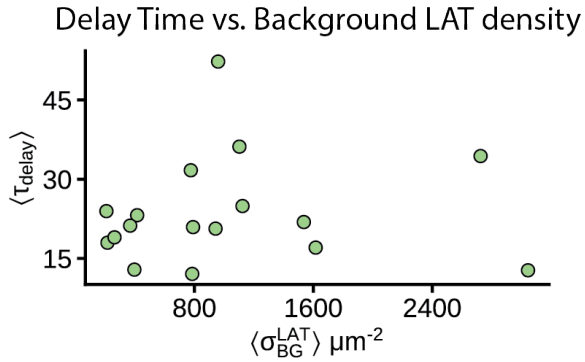

Figure 2-11: Condensate delay time is not affected by LAT expression level.
The plot shows the mean LAT condensate delay time, $< \tau_{delay} >$, for each cell (green circle) as a function of LAT expression level, $< \sigma_{BG}^{LAT} >$. Expression levels were measured using the mean background fluorescence intensity of LAT-EGFP.

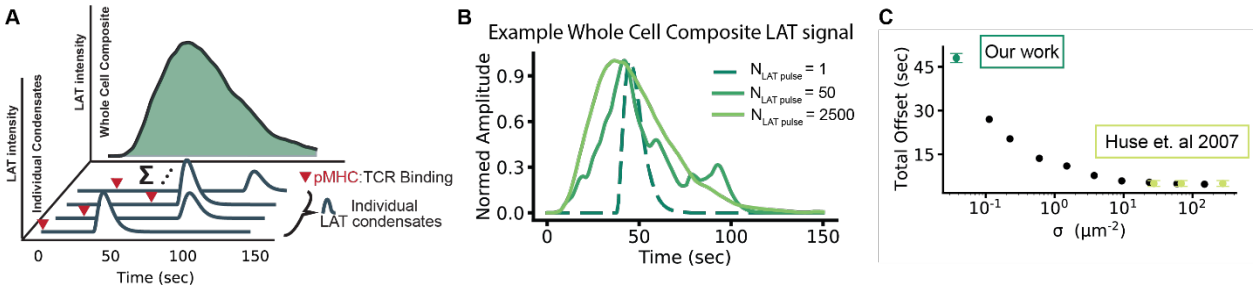

Figure 2-12: Simulation of LAT timing as a function of antigen density.
(A) Schematic showing how the output of individually signaling TCR are integrated at the cellular level. (B) Example composite cell traces for different size samples of LAT condensate pulses. The dashed line is the average expected single pulse – a wait time of ≈ 8 seconds, a delay time of ≈ 35 seconds, and a LAT condensate lifetime of ≈ 25 seconds. The solid lines are generated from random samples of n LAT condensate pulses, as described in STAR Methods. (C) Plot showing the mean total offset time for ensemble sampling of 10,000 composite LAT traces with different numbers of component LAT pulses.

3 | PLCγ1 non-enzymatically nucleates LAT condensates by specific crosslinking

Abstract

LAT condensation formed from a single pMHC:TCR binding event is a signature of productive T cell signaling. Following single TCR ligation, LAT condensation occurs after an extended delay of tens of seconds. This timing controls T cell sensitivity to antigen. We report the discovery that the PIP_2 lipase PLCγ1 nucleates LAT condensates through a structural mechanism upstream of its enzymatic activity. Modulating PLCγ1 cytosolic abundance tunes condensation delay time and formation probability. Utilizing its nSH2 and SH3 domains, PLCγ1 facilitates early crosslinking to nucleate LAT condensates while locked in the autoinhibited conformation. PLCγ1 is specifically required for this role since crosslinking leading to nucleation must occur through LAT Y136, which exclusively binds PLCγ1. This also suggests that LAT must be crosslinked in a tetravalent manner. These results reveal a sophisticated mechanism of controlling condensate delay time and antigen discrimination using a well-known enzyme in a novel capacity.

Introduction

The enzymatic function of PLCγ1 is critical to T cell signaling. PLCγ1 cleaves PIP_2 lipids to produce soluble IP_3 and DAG lipid, both of which serve as second messengers for different signaling pathways. IP_3 initiates calcium flux, while DAG activates the Ras GEF known as RasGRP (*108*, *109*). Depleting PLCγ1 in Jurkat T cells results in loss of IL-2 gene transcription (*57*). To protect against spurious activation, PLCγ1 is highly autoinhibited. An array of SH domains (SHarray) within PLCγ1 is essential for regulating its autoinhibition (*47*, *55*, *56*). Following an extended delay from single pMHC:TCR binding, the adaptor protein LAT undergoes a protein condensation phase transition upon its phosphorylation by Zap70 (see Chapter 2). PLCγ1 participates in LAT condensates where it forms a tertiary complex with LAT, SLP-76, and Gads, which is critical for PLCγ1 activation (*32*, *110*). PLCγ1 exclusively engages phosphorylated LAT at Y136 with its nSH2 domain. Y136 has an intrinsically slow phosphorylation rate by Zap70 (*25*, *49*), and accelerating Y136 phosphorylation surprisingly shortens the delay time to condensation (**Figure 2-8F**). The SH3 domain of PLCγ1 binds the adaptor protein SLP-76, though it has been observed to interact with other proteins, including SOS (*31*, *34*, *35*, *52–54*, *58*, *111*). The cSH2 domain is thought to play a purely intramolecular role, regulating autoinhibition. cSH2 maintains autoinhibition by interacting with the catalytic unit, and following PLCγ1 phosphorylation at Y783, cSH2 releases the catalytic unit and binds pY783. This causes PLCγ1 to undergo a massive structural rearrangement, resulting in a catalytically active conformation (*48*). Using its various SH domains, PLCγ1 has the potential to also operate in a structural capacity, similar to other SH-contain proteins, such as Grb2 (*58*).

Using our supported lipid bilayer platform, we investigated the role of PLCγ1 in single pMHC:TCR-induced LAT condensation. All experiments, unless otherwise noted, were performed at low densities of agonist MCC-MHC (0.2 – 0.4 molecules/μm^2). We report that PLCγ1 recruitment occurs simultaneously with LAT condensate formation. Furthermore, increasing cytosolic PLCγ1 concentration accelerates condensate delay time kinetics. Similarly, depleting endogenous PLCγ1 to near zero, by knock-down, reduces the probability of condensation. This concentration effect implies that PLCγ1 is responsible for nucleating LAT condensates in vivo. We find that nucleation occurs through the regulatory SHarray while the enzyme is locked in the autoinhibited conformation, indicating that nucleation occurs through early crosslinking of LAT. We propose that PLCγ1 crosslinks LAT to form small LAT nucleates, which quickly grow into mature condensates with further crosslinking by Grb2:SOS. Mechanistic studies using various truncations and chimeric proteins reveal that crosslinking, leading to nucleation, must specifically occur through binding LAT Y136 while the SH3 domain engages with a

yet unconfirmed binding partner, though likely SLP-76. PLCγ1 is required for nucleation since crosslinking must occur through LAT Y136. While the cSH2 domain can crosslink LAT in truncated forms of PLCγ1, in vivo nucleation does not utilize cSH2 in the full length protein due to steric occlusion. Our data also suggest that LAT must be tetravalent to form mature in vivo condensates, as experiments allowing only trivalent crosslinking fail to produce stable clusters. In total, we illustrate that PLCγ1 plays two distinct, separable roles in T cell signaling, one as a PIP_2 lipase and second in a structural capacity controlling LAT condensate nucleation and timing and, as a result, antigen discrimination.

Single pMHC:TCR induced PLCγ1 recruitment is contemporaneous with LAT condensation

Since LAT Y136 phosphorylation kinetics exhibit control over LAT condensate delay time and antigen sensitivity, we investigated what effects PLCγ1 has on condensation. In doing so, we aimed to understand how Y136 phosphorylation and PLCγ1 recruitment influence the condensate formation process. To accomplish this, we expressed full length murine $PLC\gamma1_{FL}$ fused to mNG (PLCγ1-mNG) in primary murine $CD4^+$ AND T cells, which were added to supported membranes containing ICAM-1 and low density pMHC. As in Chapter 1, single pMHC binding events were detected by the appearance of a localized bright spot of fluorescence under a T cell when imaged with TIRF microscopy using low illumination power (0.4 mW/cm^2) and long exposure (500 ms). Bona fide single pMHC:TCR complexes were spaced microns apart and mapped directly to local PLCγ1 responses inside the cell. $PLC\gamma1_{FL}$ exhibited a very uniform, low intensity background. Upon binding pMHC, some ligated TCRs productively signaled to induce a localized increase in PLCγ1-mNG fluorescence intensity corresponding to PLCγ1 recruitment from solution and clustering at the membrane (**Figure 3-1A** and **B**). These spots of PLCγ1 enrichment colocalized and comigrated with the originating pMHC:TCR as the binding event translocated in the SLB:T cell interface (**Figure 3-1B**). These condensation-like responses appeared abruptly in a low background signal after a delay from pMHC:TCR binding. This was followed by a rapid growth phase and slower decay phase, similar to LAT condensates (**Figure 3-1C**). Though the PLCγ1 clustering event shown in **Figure 3-1C** ended near the same time pMHC disengaged from the TCR, in many instances, PLCγ1 either remained clustered after or disassembled before pMHC unbinding. Overall, PLCγ1 demonstrated qualitatively similar behavior as LAT condensation in response to single pMHC:TCR binding (**Figure 2-3**).

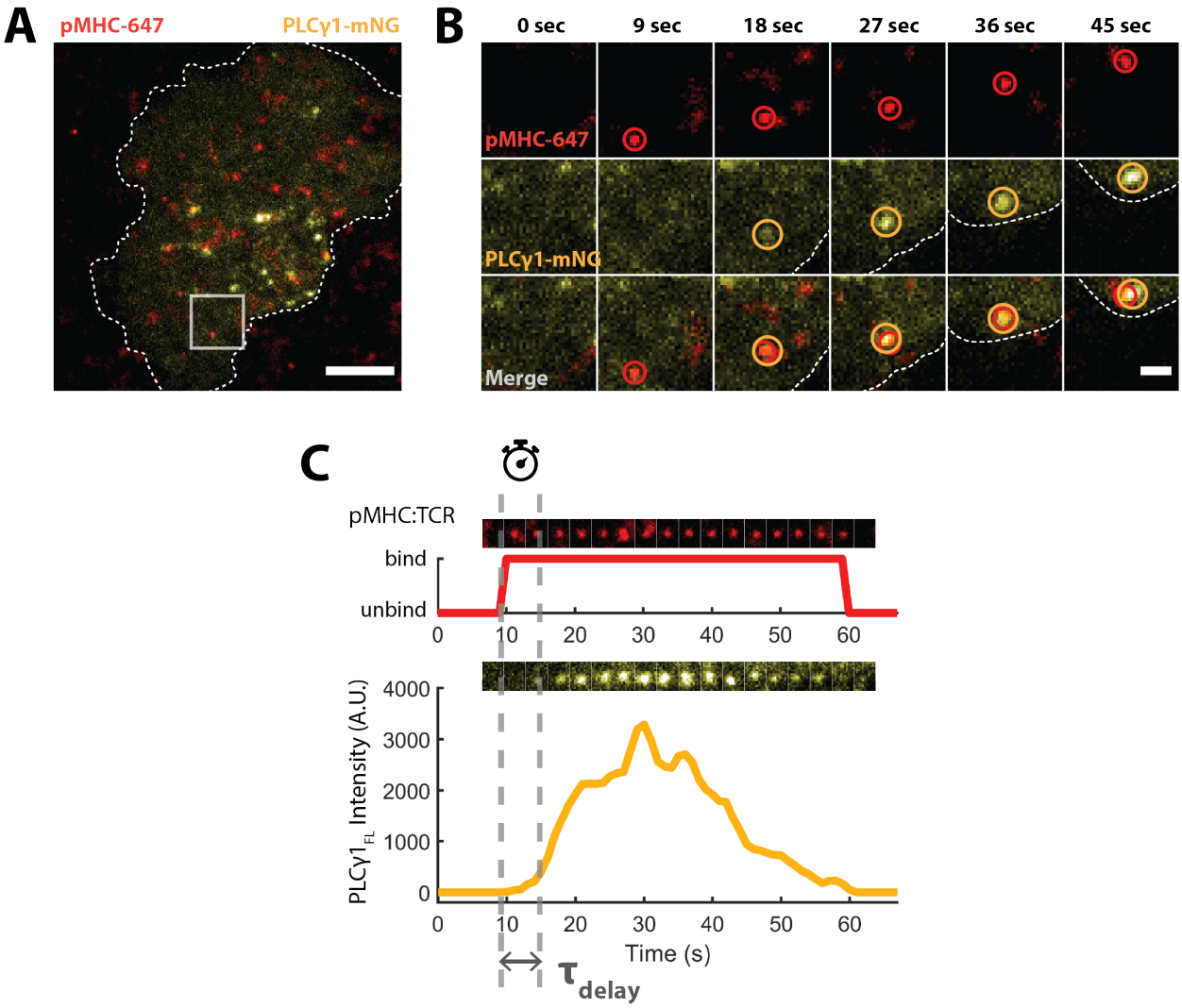

Figure 3-1: Single pMHC:TCR binding events induce discrete recruitment and clustering of PLCγ1. *(A) Primary murine T cell (outlined by white dashed line) expressing PLCγ1-mNG (yellow) interacting with a bilayer containing MCC(Att0647)-MHC (red) at single molecule density and imaged with TIFR at an exposure of 500 ms. Bar is 5μm. (B) A time series of images showing an isolated single pMHC:TCR binding event directly inducing a PLCγ1 recruitment and clustering event. The time series is a zoom-in of the white box over the cell in (A). The top row shows pMHC binding and translocation. The middle row demonstrates PLCγ1-mNG exhibiting an abrupt increase in local fluorescence in a low basal background. The bottom row is a merge of the top and middle rows. Bar is 1μm. (C). Intensity time trace of a pMHC:TCR-induced PLCγ1-mNG clustering event. The top shows the bound state of pMHC, including an image time sequence of the bound pMHC and a corresponding state function plot of the binding event. The bottom shows the PLCγ1 cluster growing and evolving over time, including an image time sequence of the PLCγ1 cluster and a corresponding intensity trace of the PLCγ1 clustering event. The time lapse between frames of pMHC and PLCγ1 images is 3 seconds.*

To determine the relative delay kinetics of PLCγ1 and LAT, we transduced primary T cells with LAT-mCh and PLCγ1-mNG and sorted for dual fluorescent cells. Placing these cells on supported membranes, all three channels (pMHC binding, LAT-mCh, and PLCγ1-mNG) were imaged within sub-second resolution of each other with a 2 second time-lapse between consecutive frames. Since the LAT Y136 phosphorylation rate is

slower compared to the Grb2-binding tyrosine residues (*25*, *49*, *50*), we anticipated PLCγ1 would recruit to LAT condensates after they begin to form. Surprisingly, the onset of PLCγ1 recruitment and LAT condensation were detected simultaneously, and both species spatially colocalizing over the lifetime of the condensate (**Figure 3-2A**). We replicated these results in Jurkat T cells by expressing LAT-EGFP and PLCγ1-HaloTag(TMR) (**Figure 3-2B**). This unexpected result demonstrates that PLCγ1 does not recruit after condensate formation, as would be expected based on tyrosine phosphorylation rates, and is consistent with high antigen stimulation experiments (*70*). From this, we conclude that at the moment LAT condensation begins, Y136 is phosphorylated. In combination with the result that condensate timing is heavily influenced by Y136 phosphorylation (**Figure 2-8F**), this suggests that condensation does not occur until Y136 is phosphorylated and binds PLCγ1. Therefore, we hypothesized that PLCγ1 actively shapes the timing and structure of LAT condensation.

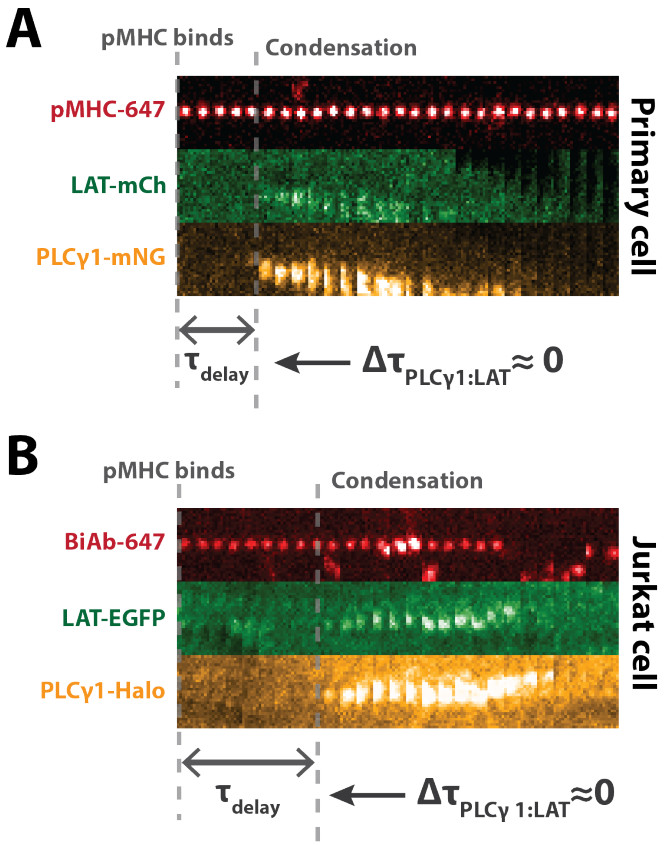

Figure 3-2: PLCγ1 recruits simultaneous with LAT condensation.
(A) PLCγ1 recruitment and LAT condensation begin simultaneously in primary murine T cells. Representative image trace of a primary murine T cell co-expressing LAT-mCh and PLCγ1-mNG placed on a supported bilayer containing MCC(Atto647)-MHC. After a delay from pMHC:TCR binding (red), PLCγ1 recruitment (yellow) and LAT condensation (green) began simultaneously. (B) PLCγ1 recruitment and LAT condensation begin simultaneously in Jurkat T cells. Representative image trace of a Jurkat T cell co-expressing LAT-EGFP and PLCγ1-HaloTag(TMR) placed on a supported bilayer containing bispecific antibody (biAb) bound to BCMA. BiAb binds TCR monovalently and is described in greater detail in Chapter

4. After a delay from BCMA:biAb:TCR binding (red), PLCγ1 recruitment (yellow) and LAT condensation (green) began simultaneously. Images were taken by TIRF. Time resolution for top and bottom is < 2 sec.

PLCγ1 in vivo abundance modulates the timing and probability of LAT condensation

To assess PLCγ1 influence on condensation, we determined whether PLCγ1 cytosolic abundance affected the delay time of LAT condensation. Since PLCγ1-mNG recruitment is detected at the same time that LAT begins to condense (**Figure 3-2**), PLCγ1 may be used as a sensor for condensation. Thus, changes in delay time kinetics as measures by PLCγ1 may be interpreted as changes in LAT condensate delay time ($\tau_{condensate}$). Therefore, we denote detection of localized PLCγ1 enrichment as LAT condensation. LAT condensate delay time under normal PLCγ1 levels is slow ($\langle\tau_{condensate}^{LAT}\rangle = 23.2\ sec.$) and broadly distributed (**Figure 3-3**, top). We increased PLCγ1 concentration by overexpressing PLCγ1$_{FL}$-mNG in primary T cells, which resulted in shortened condensate delay time ($\langle\tau_{condensate}^{PLC\gamma1}\rangle = 15.7\ sec.$) and a narrower distribution (**Figure 3-3**, bottom). Therefore, PLCγ1 exhibits similar control over condensate delay time as Y136 phosphorylation (**Figure 2-8F**), suggesting PLCγ1 plays a previously unknown role in nucleating LAT condensates.

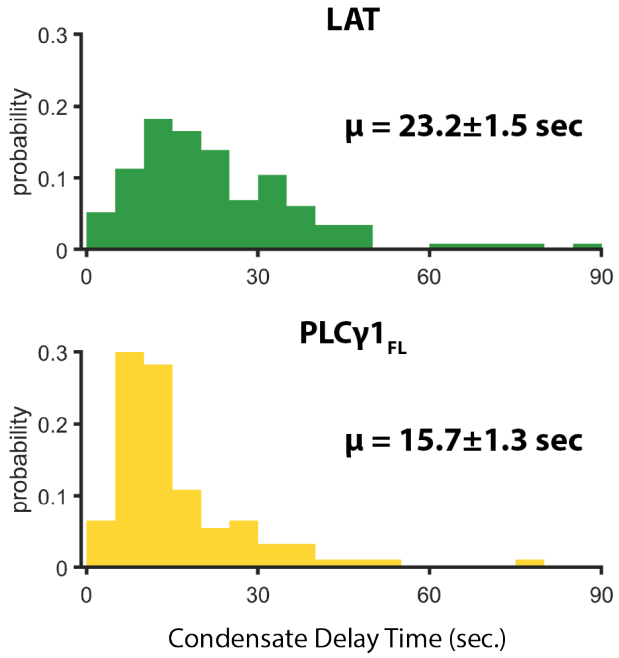

Figure 3-3: PLCγ1 overexpression accelerates condensate delay time.

LAT condensate delay time distributions with and without PLCγ1 overexpression. (Top) LAT condensate delay time distribution with normal PLCγ1 expression is slow and broadly distributed. Mean delay time is 23.2±1.5 sec (SE). (Bottom) The LAT condensate delay time distribution with PLCγ1-mNG overexpression. Mean delay time is 15.7±1.3 sec (SE). Delay times were obtained by measuring the delay between pMHC:TCR binding and the beginning of PLCγ1 recruitment. Since PLCγ1 and LAT appear at the same time, this distribution can be interpreted at the LAT condensate delay time distribution under high cytosolic PLCγ1 concentration (i.e., overexpression). The mean delay time is 15.7±1.3 sec (SE). The top and bottom distributions are statistically different, with p-value < 0.001. μ is the average delay time ± SE.

To confirm this finding, we assessed whether decreasing endogenous PLCγ1 expression had a negative effect on LAT condensation. To test this, we established a PLCγ1 knock-down Jurkat line (J.P1 cells) using stable shRNA expression. This cell line displayed >90% reduction in PLCγ1 expression (see Methods). J.P1 and wild type Jurkat cells transiently expressing LAT-EGFP were placed on supported membranes containing low agonist density. LAT condensation was attenuated in J.P1 cells relative to wild type Jurkats. Because of this, it was unfeasible to obtain sufficient data points to construct a full delay time distribution. Additionally, very long delay times are likely limited by pMHC fluorophore bleaching. Therefore, to quantify the effect on condensation, we approximated the fraction of LAT found in a condensed state. After 7 min of stimulation on supported bilayers, we fixed J.P1 and WT Jurkat cells expressing LAT-EGFP and imaged the clustering state of LAT of more than a hundred cells for each condition using TIRF. We fixed cells at 7 min to maximize the number of cells on the bilayer that were in a state of actively clustering LAT. TIRF images were processed using the image classification and segmentation software Ilastik (*112*), employing a model specifically trained to identify LAT condensate features in T cells. This model yielded probability matrices for each image, with each pixel assigned a probability value of either being background (non-condensed LAT) and clustered (condensed LAT). From this, we approximated the fraction of LAT residing in a condensed state for each cell (see Methods). The results of this analysis, as seen in **Figure 3-4**, demonstrate that the fraction of LAT found in a condensed state was significantly lower in J.P1 cells compared to wild type Jurkats. These data verify that PLCγ1 possesses control over the timing and probability of LAT condensate formation, further supporting the conclusion that PLCγ1 nucleates LAT condensation.

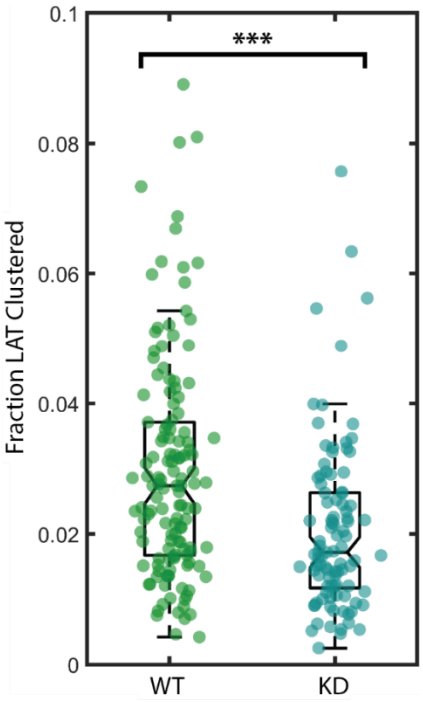

Figure 3-4: PLCγ1 knock-down decreases probability of LAT condensation.
PLCγ1-deficient Jurkat cells cluster less LAT than wild type cells. Wild type (WT) and PLCγ1-knock-down (KD) Jurkat cells expressing LAT-EGFP were placed on SLBs containing human ICAM-1 and BCMA:biAb at single molecule densities (~0.2 molecule/μm^2) and stimulated for 7 min (see Chapter 4 for details about biAb and BCMA). The fraction clustered was calculated for more than a hundred cells for each cell line (WT and KD) and plotted as a scatter (each circle represents one cell) superimposed on whisker plots of the data. The scatter on the left (green) is the distribution for WT cells. The scatter on the right (teal blue) is the distribution for KD cells which shows significantly less clustering compared to WT. The two distributions are statistically different, with p-value < 0.0001.

PLCγ1 nucleates LAT condensation by early crosslinking

We next investigated the mechanism of how PLCγ1 nucleates LAT condensation by determining which domains are critical for accelerating condensate delay time and thus nucleation. We constructed a panel of PLCγ1 mutants and truncations to identify the minimal set of domains sufficient to recapitulate accelerated nucleation (**Figure 3-5A**). First, we performed site directed mutagenesis to convert residues Y775 and Y783 to phenylalanine (Y2F) to assess whether nucleation is dependent on PLCγ1 enzymatic activity. As mentioned, the phosphorylation state of Y783 strongly controls PLCγ1 autoinhibition. When unphosphorylated, PLCγ1 remains locked in an autoinhibited conformation. Upon its phosphorylation by Itk, pY783 binds the cSH2 domain causing a

conformation rearrangement releasing autoinhibition. Mutational studies have shown that Y783F plus Y775F results in complete loss of calcium flux and NFAT activation (*47*, *56*, *113*). The exact function of Y775 phosphorylation is unknown. A recent study that resolved the first crystal structure of full length PLCγ1 removed the linker region containing Y783 to improve crystallization, and the resulting structure displayed many features consistent with autoinhibition (*48*). Therefore, these mutations render PLCγ1 catalytically inactive by locking it in an autoinhibited conformation. Overexpressing PLCγ1(Y2F)-mNG in primary T cells resulted in accelerated delay time kinetics ($\langle\tau_{condensate}^{PLC\gamma1(Y2F)}\rangle = 12.8\,sec.$) (**Figure 3-5B**, second from top) and phenotypically appeared identical to WT PLCγ1$_{FL}$, both in whole cell appearance and single pMHC:TCR-induced condensates (**Figure 3-5C**, second from top). This clearly demonstrates that PLCγ1 controls condensate nucleation via a structural mechanism that is achievable in the autoinhibited state. Thus, the domains responsible for nucleation must be reasonably accessible to bind LAT and other proteins involved in this process while PLCγ1 is in the autoinhibited conformation.

After ruling out activity-based nucleation, we speculated that PLCγ1 could facilitate condensation by two potential mechanisms. By simultaneously binding LAT Y136 with its nSH2 domain and plasma membrane lipids via its PH and C2 domains, PLCγ1 could cause LAT diffusion in the membrane to substantially decrease. Alternatively, the SHarray could facilitate early crosslinking leading to condensation, reminiscent of LAT:Grb2:SOS interactions that are responsible for driving macromolecular condensation of LAT. To test these hypotheses, we truncated off all the N- and C-terminal domains (including the catalytic and lipid binding domains) flanking the nSH2-cSH2-SH3 domains (i.e., the SHarray). Overexpressing SHarray-mNG in T cells accelerated condensate delay time ($\langle\tau_{condensate}^{SHarray}\rangle = 17.8\,sec.$) (**Figure 3-5B**, third from top) and formed large discrete condensates in a low background (**Figure 3-5C**, third from top) similar to PLCγ1$_{FL}$. This confirms that the interactions responsible for nucleation are contained within the three SH domains of PLCγ1 and are likely causing early LAT crosslinking.

We then aimed to determine whether nucleation is facilitated specifically through either the cSH2 or SH3 domains. The nSH2 domain is critical for recruiting PLCγ1 to LAT Y136. While the primary substrate of the cSH2 domain is Y783, it has been documented in other studies that, in isolation, cSH2 can promiscuously bind various tyrosine-containing proteins, including LAT (*57*, *58*, *114*). The SH3 domain is known to bind proline rich regions of SLP-76 and has been documented to also bind SOS1/2 peptides in vitro (*54*, *111*). Therefore, in theory, both cSH2 and SH3 domains could facilitate early LAT crosslinking. To assess this, we generated SHarray constructs with the cSH2 and SH3 domains independently removed (**Figure 3-5A,** SHarrayΔcSH2 and SHarrayΔSH3, respectively) and expressed them in T cells. Both the SHarrayΔcSH2-mNG and SHarrayΔSH3-mNG constructs shortened the condensate delay time ($\langle\tau_{condensate}^{SHarray\Delta cSH2}\rangle = 15.8\,sec.$ and $\langle\tau_{condensate}^{SHarray\Delta SH3}\rangle = 17.2\,sec.$, respectively) (**Figure 3-5B**, fourth and fifth from top respectively). Phenotypically, both constructs appeared qualitatively identical to PLCγ1$_{FL}$ (**Figure 3-5C**, fourth and fifth from top, respectively).

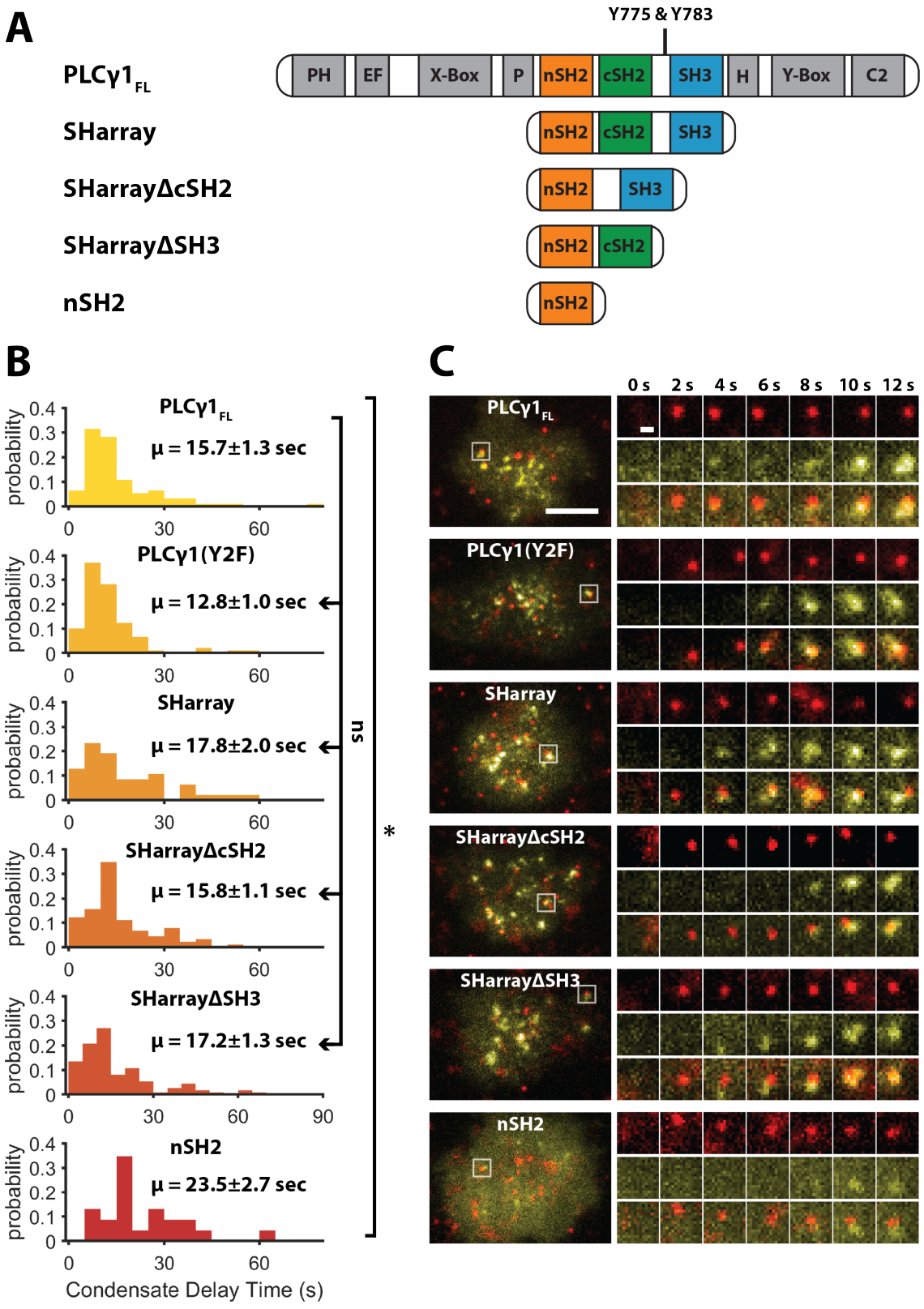

Figure 3-5: PLCγ1 nucleates LAT condensate by early crosslinking via its SH domains.
(A) Schematic of PLCγ1 constructs. PLCγ1$_{FL}$ denotes the full length, wild type protein. PLCγ1$_{FL}$(Y2F) represents PLCγ1$_{FL}$ with two Y to F mutations at Y775 and Y78 which inactive the enzyme by locking it in

the autoinhibited conformation. SHarray is the array of the SH domains (nSH2-cSH2-SH3). SHarrayΔcSH2 is the SHarray with the cSH2 domain deleted (nSH2-SH3). SHarrayΔSH3 is the SHarray with the SH3 domain deleted (nSH2-cSH2). nSH2 is the nSH2 domain only. All constructs were fused to mNG for visualization by TIRF. (B) Condensate delay time distributions of various PLCγ1 constructs. Primary murine T cells expressing the various PLCγ1-derived constructs were places on MCC-MHC stimulating SLBs and imaged with TIRF. No statistics difference exists between the delay time distributions of $PLC\gamma1_{FL}$(Y2F), SHarray, SHarrayΔcSH2, SHarrayΔSH3 and $PLC\gamma1_{FL}$(WT). The condensate delay time distributions for $PLC\gamma1_{FL}$ and nSH2 are statistically different, with p-value = 0.01. There is no statistical difference between the LAT and nSH2 delay time. For each distribution, μ is the average delay time ± SE. (C). Representative TIRF images of each construct (yellow) expressed in primary murine T cells on SLBs containing MCC(Atto674)-MHC (red). Whole cell images on the left-hand side are representative TIRF images of each respective PLCγ1-based construct. The right-hand side images are image times sequences that are a zoom-in of the box in the respective whole cell image to the left. The time series focuses on a representative single pMHC:TCR binding event (top) that produces a condensate (middle). Bar for whole cell images on the left is 5μm. The bar for the zoom-in images is 500nm.

In contrast to all other PLCγ1-derived construct variants tested thus far, overexpression of the nSH2 domain alone failed to accelerate condensate delay times. The nSH2-mNG mean delay time was tens of seconds and widely distributed, comparable with the LAT delay time distribution at normal PLCγ1 levels ($\langle\tau_{condensate}^{LAT}\rangle = 23.2\,sec.$ compared to $\langle\tau_{condensate}^{nSH2}\rangle = 23.5\,sec.$). (**Figure 3-5B**, bottom plot). Further, nSH2-mNG recruitment events were significantly smaller, and the background signal was much higher (**Figure 3-5C**, bottom). The nSH2 domain was likely sensing phosphorylated LAT in condensates without influencing its formation. This demonstrates that binding Y136 alone is insufficient to nucleate LAT condensates and further corroborates that PLCγ1 nucleates condensation by facilitating early crosslinking.

To verify that truncated PLCγ1 constructs are reliable sensors for LAT condensation, we co-expressed LAT-EGFP and nSH2-mSci using the self-cleaving P2A peptide sequence to determine if both species are detected contemporaneously. **Figure 3-6** clearly demonstrates that nSH2 recruits simultaneous with LAT condensation as observed with $PLC\gamma1_{FL}$. Therefore, the delay time measurements of all PLCγ1-based constructs accurately represent the timing of single pMHC:TCR-induced LAT condensation.

Taken together, our data indicate that the mechanism of PLCγ1-mediated nucleation of LAT condensates occurs through early LAT crosslinking. We propose that PLCγ1 facilitates LAT condensation by crosslinking the first several LAT molecules to form a small LAT “nucleate.” This nucleate structure then quickly grows and matures with the rapid addition of hundreds more LAT molecules by Grb2:SOS, and possibly more PLCγ1, crosslinking. Both the cSH2 and SH3 domains appear equally capable of inducing nucleation in the context of the truncated SHarray construct. Interestingly, SHarrayΔcSH2 and SHarrayΔSH3 accomplish this by fundamentally different mechanisms due to their distinct molecular interactions (cSH2:pTyr verse SH3:PR). The results from these experiments raise two important questions. First, are cSH2 and SH3 still capable of facilitating condensate nucleation in the context of full length PLCγ1? Second, is LAT Y136 necessary for nucleating condensates, or can this be achieved by binding and crosslinking any LAT tyrosine residues?

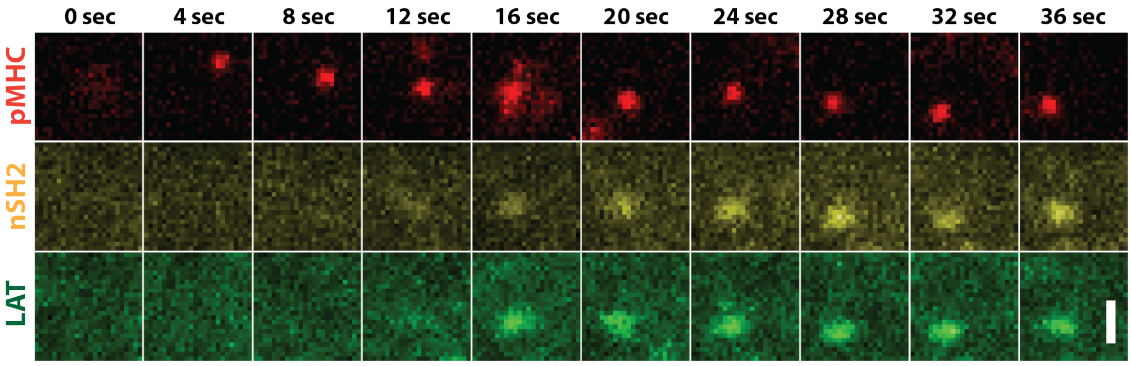

Figure 3-6: nSH2 domain recruitment is simultaneous with LAT condensation.
Primary murine T cells co-expressing nSH2-mSi (yellow) and LAT-EGFP (green) were placed on stimulating bilayers containing MCC(Atto647)-MHC (red). The TIRF image time series shows nSH2 and LAT were detected simultaneously, indicating all PLCγ1 mutation and truncation constructs are accurate sensors of LAT condensation delay kinetics. Bar is 1μm.

Condensate nucleation requires the PLCγ1 SH3 domain

In the context of the SHarray construct, cSH2 and SH3 were equally capable of nucleating LAT condensates in conjunction with the nSH2 domain. This is in agreement with previous studies imaging primary T cells and Jurkats stimulated on anti-TCR antibody coated coverslips (i.e., saturating TCR stimulation) (*58*, *115*). Those experiments suggest that PLCγ1 recruits and clusters at the membrane so long as the nSH2 plus either cSH2 or SH3 domains are present and functional. Based on the crystal structure of PLCγ1 published by Hajicek and colleagues, the nSH2 and SH3 domains are nearly fully solvent exposed and easily accessible for binding substrate in the autoinhibited state (**Figure 3-7**) (*48*). However, the cSH2 domain appears sterically occluded, with much of its surface sandwiched between various domains. Liu and colleagues point out that the phospho-peptide binding pocket of cSH2 is not accessible as it interacts with the catalytic unit to maintain autoinhibition (*116*). We suspect that the conflicting results between structural data (*48*, *116*) and live cell experiments (*58*, *115*) are a result of high antigen stimulation of T cells. We hypothesized that the cSH2 domain is incapable of binding intermolecular phosphotyrosine in the context of full length, autoinhibited PLCγ1, and, therefore, is not involved in nucleating LAT condensation.

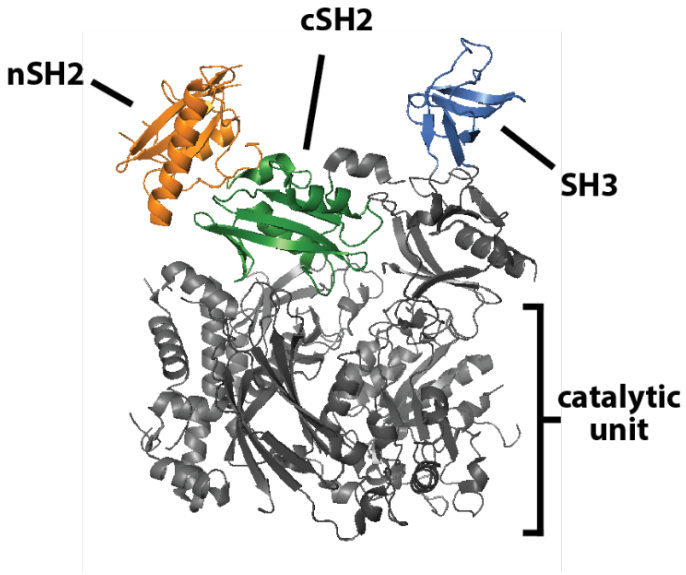

Figure 3-7: Crystal structure of autoinhibited PLCγ1$_{FL}$ suggests cSH2 is sterically occluded.
The crystal structure of autoinhibited PLCγ1$_{FL}$ published by Hajicek and colleagues (48). nSH2 (orange) and SH3 (blue) domains are highly solvent exposed, while the cSH2 domain (green) is sandwiched between the nSH2, split PH, and various domains of the catalytic unit (gray).

To test this, we deleted the SH3 domain from full length PLCγ1 (PLCγ1ΔSH3) and replaced it with a flexible linker to avoid misfolding (**Figure 3-8A**). The linker length was slightly longer than the approximate distance between the two "cleaved ends" (~18 Å vs ~13 Å, respectively). When expressed in primary T cells, PLCγ1ΔSH3-mNG yielded dramatically different results compared to PLCγ1$_{FL}$ when stimulated at low pMHC density (~0.2 molecules/μm^2). As shown previously, in response to productive single pMHC:TCR binding, PLCγ1$_{FL}$ gives rise to icon condensate features, including an abrupt and stable increase in local fluorescence intensity in the surrounding low background (**Figure 3-8B**, top). Conversely, PLCγ1ΔSH3 clustering events at single pMHC:TCR complexes were diffuse and unstable with a high background signal (**Figure 3-8B**, bottom). In many instances, it was difficult to determine whether PLCγ1ΔSH3 clustering features were caused by pMHC:TCR binding or whether they were stochastic density fluctuations. This convincingly demonstrates that the cSH2 domain does not participate in intermolecular crosslinking in the full length protein and, therefore, is not involved in LAT condensate nucleation. While SHarrayΔSH3 does nucleate condensates, it does so because cSH2 is free and unobstructed to bind a variety of phosphotyrosine substrates, such as LAT. We did not delete the cSH2 domain from PLCγ1$_{FL}$ since a recent study showed that doing so results in cell death, likely due to loss of autoinhibition or misfolding (*58*). The SH3 domain, on the other hand, does not make any intramolecular contacts in the autoinhibited structure, being mostly solvent exposed (**Figure 3-7**).

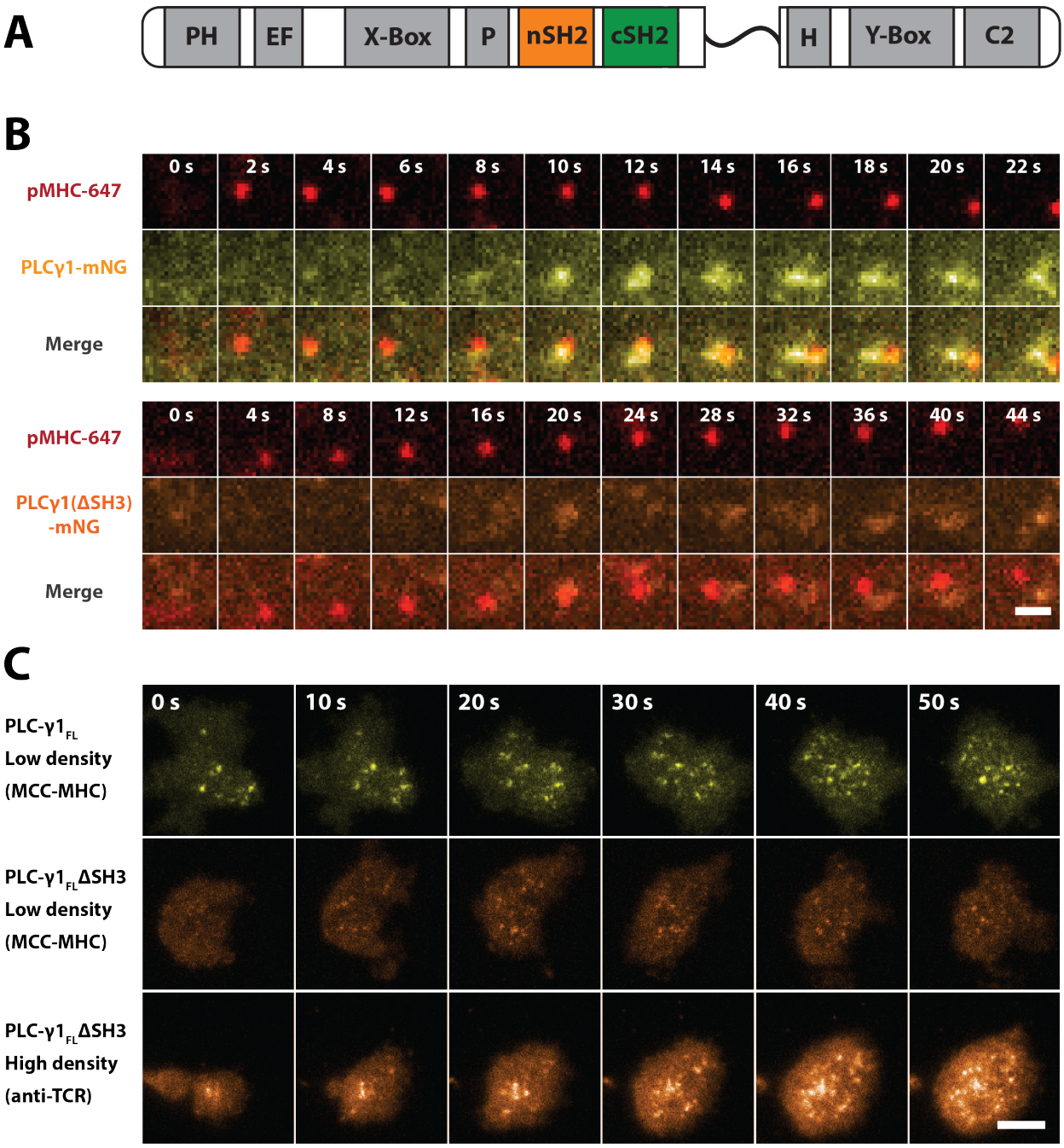

Figure 3-8: Deletion of SH3 domain inhibits condensation under single molecule stimulation.
(A) Schematic of PLCγ1$_{FL}$ΔSH3. The SH3 domain is deleted from full length PLCγ1 and replaced by a flexible linker that was slightly longer than the approximate distance between the two "cleaved ends" (~18 Å vs ~13 Å, respectively). (B) Representative image time series of single pMHC:TCR inducing condensation with either PLCγ1$_{FL}$(WT) or PLCγ1$_{FL}$ΔSH3 overexpression. Primary murine T cells expressing either PLCγ1$_{FL}$(WT)-mNG (yellow, top montage series) or PLCγ1$_{FL}$ΔSH3)-mNG (orange, bottom montage series) were placed on stimulatory bilayers containing MCC(Atto647)-MHC (red in both montages). PLCγ1$_{FL}$(WT) produced strong condensation events, while PLCγ1$_{FL}$ΔSH3 clustering events were diffuse and unstable. Bar is 1μm. (C). Representative whole cell TIRF images of primary murine T cells expressing either PLCγ1$_{FL}$ or PLCγ1$_{FL}$ΔSH3 under different degrees of TCR stimulation. (Top) T cell expressing PLCγ1$_{FL}$(WT) (yellow) on a supported membrane with low density MCC-MHC (not shown). (Middle) T cell expressing

PLCγ1$_{FL}$ΔSH3 (orange) on a supported membrane with low density MCC-MHC. In contrast to PLCγ1$_{FL}$(WT), PLCγ1$_{FL}$ΔSH3 fails to produce stable condensates. (Bottom) T cell expressing PLCγ1$_{FL}$ΔSH3 (orange) landing on a glass coverslip coated with anti-TCRβ antibody (H57-597). Such saturating stimulation "rescues" condensation. Bar is 5μm.

This result was obtained in primary T cells stimulated with physiological antigen densities and stands in contrast with antibody stimulation studies that suggest the SH3 domain is dispensable if the cSH2 domain is functional (*58*, *115*). To demonstrate that our observations are not due to experimental or protein folding artifacts, we placed primary T cells expressing PLCγ1ΔSH3-mNG on anti-TCRβ (H57-597) coated coverslips and image clustering behavior. Under such saturating stimulation, PLCγ1ΔSH3 strongly recruited and clustered at the membrane, appearing qualitatively similar to PLCγ1$_{FL}$ on low pMHC density supported bilayers (**Figure 3-8C**), recapitulating observations from antibody stimulation studies (*58*, *115*). Therefore, high density TCR stimulation artificially causes PLCγ1ΔSH3 clustering at the membrane, bypassing normal signaling mechanisms. This highlights that the magnitude of stimulation is an important factor in TCR signaling that cannot be ignored, especially in protein clustering studies. In total, these data conclusively demonstrate that the SH3 domain is, in fact, crucial for stable recruitment of PLCγ1 to LAT and that the mechanism of PLCγ1-mediation nucleation of LAT condensates occurs through the SH3, and not cSH2, domain.

Crosslinking through Y136 is essential for condensation

Finally, we aimed to determine whether LAT Y136 is uniquely required to facilitate nucleation of LAT condensates or if early crosslinking can be achieved through binding any LAT tyrosine residue. To test this, we assembled two chimeric tandem SH2 (tdSH2) constructs with specificity for different LAT tyrosines. As mentioned, the SH2 domain of Grb2 binds all three C-terminal tyrosine residues (Y175, Y195, and Y235) but does not bind Y136 (*31*, *34*, *35*). Only PLCγ1 can bind Y136 through its nSH2 domain. Therefore, by fusing the nSH2 domain of PLCγ1 with the SH2 domain of Grb2 (tdSH2(PG)), we made a construct capable of engaging Y136 plus any of the remaining tyrosines (**Figure 3-9A**). Additionally, we combined two Grb2 SH2 domains together to make tdSH2(GG) which is only able to crosslink LAT through Y175, Y195, and Y235 (**Figure 3-9B**). The SH2 domains of both constructs were fused with the same flexible linker. Any differences in their ability to induce condensation can be directly correlated with the requirement of Y136 to nucleate LAT.

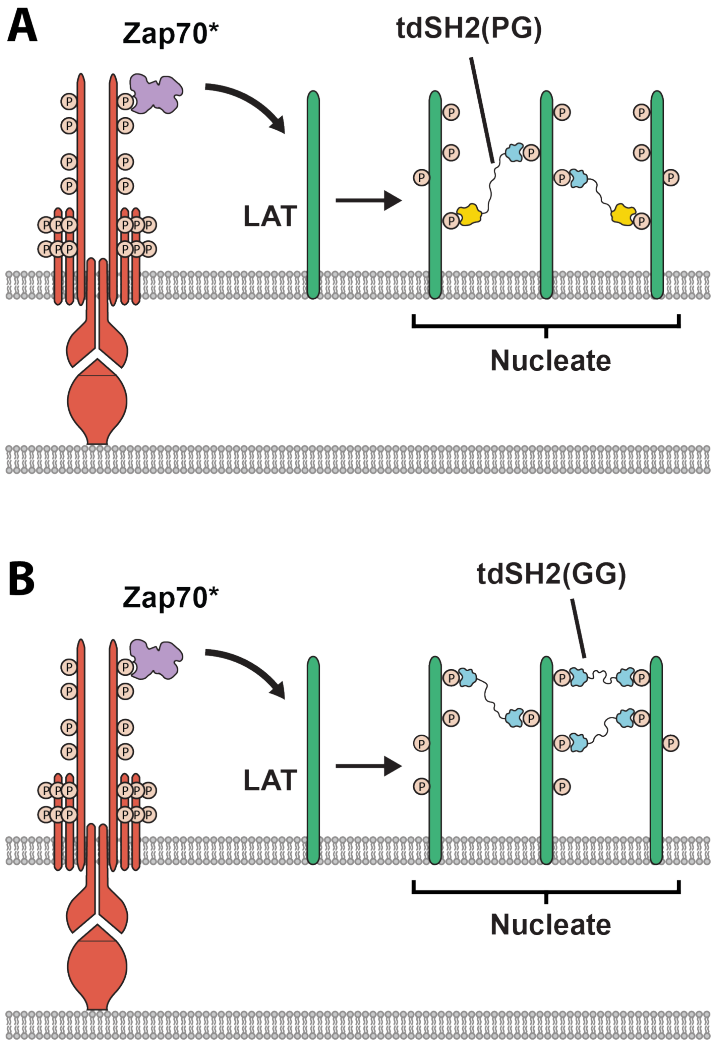

Figure 3-9: tdSH2(PG) vs tdSH2(GG) construct LAT binding diagram.
(A) Schematic of tdSH2(PG) crosslinking LAT. tdSH2(PG) is a chimeric protein composed of the nSH2 domain of PLCγ1 fused to the SH2 domain of Grb2. This construct can bind and crosslink through all four C-terminal pTyr residues on LAT, including Y136. (B) Schematic of tdSH2(GG) crosslinking LAT. tdSH2(GG) is composed of two SH2 domains of Grb2 fused together in tandem using the same linker employed in tdSH2(PG). This construct can only bind and crosslink through the three most C-terminal pTyr residues on LAT, not Y136. Both constructs were tagged with mNG.

Expressing mNG-tagged tdSH2(PG) and tdSH2(GG) in primary T cells resulted in strikingly different outcomes. **Figure 3-10** shows time series images of two representative cells expressing either tdSH2(PG) (**Figure 3-10A**) or tdSH2(GG) (**Figure 3-10B**). As can be seen, tdSH2(PG) qualitatively resembles $PLC\gamma1_{FL}$, giving rise to prototypical, stable discrete condensates. On the other hand, tdSH2(GG) rarely produced condensate-like structures, and those that did form were short-lived. Examining single pMHC:TCR-induced condensation events, the two chimeric proteins showed several marked differences (**Figure 3-11A** and **B**). These differences are highlighted in the intensity traces in **Figure 3-11C** and **D**. The numbered intensity traces in **C** and **D** correspond to the time sequence images in **A** and **B**, respectively. Juxtaposing the data from both chimeric proteins, tdSH2(PG) clearly produced significantly larger and long-lived

condensates compared to tdSH2(GG) (**Figure 3-11 A** and **C** verse **B** and **D**). As shown in **Figure 3-11A** and **C**, tdSH2(PG)-nucleated condensates exhibited iconic LAT condensate features, including abrupt appearance followed by rapid, stable growth and ending in exponential-like decay. Conversely, tdSH2(GG)-induced clusters displayed slow and unstable growth, with clusters frequently fluctuating down to background levels (**Figure 3-11 B** and **D**, traces 1, 4, 5, and 6). Interestingly, this appears to suggest that tSH2(GG) is inhibitive to condensation. Additionally, tdSH2(PG) displayed faster delay time kinetics relative to tdSH2(GG) (**Figure 3-11 E** verse **F**).

Taken together, our data clearly indicate that productive crosslinking, necessary to nucleate LAT condensation, must occur specifically through binding Y136. This demonstrates why PLCγ1 is required for nucleation because it exclusively binds Y136. This novel insight augments the classical view of LAT condensation that clustering primarily occurs through Grb2:SOS-mediated crosslinking. These data also suggest that LAT must be tetravalent to achieve nucleation and stable condensation.

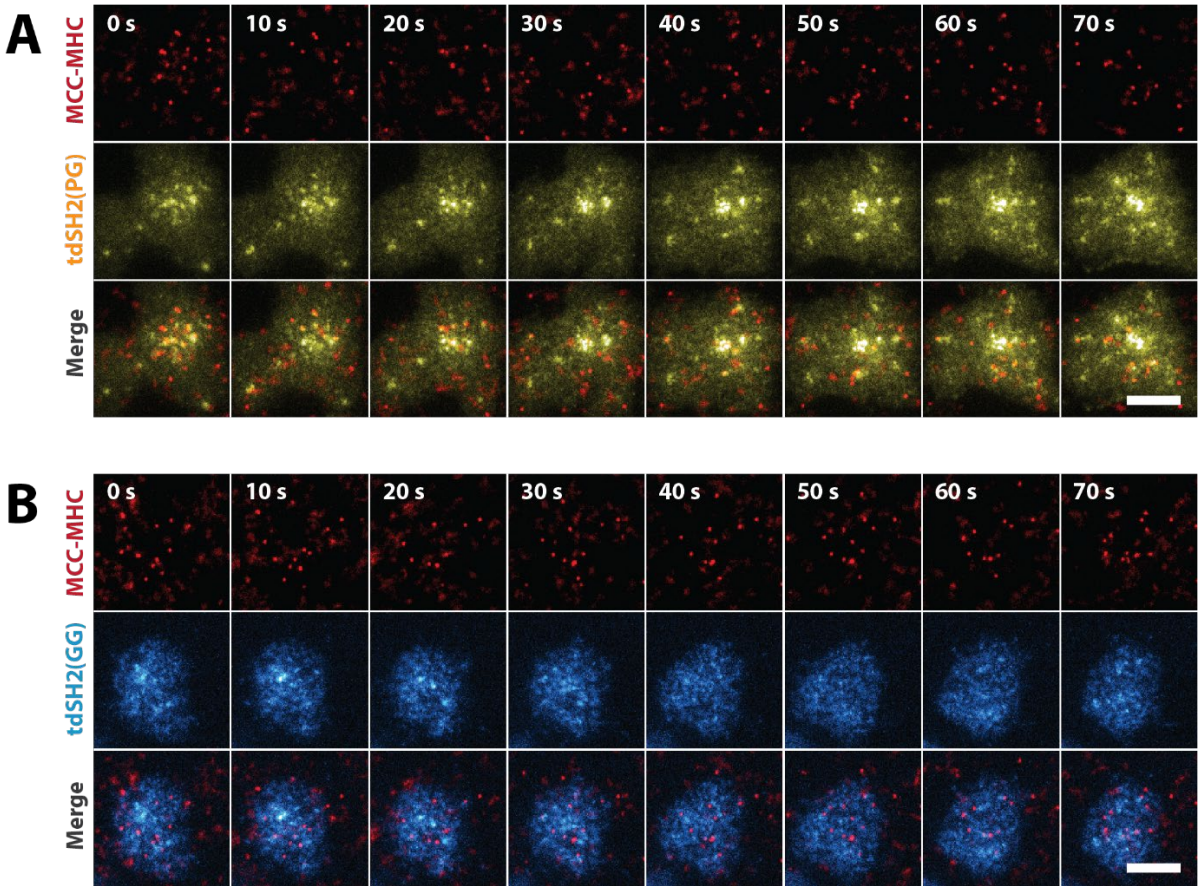

Figure 3-10: tdSH2(PG) appears similar to PLCγ1$_{FL}$ while tdSH2(GG) fails to robustly cluster.
(A) Representative image time series of a primary murine T cell expressing tdSH2(PG)-mNG (yellow) on a supported membrane containing MCC(Atto647)-MHC (red). tdSH2(PG) resulted in robust condensation similar to PLCγ1. Bar is 5μm. (B). Representative image time series of a primary murine T cell expressing tdSH2(GG)-mNG (light blue) on a supported membrane containing MCC(Atto647)-MHC (red). tdSH2(PG) clusters were rare and small compared to tdSH2(GG). Bar is 5μm.

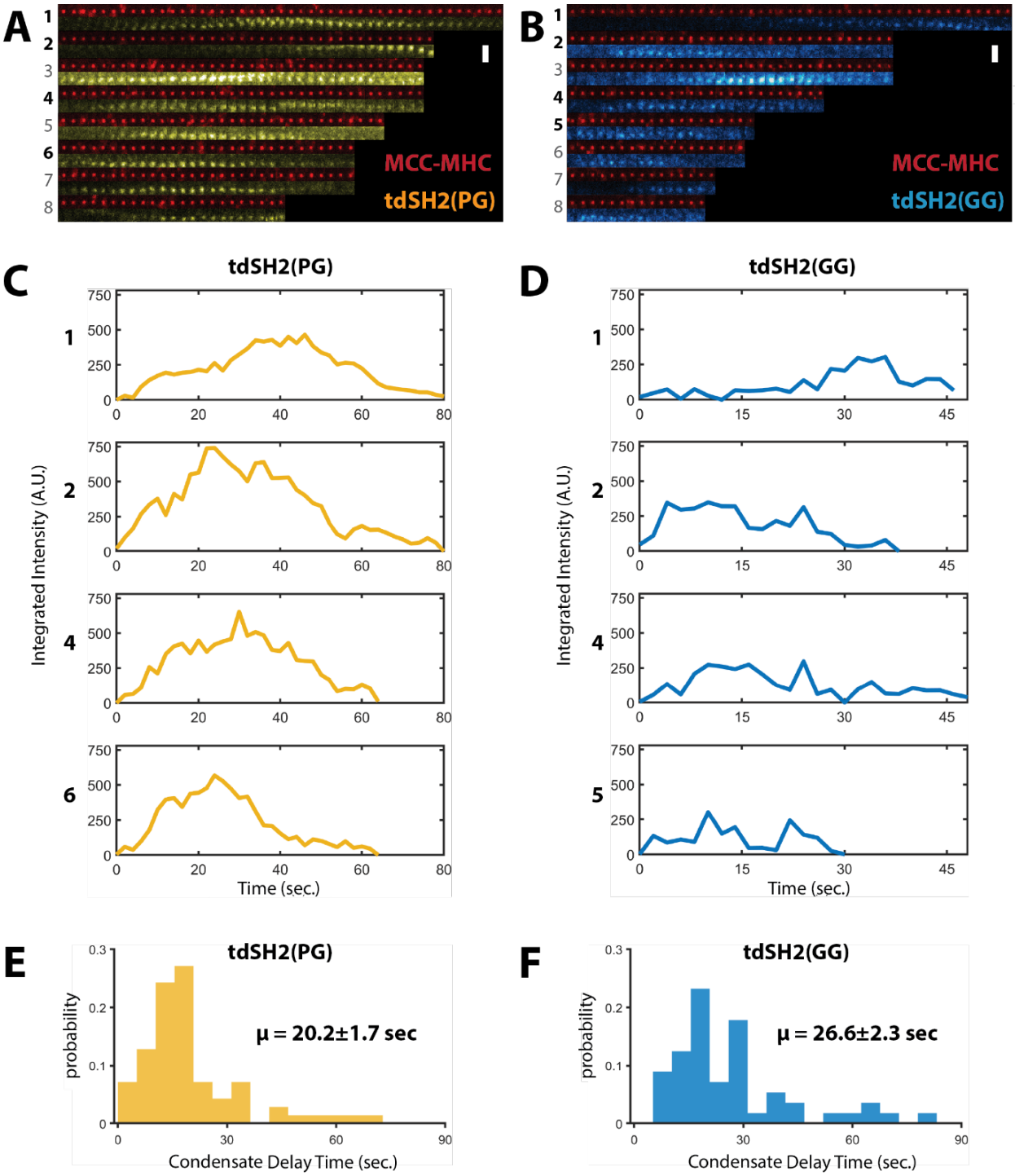

Figure 3-11: tdSH2(PG) facilitates robust LAT condensation but not tdSH2(GG).
(A) A series of time sequence images of single pMHC:TCR complexes inducing tdSH2(PG)-crosslinked condensates. Each numbered row consists of a single MCC(Atto647)-MHC binding event (red, top of each numbered row) tracked over time and the resulting condensate formed and detected by tdSH2(PG)-mNG (yellow, bottom of each numbered row). The eight representative TIRF image time traces are displayed from multiple cells. The first frame in each trace is the beginning of the pMHC:TCR binding event, and the time lapse between frames is 2 sec. The montages exemplify that tdSH2(PG)-nucleated condensates appear similar to PLCγ1-nucleated LAT condensates. The vertical bar is 2μm. (B) A series of time sequence

*images of single pMHC:TCR complexes inducing tdSH2(GG)-crosslinked condensates. Each numbered row consists of a single MCC(Atto647)-MHC binding event (red, top of each numbered row) tracked over time and the resulting condensate formed and detected by tdSH2(GG)-mNG (light blue, bottom of each numbered row). The eight representative TIRF image time traces are displayed from multiple cells. The first frame in each trace is the beginning of the pMHC:TCR binding event, and the time lapse between frames is 2 sec. The montages exemplify many features of tdSH2(GG)-nucleated condensates, which appear small and unstable. Cells rarely produced large condensates. The vertical bar is 2μm. (C) Selected condensate intensity traces from A (see numbering). Dynamic features appear very similar to PLCγ1$_{FL}$ (see **Figure 2-1C**). (D) Selected condensate intensity traces from B (see numbering) (note the x-axis scale differences between C and D). tdSH2(GG) condensates were smaller and had shorter lifetimes compared to C, and were unstable. (E) Condensate delay time distribution of tdSH2(PG). (F) Condensate delay time distribution of tdSH2(GG). The delay time of tdSH2(GG)-induced condensates is statistically longer than the delay of tdSH2(PG) (p-value = 0.031). For delay time distributions, μ is average delay time ± SE.*

Discussion

The majority of PLCγ1 studies to date have primarily focused on understanding its enzymatic role in signal transduction pathways, including deciphering its regulatory mechanism of transitioning from an autoinhibited to active state. Only one recent study has suggested that PLCγ1 is capable of playing a purely structural role in T cells, separate from its enzymatic function (*58*). Those researchers demonstrated that PLCγ1 is capable of using its SH domains to crosslink LAT in vitro. The work we presented here is the first to describe that PLCγ1 plays a critical signaling role upstream of its enzymatic function in regulating and nucleating discrete LAT condensates formed from single pMHC:TCR binding events in living cells.

Work from Zeng et al. has shown that including PLCγ1 in reconstituted in vitro LAT:Grb2:SOS phase transitions on SLBs accelerates the rate of global phase separation (*58*). It is important to differentiate the work reported by Zeng and the results we present here. These researchers nicely demonstrated that PLCγ1 can play a structural role in LAT condensation, as we have observed. However, due to limitations of in vitro reconstitution, LAT condensates are formed by adding necessary assembly constituents into the bulk solution. Therefore, this system does not rely on activating single TCR nor on a kinetic proofreading mechanism. Additionally, with no point of reference to measure delay kinetics, it is impossible in such experiments to determine what causes condensates to form. Only the characteristics of already maturing condensates are measured. As a result, this study can only conclude that PLCγ1 can structurally incorporate into LAT assemblies and change the physical and kinetic characteristics of maturing condensates but not nucleation. Single molecule pMHC:TCR experiments in living cells allow direct and precise measurement of condensate delay time and its signaling consequences. The delay time contains all kinetic steps that must be passed to condense LAT. The ability to perturb delay time by tuning PLCγ1 cellular abundance indicates that PLCγ1 is doing more than participating in mature condensate structure. Therefore, we can confidently

conclude from our data that PLCγ1 not only influences condensate structure but controls its timing and nucleating.

Interestingly, increasing the concentration of either PLCγ1 or LAT phospho-Y136, via LAT(G135D), yields similar outcomes, suggesting that both must be rate limiting. The intrinsic slow phosphorylation rate of Y136 by Zap70 explains its limiting nature, and a recent study measuring in vivo protein copy number in effector T cells has shown that PLCγ1 is present in low abundance (~10,000 copies on average per cell, ~30nM cellular concentration, see Methods for molarity calculation) (*117*). Since both species are limiting in the cell, increasing the concentration of either one greatly accelerates the condensation process. This is consistent with the idea that PLCγ1-mediated condensate nucleation by crosslinking through phospho-Y136 is a major kinetic bottleneck step. Conversely, Grb2 is estimated to be present at substantially higher concentrations in the cell (~200,000 copies on average per cell, ~650nM cellular concentration, see Methods for molarity calculation) (*117*), and increasing its cellular concentration by overexpression has no effect on condensate delay time (see **Figure 2-8D** in Chapter 2), implicating that LAT tyrosine phosphorylation at Grb2 binding sites is not rate limiting. Therefore, in vivo LAT phase transition nucleation by PLCγ1 constitutes a significant, and previously unknown, kinetic proofreading bottleneck step, controlling kinetic antigen signaling thresholds.

Our data also highlight the importance of studying T cells under physiological, single molecule pMHC stimulation. The true physiological context of TCR signaling is a T cell physically juxtaposed with an antigen presenting cell. The abundance of agonist pMHC on an APC surface is only on the order of tens of molecules. A growing body of work illustrates that TCRs operate at the single receptor, single pMHC level (*10*–*14*, *69*, *118*, *119*). However, the vast majority of experiment work studying T cell signaling is performed under unphysiological, high antigen stimulation (*38*, *41*, *58*, *70*, *115*). Such studies artificially activate T cells by crosslinking receptors with high affinity antibodies or tetrameric pMHC either in solution or immobilized on glass surfaces. High antigen stimulation can potentially bypass important regulatory steps or induce artifactual clustering of signaling proteins. For example, TCR-crosslinking antibodies may cause membrane protein clustering by external crosslinking or by locally hyper-concentrating Zap70. While the knowledge gained from such studies is highly informative, it should be interpreted judiciously. For instance, high antigen stimulation experiments have suggested that mutating or deleting the SH3 domain of PLCγ1 has little consequence for recruitment and clustering, causing it to appear that the cSH2 domain engages in crosslinking (*58*, *115*). However, under single molecule pMHC stimulation, deleting the SH3 domain abrogates the ability of PLCγ1 to strongly bind LAT and nucleate condensates. By placing T cells on activating antibody-coated coverslips, we can rescue recruitment and clustering by mimicking previous experiments. Therefore, accurately measuring TCR signaling processes necessitates studying T cells under physiological single molecule pMHC conditions.

In vitro reconstitution studies are extremely powerful in dissecting cellular signaling mechanisms, though they should always be interpreted based on how the results fit into the context of the cell and all its components. One group of researchers found that by

adding PLCγ1$_{FL}$ to SLB-bound phospho-LAT, they could induce a two-component phase transition without Grb2 and SOS, presumably by directly crosslinking LAT through binding of the nSH2 and cSH2 domains (*58*). It is important to note that these researchers only observed this two-component phase transition when PLCγ1 concentration was an order of magnitude above measured cytosolic concentrations. Our in vivo data clearly indicates that the SH3 domain is required for condensate formation. It is likely that in vitro reconstitution mimics high antigen stimulation experiments, thus circumventing the requirement for the SH3 domain. Furthermore, the concept of the cSH2 domain engaging in LAT crosslinking presents a significant signaling challenge. As mentioned, cSH2 is crucial for maintaining autoinhibition by interacting with the catalytic unit. If cSH2 disengages the catalytic unit to bind LAT, it would likely cause unregulated lipase activation. Condensate nucleation does not require Y783 phosphorylation (**Figure 3-5B**), but PLCγ1 activation does (*47*, *55*, *56*, *113*). Therefore, we are skeptical that any crosslinking through cSH2 occurs in vivo under physiological conditions. If it does, it must occur after Y783 phosphorylation. Perhaps this would provide signaling amplification within mature LAT condensates (*51*).

Our data points to a crosslinking mechanism of nucleation through which PLCγ1 binds LAT Y136 and a yet unconfirmed binding partner with its SH3 domain. Below we explore several possibilities of how the SH3 domain may facilitate early crosslinking. The SH3 domain of PLCγ1 is known to engage SLP-76, which binds the adaptor protein Gads (*52*–*54*). It is generally believed that tertiary binding of LAT:PLCγ1:SLP-76:Gads:LAT occurs on the same LAT molecule (cis binding), forming a circular arrangement (*32*, *120*). This cis configuration is required for PLCγ1 activation and downstream signaling, such as ERK phosphorylation (*32*). Even though cis binding is necessary for PLCγ1 signaling, it does not eliminate the possibility of trans binding to crosslink two LAT molecules (**Figure 3-12A**). One problem with this model is that it only results in the effective dimerization of LAT. We suspect higher order LAT oligomerization is required to form a nucleate.

SLP-76 itself is capable of homo-oligomerization through its SAM domain. Crystal structures suggest that SAM domains can achieve higher order polymerization (*121*, *122*), and the SAM domain of SLP-76 has been implied in microcluster formation in TCR signaling (*123*). This study detected up to tetramers of SLP-76 SAM domain in isolation, using dynamic light scattering and fluorescent microscale thermophoresis. Deletion of the SAM domain resulted in loss of NFAT translocation and IL-2 production. Therefore, the SAM domain could reasonably provide the crosslinking required for condensate nucleation (**Figure 3-12B**), though it is not known whether such extended oligomerization is conformationally possible in the context of a two-dimensional phase transition on the membrane. Alternatively, the adaptor protein ADAP could oligomerize LAT by multivalent binding SLP-76 via SH2:pTyr interactions (**Figure 3-12C**) (*124*). Experimental attempts to reconstitute LAT phase transitions in vitro using SLP-76 plus Gads or PLCγ1 have failed to produce extensive condensation (*42*, *58*). However, these experiments did not include ADAP, and the SAM domain of SLP-76 was truncated off. Including either or both of these could drastically change the experiment outcomes. In summary, SLP-76 possesses a variety of ways to indirectly oligomerize LAT and is a likely candidate for providing the crosslinking needed for PLCγ1-mediated nucleation of LAT condensates.

Another possibility is that the SH3 domain of PLCγ1 may bind SOS, engaging in crosslinking similar to Grb2:SOS. A study in 2007 reported that isolated PLCγ1 SH3 domain can bind SOS-derived PR peptides with ~30μM affinity (*111*). Reconstitution experiments have revealed that SOS enhances PLCγ1:LAT clusters on supported membranes (*58*). How frequent and relevant these interactions are in the cell is not understood. For instance, the effective affinity of PLCγ1(SH3) to SOS(PR) will be lower in the presence of other competitive binders (e.g., SLP-76 binding PLCγ1(SH3) and Grb2 binding SOS(PR)). Zeng and colleagues have shown that titrating SLP-76 concentration completes off SOS binding to PLCγ1 (*58*). Furthermore, cytosolic Grb2 concentration is an order of magnitude higher than PLCγ1 (*117*). Thus, even if their affinities were identical, Grb2 has a comparative advantage to bind SOS due to greater abundance.

Taken together, there are multiple plausible mechanisms for how PLCγ1 could facilitate early crosslinking to nucleate LAT condensates. Which of these mechanisms play the dominant role is unknown and requires further experimentation. Additionally, none of these mechanisms are mutually exclusive. Based on available data, we propose that PLCγ1 facilitates nucleation through the recruitment and oligomerization of SLP-76, either via its SAM domain, ADAP, trans tertiary complex binding, or a combination of the three (**Figure 3-12**).

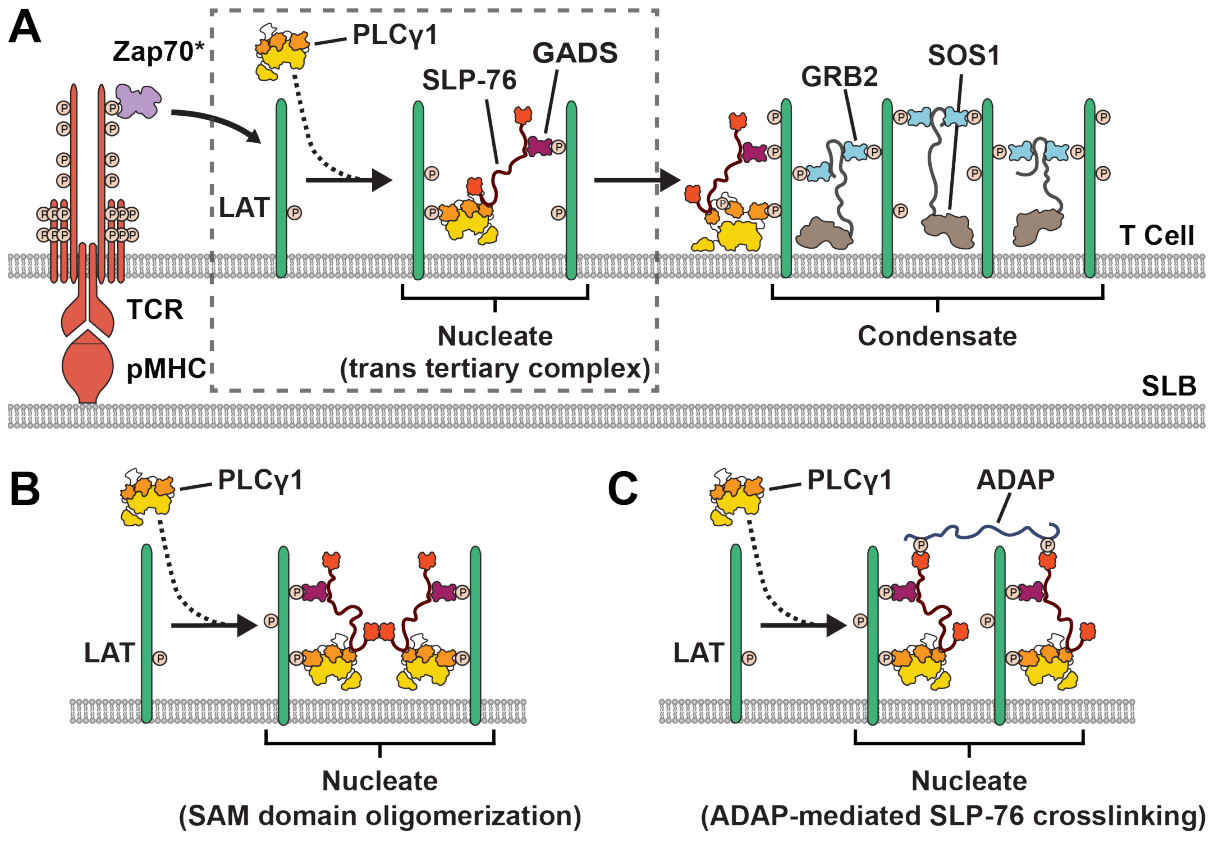

Figure 3-12: Models of PLCγ1-mediated LAT condensate nucleation with SLP-76.
This schematic portrays plausible mechanisms of PLCγ1-mediated nucleation of LAT condensates using SLP-76 to facilitate crosslinking. Following single pMHC:TCR binding, Zap70 begins phosphorylating LAT. Once LAT Y136 is phosphorylated, autoinhibited PLCγ1 recruits to Y136 and mediates early crosslinking

to form a LAT nucleate. The nucleate then rapidly grows into a mature LAT condensate. Early crosslinking could occur through (A) trans tertiary complex binding, (B) SAM domain oligomerization, or (C) ADAP-mediated crosslinking of SLP-76.

Additionally, we demonstrated that LAT Y136 is uniquely important for condensate nucleation. What makes this residue so unique for this role is not fully understood; however, our chimeric tdSH2 data implication the importance of LAT valency. Historically, Y136 has not been thought to participate in LAT crosslinking, and it increases LAT valency from the traditional three Grb2 binding sites (Y175, Y195, Y235) to four. The tdSH2(GG) construct can only bind the three Grb2 sites and, therefore, can only crosslink and condense LAT in a trivalent fashion, assuming all tyrosine sites are phosphorylated and occupied (**Figure 3-13**, middle). This represents the traditional view of LAT crosslinking by Grb2:SOS. Conversely, tdSH2(PG) can engage all four pTyr residues, effectively increasing LAT valency to a maximum of four. The left panel of **Figure 3-13** depicts a model condensate in which LAT is maximally crosslinked with four valency sites. As can be seen, the number of LAT molecules and the multiplicity of binding sites after just two degrees of growth from the central LAT molecule (the green dot with grey outline) are far greater compared to trivalent LAT maximally occupied (shown in the middle panel). However, the likelihood that every LAT molecule will be fully saturated is very low, as this represents a single possible microstate of LAT occupancy and crosslinking. It is far more likely that some LAT will be slightly subsaturated, and that LAT molecules will be more interconnected. The middle panel of **Figure 3-13** also represents a model of tetravalent LAT partially occupied, which is more likely (i.e., greater entropy). Both maximal (left panel) and partial (right panel) occupancy of tetravalent LAT still allows for substantial two-dimensional condensation. Conversely, partial occupancy with trivalent LAT most likely fails to achieve 2-dimensional condensation, as exemplified in the right panel of **Figure 3-13**. Therefore, we propose that Y136 is critical to condensate nucleation and stability because it provides the critical fourth valency site, and that in vivo two-dimensional LAT condensation phase transition requires a valency of four. It is important to note that these condensates are under kinetic control. Therefore, these toy models, which also inaccurately depict LAT as a stiff rod, do not fully describe the condensation process but are conceptually useful. Stochastic simulations of how different LAT valency affects two-dimensional phase transition would be very informative.

Another possibility is allostery and tyrosine accessibility. Previous work from our laboratory has suggested that LAT can adopt higher order structures that sterically obstruct tyrosine residues from phosphorylation (*35*). Phosphorylation at one site allosterically increased the rate of phosphorylation at subsequent tyrosine sites and so on. Y136 phosphorylation may have a stronger allosteric effect than the other tyrosine residues accessible. However, our data imply that crosslinking, and not simply binding LAT at phospho-Y136, is required for nucleation.

Finally, the unique positioning of Y136 proximal to the plasma membrane could be an important factor in nucleation. A recent study exploring the importance of LAT tyrosine ordering found that when Y132 (the human equivalent of Y136) is placed at the membrane distal end of LAT, Y226 (the human equivalent of Y235) phosphorylation was significantly attenuated, which would likely affect condensation (*125*).

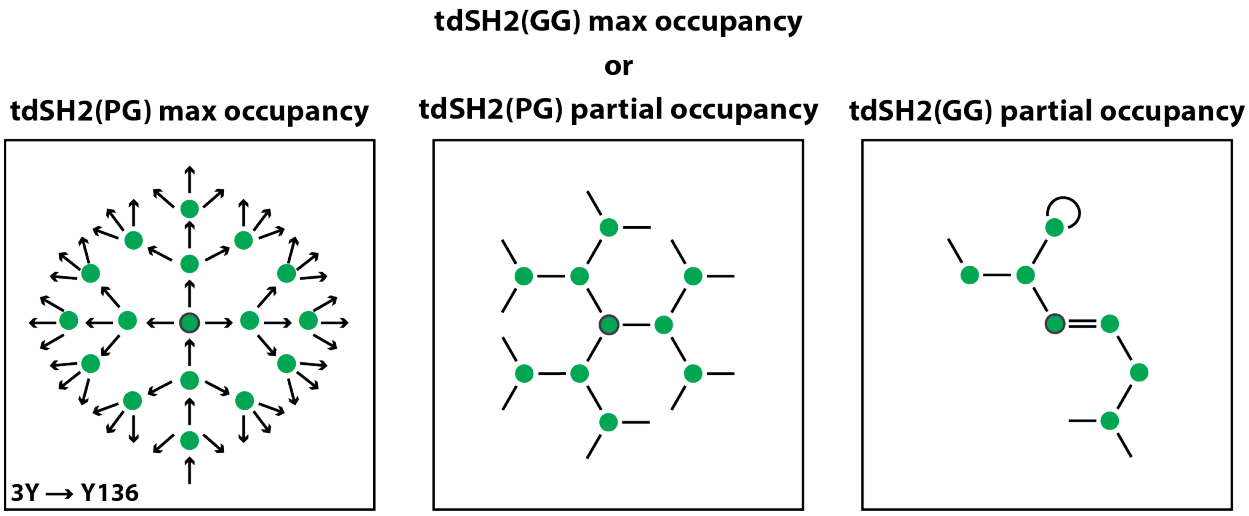

Figure 3-13: LAT valency of four enhances LAT condensation.
Schematic depicting different LAT valency models. Green circles represent individual LAT molecules, and black lines connecting LAT nodes represent a crosslink. Model condensates are only grown two LAT molecules out from the central LAT node (gray outline). Occupancy refers to the number of crosslinkers bound to LAT. (Left) LAT with a valency of four and maximum occupancy. This model represents what may be observed with the tdSH2(PG) construct, which can crosslink LAT with all four tyrosines. The arrows represent the directional binding of tdSH2(PG), with arrowheads indicating binding to Y136. This also roughly represents crosslinking achieved by PLCγ1$_{FL}$, except not all crosslinks would be required to involve Y136 (e.g., traditional Grb2:SOS linking). (Middle) LAT with a valency of three and maximum occupancy or valency of four and partial occupancy. This model represents what may be observed with the tdSH2(GG) construct, which can only crosslink LAT with three tyrosines similar to the traditional view of LAT crosslinking by Grb2:SOS. This also represents an example of partial occupancy (one less than max) with a valency of four. (Right) LAT with a valency of three and partial occupancy fails to yield a two-dimensional condensate.

In summary, we report the discovery that PLCγ1 nucleates and controls the timing of single pMHC:TCR-induced LAT condensates upstream of its lipase function. PLCγ1 plays a pivotal role in regulating and gating LAT condensation and, therefore, TCR antigen sensitivity. Our data provide a clear picture of key molecular features of PLCγ1 that are required to accomplish this. In lymphocytes, PLCγ1 is primarily expressed in T cells, while its isozyme PLCγ2 is predominant in B cells. We are interested in investigating whether PLCγ1 and PLCγ2 exhibit similar structural roles in controlling signaling in other receptor pathways and cell types such as EGFR and BCR signaling.

This work has the potential to improve the design of modern immunotherapeutics. Therapies could be developed to increase or decrease antigen sensitivity by exploiting the structural role of PLCγ1 without inhibiting its catalytic function. In cancer immunotherapy, reliably targeting T cells to solid tumors has proven difficult (*126*–*129*). In this scenario, increasing T cell antigen sensitivity by expressing SHarray construct variants may be beneficial. In the case of autoimmune disease, decreasing sensitivity could be achieved by impeding condensate nucleation using a construct such as tdSH2(GG). Finally, mutations in PLCγ1 are the most prevalent in adult T cell leukemia and lymphoma, appearing in ~36% of patients (*130*, *131*). While many of these mutations are expected to destabilize autoinhibition, it may be worthwhile to investigate whether any mutations are tied to this newly discovered PLCγ1 function.

4 | LAT condensate regulation and using supported bilayers to study immunotherapeutics

Abstract

LAT condensation is positioned at a critical juncture in the TCR signaling pathway. LAT translates antigen information from pMHC and transforms it into various bifurcating signaling pathways. As such, LAT condensation is highly regulated to avoid spurious activation. We report that calcium depletion greatly accelerates condensate delay time, indicating a potential negative feedback loop that is activated when calcium flux elevates cytosolic levels. Jurkat T cells lines display a wide range of basal LAT clustering, underscoring the need for careful characterization of LAT clustering when performed such studies in Jurkats. Tumor-targeted bispecific antibodies studied on support membranes reveal robust TCR binding and T cell activation regardless of TCR clonotype and a moderate tolerance for a small range of antigen molecule height. Finally, cortical actin actively accumulates at sites of non-TCR-induced LAT condensation, providing a safety mechanism against spurious LAT condensation by blocking PLCγ1 from accessing PIP_2 substrate. Actin accumulation at condensates is depolarized by CD28-induced actin remodeling, allowing downstream signal propagation. These preliminary data provide valuable insights into LAT condensate regulation and highlight the utility of supported membranes to study cancer immunotherapeutics.

Introduction

This chapter represents a compilation of preliminary data centered around TCR signaling and LAT condensation with promising prospects for future research efforts. Chapters 2 and 3 demonstrated that the LAT condensation phase transition plays a critical role in TCR signaling and antigen discrimination. As such, LAT condensation is highly regulated to avoid spurious activation. For instance, constant pressure from PTPs helps prevent resting T cells from spontaneously activating by ensuring TCR ITAMs and LAT remain unphosphorylated (*37*). Additionally, LAT ubiquitinylation by the E3 ubiquitin ligase c-Cbl leads to enhanced LAT internalization and trafficking away from the plasma membrane (*132*, *133*). Understanding condensate regulation is essential for building a complete picture of antigen discrimination and informing the productive design of cancer immunotherapeutic agents.

We report a potential negative feedback loop caused by TCR-induced calcium flux. Productive TCR signaling results in elevated calcium levels, which acts as a second messenger to propagate signaling. Depleting extra- and intra-cellular calcium reservoirs causes a dramatic decrease in LAT condensate delay time. We suspect that TCR-induced calcium flux produces the inverse effect. This depicts calcium playing a dual role in propagating the earliest signals and suppressing further input.

We describe observations of LAT clustering in Jurkat T cell lines. Some Jurkat lines produce large numbers of LAT clusters in the absence of TCR stimulation. Pharmacological inhibitor studies suggest integrin signaling, through ICAM-1:LFA-1, is responsible for the high levels of basal clustering. Interestingly, different sources of parental Jurkat lines exhibit minimal LAT clusters in resting cells, similar to primary T cells. This underscores the importance of judiciously interpreting clustering studies performed in Jurkats as well as thorough characterization of Jurkat lines prior to such experimentation.

We utilize the supported lipid bilayer platform to characterize bispecific antibody (biAb) stimulation of primary T cells and Jurkats. Bispecific antibodies are a cancer immunotherapeutic reagent that crosslinks a T cell's TCR with a tumor-associated antigen. Thus, in these experiments, the SLB mimics a tumor cell surface. The biAb effectively binds and activates T cell, as determined by NFAT nuclear translocation, regardless of TCR clonotype. BiAb stimulation also effectively activates cells within a certain tolerance range of intermembrane spacing.

Finally, we present findings that the cortical actin cytoskeleton actively accumulates at sites of spontaneous (i.e., non-TCR induced) LAT condensation, presumably to block PLCγ1 from accessing PIP_2 substrate as suggested by Csk inhibition studies. This accumulation is mitigated by additional actin reorganization induced by CD28 stimulation. This implicates that actin provides a safety mechanism to prevent spurious activation, which is released by further signaling input. Collectively, all these results reveal that many well-known proteins and second messengers play critical auxiliary roles regulating LAT condensation and signaling.

Calcium-induced negative feedback loop on LAT condensation timing

Introduction

Calcium is a critical second messenger in T cell signaling. After recruiting to LAT and becoming activated, PLCγ1 catalyzes the cleavage of PIP_2 lipids to produce IP_3 and DAG. Soluble IP_3 binds to IP_3 receptors in the endoplasmic reticulum (ER) membrane. This ultimately causes elevated cytosolic calcium levels as calcium is released from ER stores and enters the cell through calcium ion channels in the plasma membrane (*108*). This activates the phosphatase calcineurin, which dephosphorylates NFAT, enabling nuclear translocation and cytokine transcription. Therefore, calcium stands at the midpoint between LAT condensation and transcription factor activation. How calcium integrates individual condensate input, what calcium flux signatures are required for NFAT activation and translocation, and how calcium may affect upstream signaling is generally unknown.

Chapter 3 exemplified how signaling proteins may exhibit additional critical functions upstream of their traditional role. PLCγ1 plays a key role in nucleating LAT condensates by facilitating early crosslinking. We are interested in determining if other proteins or second messengers similarly regulate upstream signaling, particularly with regards to LAT condensation. A recent study demonstrated that under high antigen stimulation in Jurkat cells, the kinetic lag between the Zap70 and Grb2 clustering was tunable by titrating the extracellular calcium concentration (*70*). Lower calcium concentrations decreased the ensemble kinetic lag, while higher calcium concentration resulted in a longer lag time. If true, this could constitute a calcium-mediated negative feedback loop. However, as explained in Chapters 2 and 3, saturating TCR stimulation can produce artificial protein clustering and timing results. Therefore, it is imperative that these results are tested and verified under physiological, single molecule TCR triggering conditions.

Cytosolic Calcium Concentration Modulates LAT Condensation Timing

To accomplish this, we depleted T cells of their intracellular calcium reservoirs and quantified how this perturbation affected LAT condensate delay time. Primary murine T cells expressing LAT-EGFP were treated with 1mM EGTA for 20 min (see Methods). EGTA is membrane permeable and selectively chelates and sequesters calcium ions (*134*). Cells were then added to SLBs containing single molecule pMHC densities and imaged in calcium-free live cell imaging buffer. The results were very striking as calcium-depleted T cells produced far more condensates compared to untreated cells (**Figure 4-1A**). LAT condensates formed rapidly in response to single pMHC:TCR binding events (**Figure 4-1B**). Individual condensate delay times demonstrated that calcium depletion greatly accelerated LAT delay time kinetics (**Figure 4-1C**). In fact, calcium depletion had

the strongest effect on LAT condensate delay time of all methods discovered thus far (i.e., LAT(G135D) and PLCγ1 overexpression). Furthermore, the rate of condensate production more than doubled (**Figure 4-1D**).

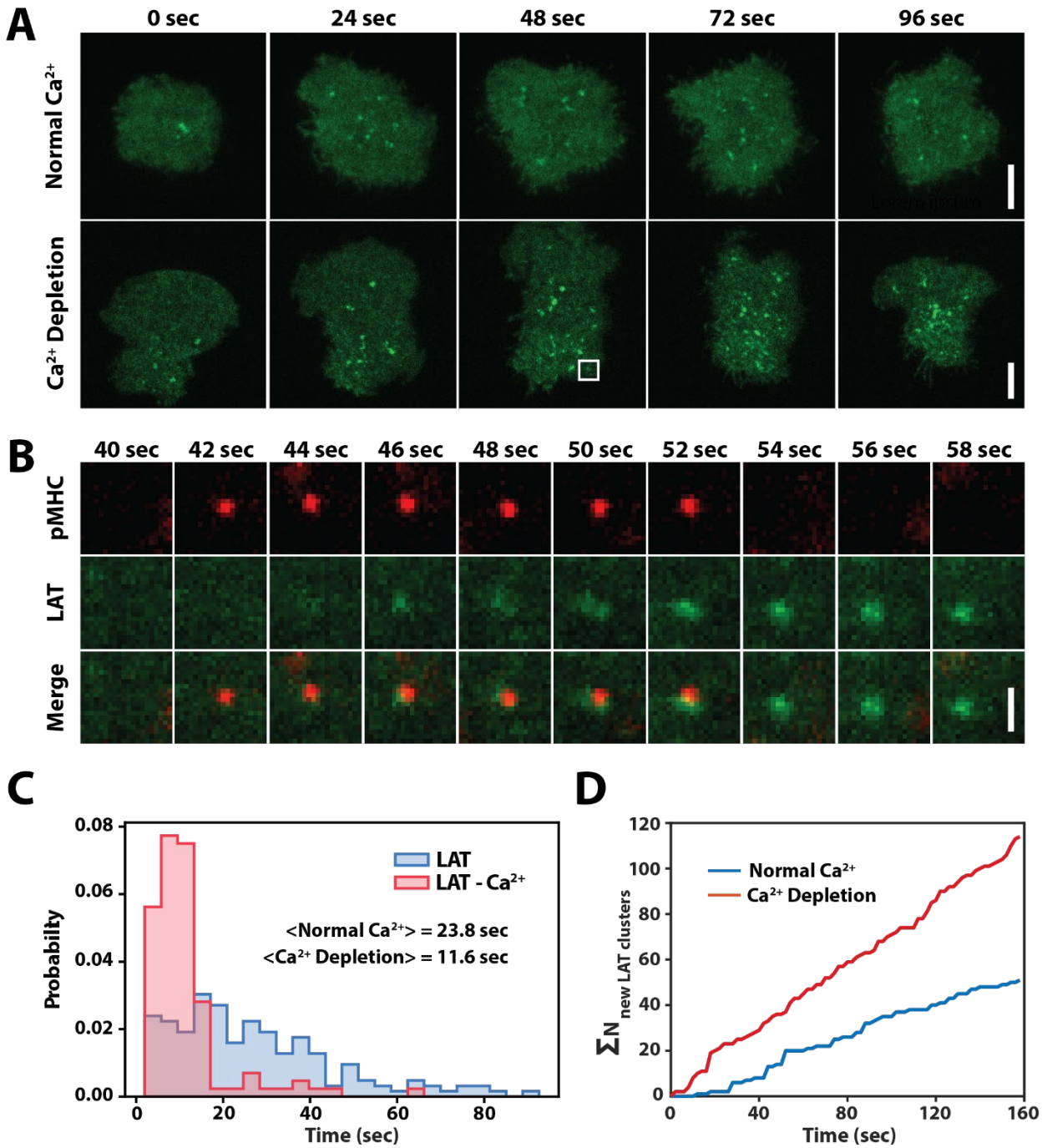

Figure 4-1: Calcium influences LAT condensate delay time.
(A) TIRF image time series of LAT condensation in primary murine T cells in normal or calcium-depleted conditions. (Top) Images of a T cell under normal calcium conditions expressing LAT-EGFP (green) placed on a supported membrane containing MCC(Atto647)-MHC (not shown). (Bottom) Images of a T cell under depleted calcium conditions expressing LAT-EGFP (green) placed on a supported membrane containing

MCC(Atto647)-MHC (not shown). Intracellular stores were depleted with EGTA, and cells were imaged in calcium-free live cell imaging buffer. Top and bottom bars are 5μm. (B) Zoom-in of the box in A (bottom). Image time sequence of single molecule MCC(Atto647)-MHC (red) binding TCR and inducing a LAT (green) condensate after a shortened delay in depleted calcium conditions. Bar is 1μm. (C) LAT condensate delay time distribution in calcium-free conditions (red) overlayed onto the delay time distribution measured under normal calcium conditions (blue). (D) An anecdotal example of the rate of LAT condensate appearance under normal (blue) and calcium depleted (red) conditions. Each trace comes from a single cell.

To verify that EGTA treatment actually depleted calcium stores, we imaged NFAT nuclear translocation. EGTA-treated and untreated cells expressing NFAT-mCh-P2A-LAT-EGFP were placed on stimulating supported membranes for 30 min, after which we imaged both the state of LAT condensation and NFAT translocation. All cells treated with EGTA failed to translocate NFAT despite the large number of condensates formed (**Figure 4-2A** and **B**). Untreated cells, on the other hand, robustly activated. This is expected since NFAT activation and translocation are immediately dependent on calcium flux; therefore, confirming that EGTA treatment successfully depleted intracellular calcium in our experiments. EGTA treatment had no apparent ill effect on cell health nor caused observable changes in cellular morphology (**Figure 4-1A**, bottom vs. bottom row).

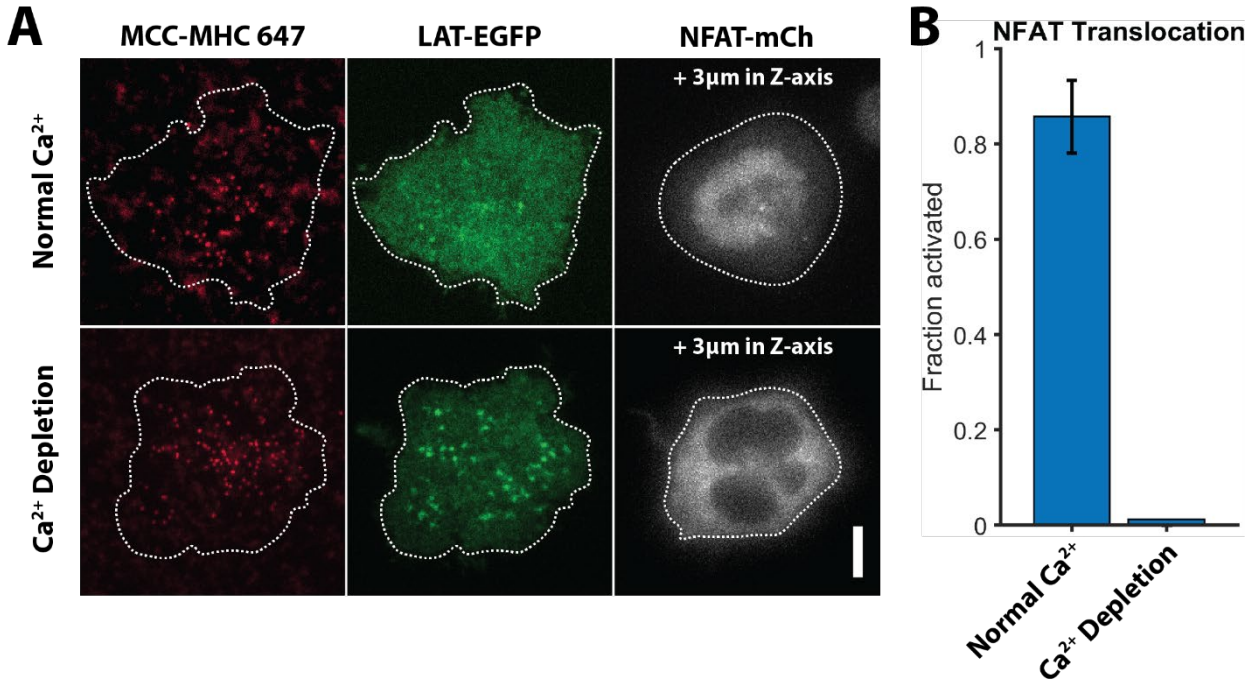

Figure 4-2: EGTA treatment precludes NFAT translocation.
(A) Representative images of T cells activating or failing to activate under different calcium conditions. Primary murine T cells co-expressing NFAT-mCh (gray) and LAT-EGFP (green) were placed on SLBs containing MCC(Atto647)-MHC (red) for 30 min. MCC(Atto647)-MHC and LAT-EGFP were imaged by TIRF, and NFAT-mCh was imaged by epifluorescence at 3μm above the plane of the SLB. (Top row) Representative images of a T cell under normal calcium conditions showing NFAT translocated into the nucleus. (Bottom row) Representative images of a T cell under depleted calcium conditions showing NFAT remaining in the cytosol. Bar is 5μm. (B). Bar plot of the fraction of activated T cells under different calcium conditions. T cells were stimulated for ~30 min on an MCC-MHC (0.5-0.7 molecules/μm^2) containing bilayer.

~85% of T cells under normal calcium conditions activated, which is expected for this density of pMHC, while all T cells depleted of calcium failed to translocate NFAT. More than 20 cells for each condition.

Discussion

A major question posed by these results is how calcium is acting to influence LAT condensation. There are several calcium-dependent proteins involved in T cell signaling. For instance, PLCγ1 activity is dependent on a calcium cofactor present in the TIM-barrel active site, which coordinates inositol headgroups (*135*). Mutation of a histidine residue that chelates the calcium ion results in a catalytically dead enzyme (*136*). Since calcium depletion yields PLCγ1 catalytically inactive while simultaneously enhancing LAT condensation, this corroborates our data presented in Chapter 3 that PLCγ1 activity is not required for nucleation of LAT condensates. PLCγ1 also has a calcium-dependent EF motif region and a C2 domain. Calcium binding and unbinding causes conformational changes to EF hand motifs; however, their exact function in PLCγ1 is unknown. Deletion or mutation of EF hands in PLCζ leads to a decrease or loss of activity (*137*). C2 domains bind negatively charged lipids in a calcium-dependent manner (*138*). Deletion of C2 from PLCζ also results in loss of activity (*137*). Again, the full function of the C2 domain in PLCγ1 signaling is unclear. It appears from data on other PLC enzymes that calcium mainly regulates enzymatic activity. Therefore, we suspect that calcium's effect on LAT condensation does not occur through PLCγ1.

As mentioned above, calcium flux activates the phosphatase calcineurin, whose primary function is to dephosphorylate and active NFAT. In a recent study, researchers discovered that calcineurin can bind TCR complexes and reverse an inhibitory phosphorylation at serine 59 on Lck (*139*). Inhibition of calcineurin activity resulted in impaired Y493 phosphorylation on Zap70, which is required for Zap70 activation (*140*). Therefore, calcineurin activation appears to enhance TCR signaling, which is not consistent with calcium-induced negative feedback.

Calcium has also been observed to bind PIP_2 lipids (*141*). Bilkova and colleagues found that calcium can bind and bridge PIP_2 headgroups, essential leading to their sequestration. Calcium bridging of PIP_2 precludes binding of the PLCδ1 PH domain. How PIP_2 sequestration could influence LAT condensation is not clear, though it could act through lipid microdomain partitioning or electrostatic effects.

Taken together, our data support a hypothesis that modulating cytosolic calcium levels, either by calcium influx due to TCR signaling or export through ion pumps, regulates LAT condensate delay time and formation. This represents a novel calcium flux-induced negative feedback loop in TCR signaling. As summarized in **Figure 4-3**, following TCR triggering and LAT condensation, PLCγ1 ultimately causes calcium influx. We suspect that elevated calcium concentration in the cytosol induces upstream negative feedback on subsequent pMHC:TCR binding events by elongating LAT condensate delay time, thus causing a higher kinetic threshold. This may also represent a safety mechanism against spurious activation. Thus, only true, sustained TCR signaling would be capable of surpassing signaling thresholds. The exact mechanism of how calcium is influencing

upstream kinetic steps is yet unknown and requires further investigation. For instance, in vitro reconstituted LAT phase transition experiments may inform how calcium influences condensate formation and structure.

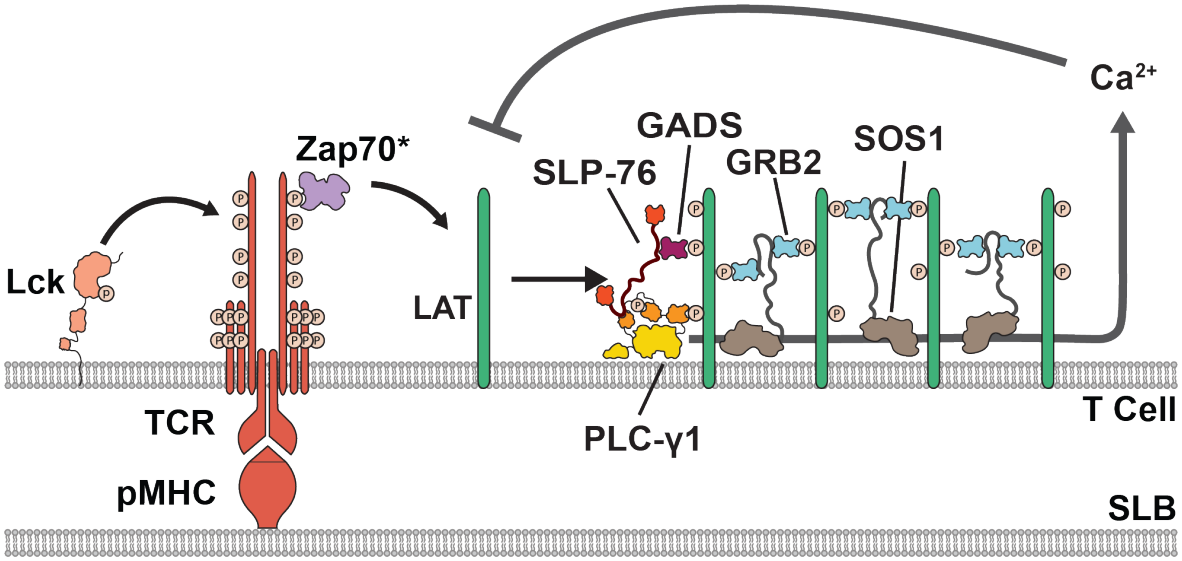

Figure 4-3: Model of calcium-induced negative feedback.
After pMHC:TCR binding, Zap70 recruitment, and a delay to LAT condensation, activated PLCγ1 produces IP_3 leading to calcium flux. Elevated calcium levels are suspected to engage in a negative feedback loop to inhibit subsequent upstream signaling events, presumably by increasing the kinetics threshold for productive TCR signaling to condense LAT.

LAT condensation in Jurkat T cells

Introduction

Jurkat T cells are widely used in immunological research, and data obtained from these cells can be found throughout T cell literature. Jurkats are an immortalized human T cell line derived from a 14-year-old leukemia cancer patient (*142*). There are many advantages to using Jurkats over primary T cells. For instance, Jurkats quickly proliferate, are easily transfected with proteins of interest, and are straightforward to genetically manipulate. This final point is a significant advantage over primary cells, which often require genetic engineering at the level of the embryo to obtain T cells with a desired genetic background. Jurkats also have known disadvantages arising from misregulated tumor pathways, such as deficiencies in PTEN and SHIP phosphatases (*142*). The cognate pMHC ligand for the Jurkat TCR is also unknown. Regardless, Jurkats provide a powerful platform for studying T cell signaling and LAT condensation using loss-of-function mutation and knock-out studies. Therefore, we aimed to characterize LAT condensation in Jurkat cells.

Some Jurkat Lines Exhibit High Levels of Basal LAT Cluster

To accomplish this, we first investigated basal LAT condensation behavior (i.e., in the absence of TCR stimulation). Primary T cells on SLBs containing only ICAM-1 show only a handful of condensates, in any, over the course of several minutes (**Figure 4-4A**, top row). This quiet basal state of LAT is a very robust feature in primary cells. Next, we placed Jurkats cells stably expressing LAT-EGFP onto supported bilayers displaying only human ICAM-1. Surprisingly, we observed a large number of basal LAT clusters in the Jurkat cells (**Figure 4-4A**, second row). Such excessive clustering would make the identification of true TCR-induced condensates difficult. Therefore, we aimed to identify and tune down the source of basal clustering in Jurkats.

We first attempted a noninvasive approach by serum starving the cells before imaging. This is a common practice in T cell experiments to place the cells in the quietest signaling state possible by removing all sources of potential stimulation. A short 20 min serum starvation had no effect on attenuating LAT clusters (data not shown). Performing a 20-hour serum starvation before adding Jurkats to ICAM-1 SLBs likewise had no effect (**Figure 4-4A**, third row).

Next, we employed pharmacological agents to inhibit specific signaling pathways. PP2 selectively inhibits the Src-tyrosine kinase Lck, which initiates TCR signaling by phosphorylating TCR ITAMs as well as Zap70. The IC_{50} value of PP2 for Lck is 4nM (*143*). PP2 also inhibits the Src kinases Fyn and Hck. To ensure complete inhibition of Lck, we incubated Jurkat cells with 4μM PP2 for 30-45 min before adding the cells to ICAM-1-containing bilayers. Surprisingly, the level of basal LAT clustering did not decrease

(**Figure 4-4A**, fourth row). This suggests that these basal clusters do not originate through the TCR unless it is being bypassed.

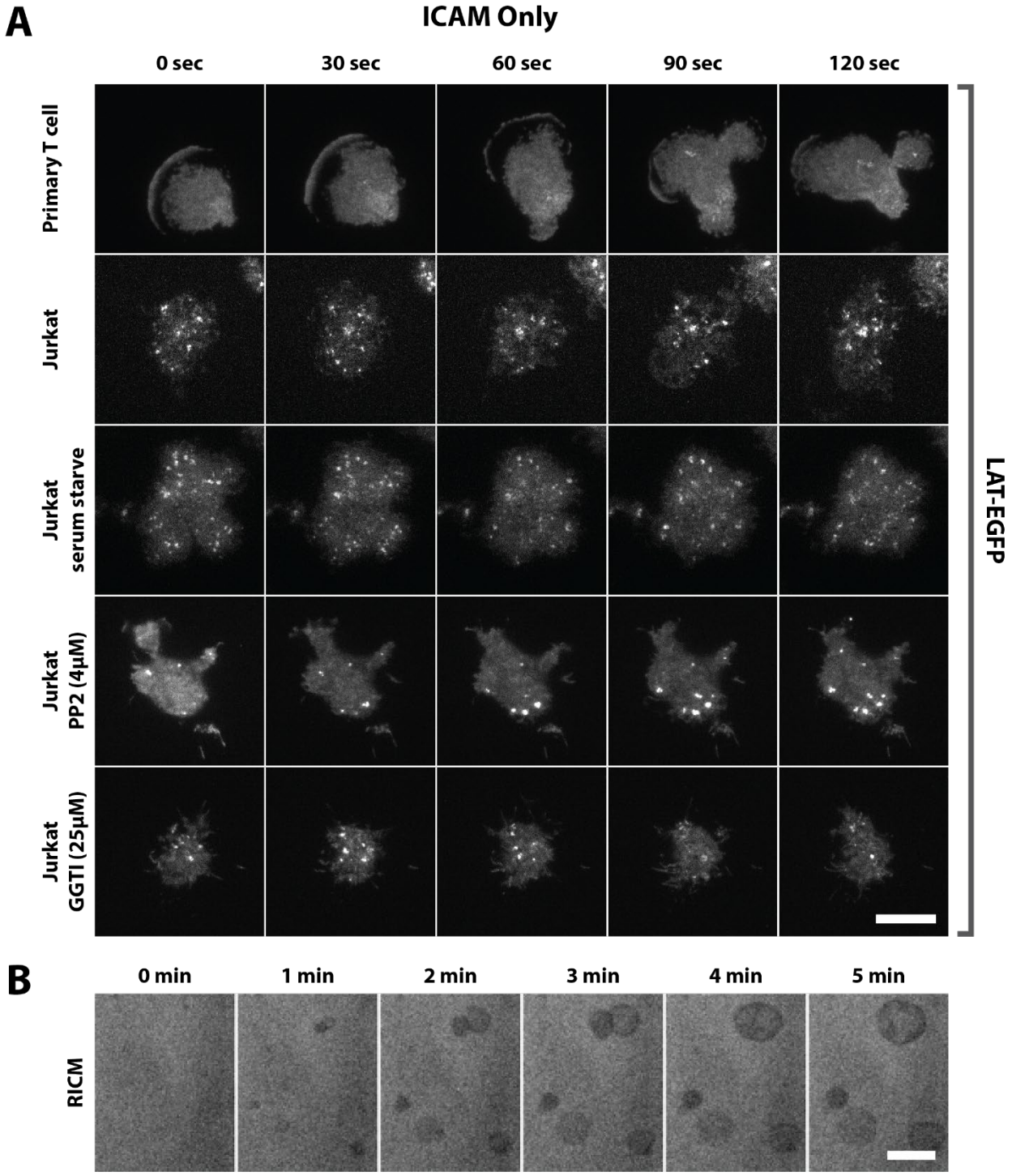

Figure 4-4: Basal LAT condensation in Jurkats cells.
(A) Representative TIRF image time series of basal (no TCR simulation) LAT clustering in Jurkat T cells under various conditions. (Top row) Primary murine T cells expressing LAT-EGFP interacting with a

supported lipid bilayer containing only murine ICAM-1 show little to no LAT clustering. (Second and all subsequent rows) Jurkat T cells expressing LAT-EGFP interacting with a supported membrane containing only human ICAM-1. This line of Jurkats exhibited high levels of basal LAT clustering. (Third row) Jurkat cells after 20-hour serum starvation still exhibited a high degree of LAT clustering. (Fourth row) Jurkat treated for 30-45 min with 4μM Src-kinase inhibiter PP2 still showed high levels of LAT clustering. (Bottom row) Jurkat treated for 30-45 min with 25μM Rap1 inhibiter GGTI still showed high levels of LAT clustering, though clusters appeared more unstable. Bar is 10μm. (B). RICM image time series of GGTI-induced membrane blebbing of the supported lipid bilayer. Bar is 2μm.

We then aimed to prevent LAT clustering originating from ICAM-1:LFA-1 signaling by inhibiting Rap1. Rap1 is a small, membrane-associated GTPase that regulates the binding strength of ICAM-1:LFA-1 interactions. Specifically, activation of Rap1 induces conformational changes in LFA-1 that increase its affinity for ICAM-1 ligand (*144*). Therefore, we reasoned that mitigating ICAM-1:LFA-1 affinity by Rap1 inhibition may reduce integrin-mediated LAT clusters. The inhibitor GGTI blocks geranylgeranylation of Rap1 and possesses an IC_{50} of 2μM (*145*). Treating Jurkats with up to 25μM GGTI failed to prevent excessive basal LAT clustering (**Figure 4-4A**, bottom row). However, of all the conditions tested, GGTI qualitatively had the strongest effect, as basal clusters appeared more diffuse and destabilized. However, the concentration of GGTI used (25μM) caused significant cell death. It is also worth noting that GGTI caused blebbing of the supported lipid bilayer, observable in RICM, and affected cell adhesion with the bilayer (**Figure 4-4B**). It is possible that low affinity ICAM-1:LFA-1 interactions are still sufficient to induce LAT clustering, albeit more weakly.

We additionally tested a parental Jurkat line from another vendor. Jurkats were transfected with LAT-EGFP and placed on supported bilayers containing only ICAM-1. Intriguingly, these cells showed substantially lower basal LAT clustering, comparable to primary cells (**Figure 4-5A**, first four frames of the montage). This demonstrates that basal LAT clustering in Jurkat cells is highly variable depending on the source of the cell lines. It is not fully clear what causes high basal clustering, if clusters exist while cells are in solution, or why cell lines exhibit such broad variability. It is important, therefore, to consider how these findings may influence the interpretation of data obtain from Jurkats, especially imaging-based experiments studying protein clustering on the plasma membrane. Fortunately, some Jurkat lines possess low basal clustering and can be used in single molecule studies, as we have done with primary cells.

Pervanadate Inhibits LAT Condensation While Enhancing Tyrosine Phosphorylation

T cells express several protein tyrosine phosphatases (PTPs) that exert negative pressure on TCR signaling by counteracting tyrosine kinases driving signaling forward (*37*). We were interested in observing the effect of phosphatase inhibition on LAT condensation in Jurkats. Therefore, we treated cells with the potent general PTP inhibitor pervanadate (perV). Pervanadate irreversible oxidizes the catalytic cysteine residue of PTPs and has been shown to dramatically increase tyrosine phosphorylation in Jurkats in the absence of TCR stimulation (*146*, *147*). PerV is used ubiquitously in T cell signaling literature as a means of activating T cells. We anticipated that upon adding perV to cells,

LAT would spontaneously condense. Much to our surprise, upon adding perV, existing LAT condensates decayed to background levels, and no new condensates formed (**Figure 4-5A**). This suggests that PTP inhibition by perV had an inhibitive effect on condensation. Many studies have shown, however, that perV treatment induces extensive tyrosine phosphorylation and cellular activation (*146*, *147*). To verify that our preparation of perV was, in fact, causing tyrosine phosphorylation, we ran the same population of cells imaged in **Figure 4-5A** on a western blot and stained for phosphotyrosine. As expected, perV triggered substantial spontaneous tyrosine phosphorylation (**Figure 4-5B**, right). These data indicate that perV activates T cells in a LAT condensate-independent manner. Meaning that under these conditions, signaling from LAT occurs at the monomeric level or by bypassing LAT altogether.

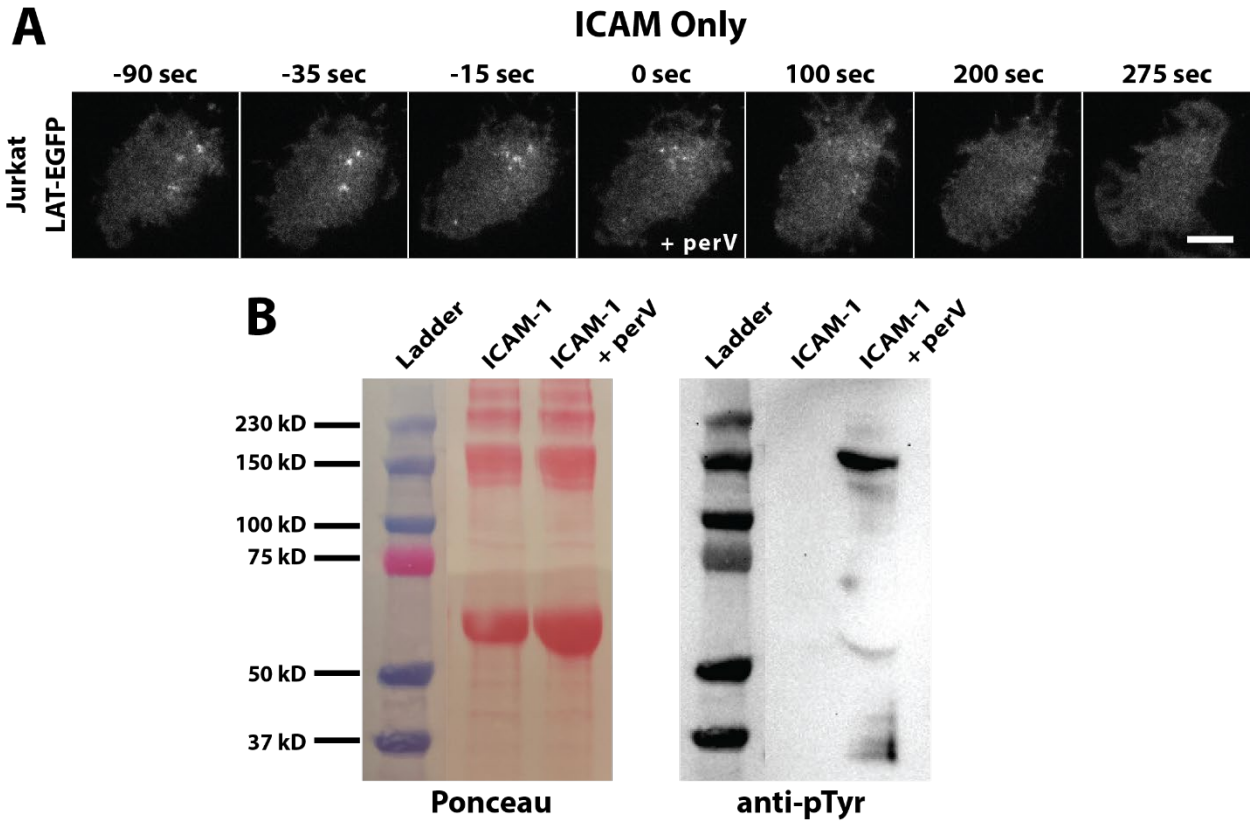

Figure 4-5: Pervanadate inhibits LAT condensation while increasing tyrosine phosphorylation. *(A) TIRF image time series of a different Jurkat cell line expressing LAT-EGFP on an SLB containing only human ICAM-1. Pervanadate (perV) was added at the indicated frame. Bar is 5μm. (B) Pan-phosphotyrosine western blot of Jurkats treated with and without perV. Jurkat cells interacting with SLBs containing only ICAM-1 were treated with or without perV for 30 min followed by cell lysis and SDS-PAGE gel electrophoresis. (Left) Ponceau stain of nitrocellulose membrane after protein transfer. Ponceau stain shows total protein content and loading. ICAM-1 and ICAM-1 plus perV lanes were loaded roughly equally with whole cell lysate, though ICAM-1 plus perV did have somewhat more. (Right) Anti-pTyr antibody stain detected with horseradish peroxidase-conjugated secondary antibody. ICAM-1 cells showed no detectable signs of basal pTyr, while the ICAM-1 plus perV condition showed a significant increase in tyrosine phosphorylation. The cell imaged in A was part of the cell population used for the ICAM-1 plus perV lane.*

Discussion

We report the observation that some Jurkat T cell lines possess high levels of LAT clustering in the absence of antigen stimulation. The source of high basal clustering is largely unknown, though there are several plausible suspects. One possibility is the potential misregulation of kinases and phosphatases. Inhibition by PP2 suggests that these clusters either do not originate from TCR or bypass ITAM phosphorylation by Lck. It is possible that other non-Src family kinases may be causing ITAM phosphorylation, such as Tec-family kinases, though this has not been observed in experiments. Perhaps Zap70 possesses unusually high basal activity in this cell line. PTEN and SHIP phosphatases are already known to be misregulated in Jurkats.

In primary cells, we observe that a few LAT condensates form in the absence of pMHC binding. Some of these LAT clusters form from LAT/VAMP7-enriched vesicles docking at the plasma membrane (**Figure 2-5C**), and others from ICAM-1:LFA-1 induced clustering (**Figure 2-5D**). Raab and colleagues propose the existence of compositionally distinct LAT clusters, formed orthogonally by TCR and ICAM-1:LFA-1 signaling (*90*). Therefore, excessive LAT clustering in Jurkats on SLBs containing only ICAM-1 may arise from overactive IFA-1 signaling. Rap1 inhibition failed to fully block basal LAT clustering, though clusters were diffuse and unstable. This is the strongest effect we observed and may indicate that LFA-1 signaling plays a role in basal clustering.

Lastly, LAT may exist in a pre-clustered state in some Jurkat lines. Three-dimensional imaging of Jurkats in solutions would be required to assess whether this is the case. If true, it is surprising that western blot studies show little detectable LAT phosphorylation in the absence of TCR triggering (*50*). Taken together, we speculate that high basal LAT clustering in some Jurkat cell lines is due to ICAM-1:LFA-1 signaling, though this needs to be confirmed with further investigation.

As discussed earlier, the utility of genetically manipulating Jurkats is highly valuable for dissecting mechanistic details of T cell signaling and LAT condensation. Fortunately, some parental Jurkats exhibit basal LAT clustering levels comparable to primary cells. This fortuitous discovery allowed us to perform perturbation studies such as the PLCγ1 knock-down experiment detailed in Chapter 3 (**Figure 3-4**). Since the degree of basal LAT clustering in Jurkats is so variable, it is imperative that thorough characterization is performed in experiments investigating membrane protein clustering. It is not known whether high basal clustering causes Jurkats to activate in the absence of TCR stimulation, but, given the relationship between the number of LAT condensates and NFAT activation, it is likely (**Figure 2-10C**, Chapter 2).

Finally, we made the surprising observation that pervanadate treatment appeared to suppress LAT condensation. Pervanadate is used by many researchers to artificially induce tyrosine phosphorylation (*146*, *147*). We anticipated that perV would cause spontaneous phosphotyrosine-driven LAT condensation. Our result indicates that perV activates T cells in a condensate-independent manner. The exact mechanism is currently under investigation though we offer the following speculations. Under perV treatment,

LAT is likely fully phosphorylated and trapped in a monomeric state. One study suggests that phosphorylation of Grb2 at Y160 disrupts Grb2 dimerization, which may be important for driving condensation (*148*). However, this same study suggested that only Grb2 monomers interact with SOS1. PerV likely causes phosphorylation at Y160 on Grb2. If condensation heavily relies on Grb2 dimers for oligomerization, this could explain our perV results. However, it is not clear to what extent Grb2 dimers versus Grb2:SOS drive condensation in T cells. Other studies offer conflicting data that only Grb2 dimers interact with SOS (*149*). Finally, SOS is present in cells at very low copy number (2,000-5,000) (*150*). Therefore, if all the LAT across the cell membrane is completely phosphorylated, there may be insufficient SOS to crosslink LAT into localized condensates. In general, our data suggest that under perV stimulation, T cell signaling either proceeds by a monomeric LAT-based mechanism or bypasses LAT altogether. Understanding precisely how perV is acting on T cells is crucial to accurately interpret experimental work that utilizes this inhibitor in signaling studies.

Polyclonal T cell activation by bispecific antibody on supported lipid membranes

Introduction

T cells possess an unparalleled ability to identify specific pathogenic targets and initiate a global immune response to clear the disease. Many diseases, however, evolve to evade immune surveillance. This is especially poignant for many types of cancer. For instance, tumor cells may accumulate mutations that upregulate the expression of inhibitory ligands, such as PD-L1, which prevent T cells from activating (*151*, *152*). Additional factors, such as the chemical composition of the tumor microenvironment, further complicate adaptive immune response by suppressing T cell function (*153*). There is great interest in the biotechnology and medicinal industries to harness and redirect the specific and potent cytotoxic properties of T cells to targets of interest, such as tumors.

Cancer immunotherapy is a rapidly growing field that aims to use the body's immune system to fight cancer. For example, antibody-based therapies, known as checkpoint inhibitors, block the binding of PD-L1 or other ligands to inhibitory co-receptors and have shown remarkable success clearing various types of cancer (*154*). Chimeric antigen receptor (CAR) T cells are patient-derived T cells expressing an engineered receptor that binds a tumor-associated antigen (*126–129*). CAR T cells have had much success clearing B cell-based lymphoma and leukemia.

Bispecific antibodies (biAb) are another approach to directing T cells to cancer targets. Typical IgG antibodies consist of two identical Fabs (fragment antigen binding) domains joined together by an Fc region. BiAbs are engineering to have two different Fab domains that bind unique epitopes (*101*) (**Figure 4-6A**). Thus, instead of being bivalent for the same epitope, biAbs can simultaneously bind two unique protein targets. Therefore, an immunotherapeutic biAb uses one Fab to bind a TCR constant region, while the other binds a tumor antigen on the surface of a cancer cell. (**Figure 4-6B**). A major advantage of this approach is that biAbs can facilitate anti-tumor activity using any T cell regardless of the TCR clonotype.

Despite numerous clinical successes, many barriers remain for cancer immunotherapy, such as directing T cells against solid tumors and minimizing on-target off-tumor toxicity (*104*, *105*). A more complete understanding of how TCR signaling occurs with various immunotherapeutic approaches is needed to better inform the design and administration of specific and safe treatments. Here, we demonstrate using our supported lipid bilayer platform to study and characterize TCR binding and stimulation by bispecific antibodies at the single molecule level.

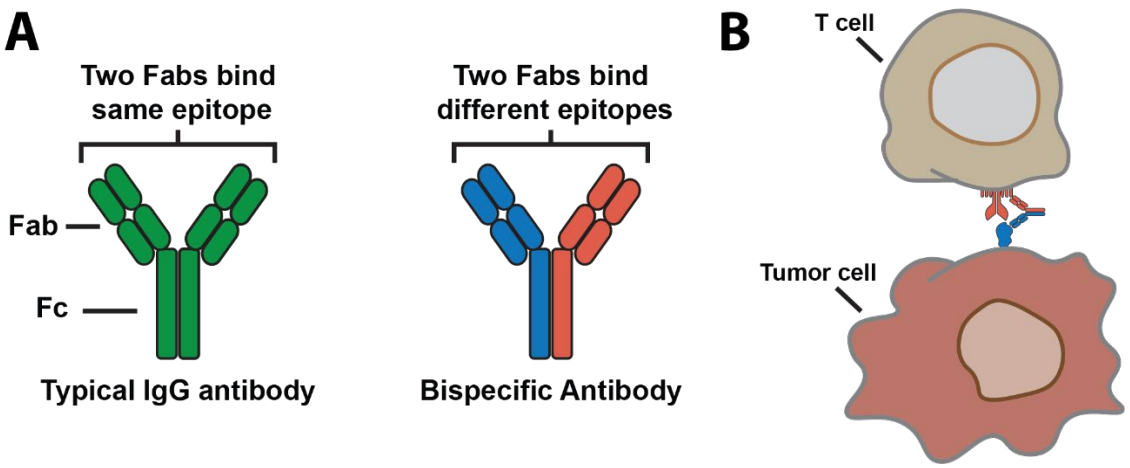

Figure 4-6: Typical IgG antibody vs bispecific antibody architecture.
(A) Comparison of a typical IgG antibody versus a bispecific antibody. A typical IgG antibody (green on the left) contains two Fab portions that are identical and thus bind the exact same epitope. A bispecific antibody (biAb) (orange and blue dual-colored on the right) has a similar architecture except the two Fabs are derived from different antibodies, and thus, each Fab binds a different epitope. Different biAb designs truncate off various non-binding portions, such as the Fc region. (B) Depiction of a biAb crosslinking a TCR on a T cell with a surface tumor antigen on a tumor cell. A cancer immunotherapeutic biAb binds a constant region of a TCR with one Fab, while the other binds a tumor-specific antigen on the surface of a cancer cell. In theory, this results in TCR triggering, leading to cancer cell death.

An important aspect of TCR signaling is the spatial and topographical landscape of the APC (or cancer cell):T cell interface. A prominent hypothesis in TCR signaling, known as the kinetic-segregation model, posits that transmembrane phosphatases possessing large extracellular domains, such as CD45, are spatially excluded from pMHC:TCR complexes (*64*, *155–160*). The extracellular portion of CD45 is rigid and rod-like with an approximate length of 28-50 nm (*159*, *161*, *162*), while the total distance of a pMHC:TCR complex is roughly 15 nm (*160*, *163*, *164*) (**Figure 4-7**). ICAM-1:LFA-1 establishes a distance of about 30 nm (*165*). Thus, when TCR binds pMHC, it forms a local area of “close contact,” which is suspected to sterically exclude CD45 from the pMHC:TCR vicinity. This enables ITAM phosphorylation and further signal propagation. For instance, Choudhuri and colleagues performed experiments in which they activated T cells with pMHC ligands of varying heights (*160*). They observed that increasing the APC:T cell intermembrane spacing, by increasing pMHC ligand height, attenuated IL-2 secretion and enriched CD45 in the cell-cell junction. We investigated biAbs in the context of our supported lipid bilayer platform in order to understand their fundamental signaling properties. In particular, we investigated biAb:TCR binding, activation of polyclonal T cell populations, and whether cellular activation by biAb demonstrated similar intermembrane dimensional dependence.

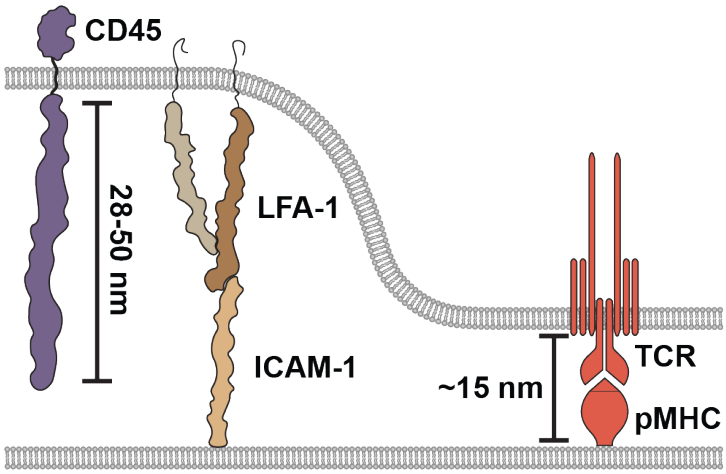

Figure 4-7: Height differences between pMHC:TCR complexes and CD45 ectodomain.
Schematic of the extracellular size differential between various proteins in the APC:T cell interface. The expected intermembrane spacing caused by pMHC:TCR engagement is approximately 15 nm based on the sizes of the TCR and pMHC extracellular domains. Isoforms of CD45 range from 28 to 50 nm. The intermembrane spacing caused by ICAM-1:LFA-1 is approximately 30 nm. Thus, pMHC:TCR binding is suspected to segregation CD45, and other integral membrane PTPs with large ectodomains, away from the TCR to allow phosphorylation and signaling.

Experiment Approach to Tuning Intermembrane Spacing

In collaboration with industrial partners, we developed the following SLB-based method for studying and activating T cells using bispecific antibodies. Supported membranes were functionalized with ICAM-1 and a 10X His-tagged human tumor antigen, B cell maturation agent (BCMA). A biAb was designed with one Fab against BCMA and the other derived from the anti-murine CD3ϵ antibody 145-2C11 and was used to crosslink the TCR to BCMA on the SLB. To modulate intermembrane spacing, stiff non-signaling domains were added to the SLB-proximal end of BCMA to increase its height. BCMA of four different heights were generated, and their sizes were roughly estimated using dynamic light scattering (DLS) (see sizes in **Figure 4-8**). It is important to note that DLS estimates size by assuming particles are spheres. Since BCMA is expected to be rod-like, the reported values underestimate their actual height. Thus, by exposing T cells to biAb-bound BCMA of increasing heights, the intermembrane spacing is expect to likewise increase (**Figure 4-8**).

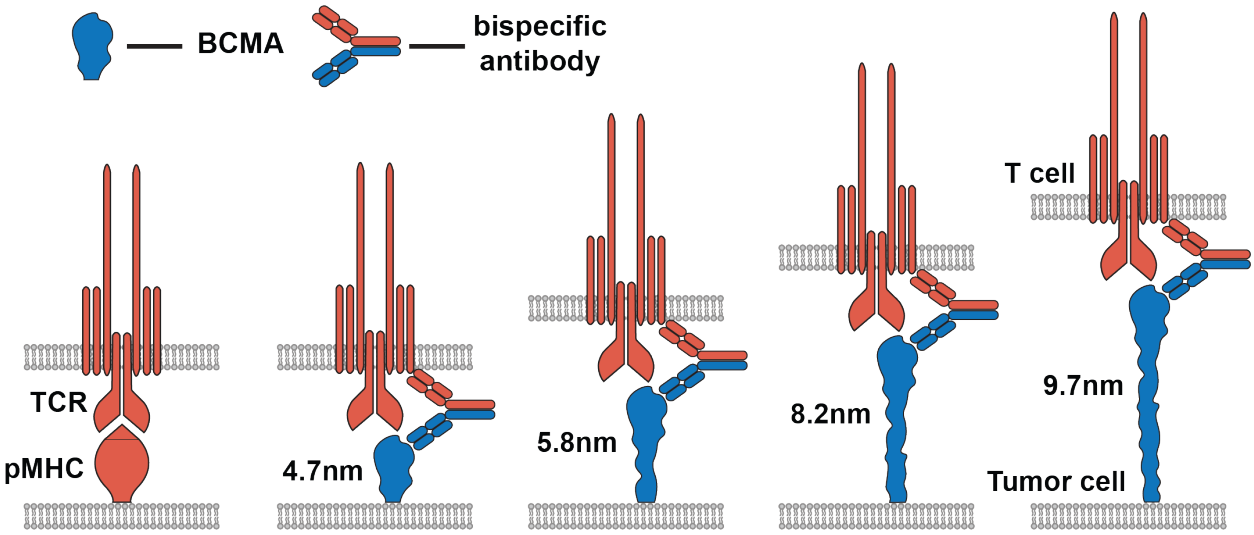

Figure 4-8: Tuning the intermembrane spacing by increasing ligand height.
Schematic of the experimental approach to tune the SLB:T cell intermembrane spacing by increasing the height of the SLB-bound tumor antigen target (BCMA) that binds one Fab of the biAb. The sizes reported in the schematic were measured by DLS.

BiAb Labeling and Characterization

To perform quantitative single molecule experiments, we non-specifically labeled biAb with Atto647N-NHS ester. We ran the labeling reaction at 4°C for 30 min to minimize extensive over-labeling. Upon binding biAb(Atto647) to membrane-conjugated BCMA, we performed TIRF imaging at high power and short exposure (20-50 ms) to image all labeled biAb molecules. Then using particle localization, we extracted single molecule intensities of labeled biAb and fit the distribution to a log-normal. The log-normal fitting of the spot intensity distribution showed the existence of two labeled populations, likely singly and doubly labeled (**Figure 4-9A**). Visual inspection of TIRF images further confirmed two populations of biAb molecules with different brightness (**Figure 4-9B**). This is expected since antibodies possess multiple lysine residues and labeling was performed with NHS ester chemistry. While this presents some challenges, such as being unable to distinguish dimeric states, for the purposed of these experiments, it is sufficient for measuring T cell activation properties by biAb.

Similar to pMHC experiments, BCMA:biAb exhibited lateral Brownian motion as anticipated (**Figure 4-9C**). Upon adding primary murine AND T cells to bilayers containing BCMA-bound biAb, single BCMA:biAb:TCR binding events were detectable with long TIRF exposure (500ms) (**Figure 4-9D**). The off-rate for these binding events was very slow, with an observed average dwell time of 75.6 seconds (**Figure 4-9E**). This value is not corrected for the dye bleaching rate, so the true dwell is even longer. The dwell time of biAb is much longer than the strong agonist MCC-MHC which possesses a 43.6 second observed dwell time (*13*). Such a long dwell time is anticipated since antibodies are known to have exceptionally high affinities (nano- to picomolar range) (*166*). We recently published that anti-TCRβ (H57-597) Fab tethered to supported bilayers by DNA

hybridization possesses an 87 second observed dwell time before bleaching correction (*167*). Therefore, our observed dwell time for 2C11-based biAb is comparable with other Fab-based measurements.

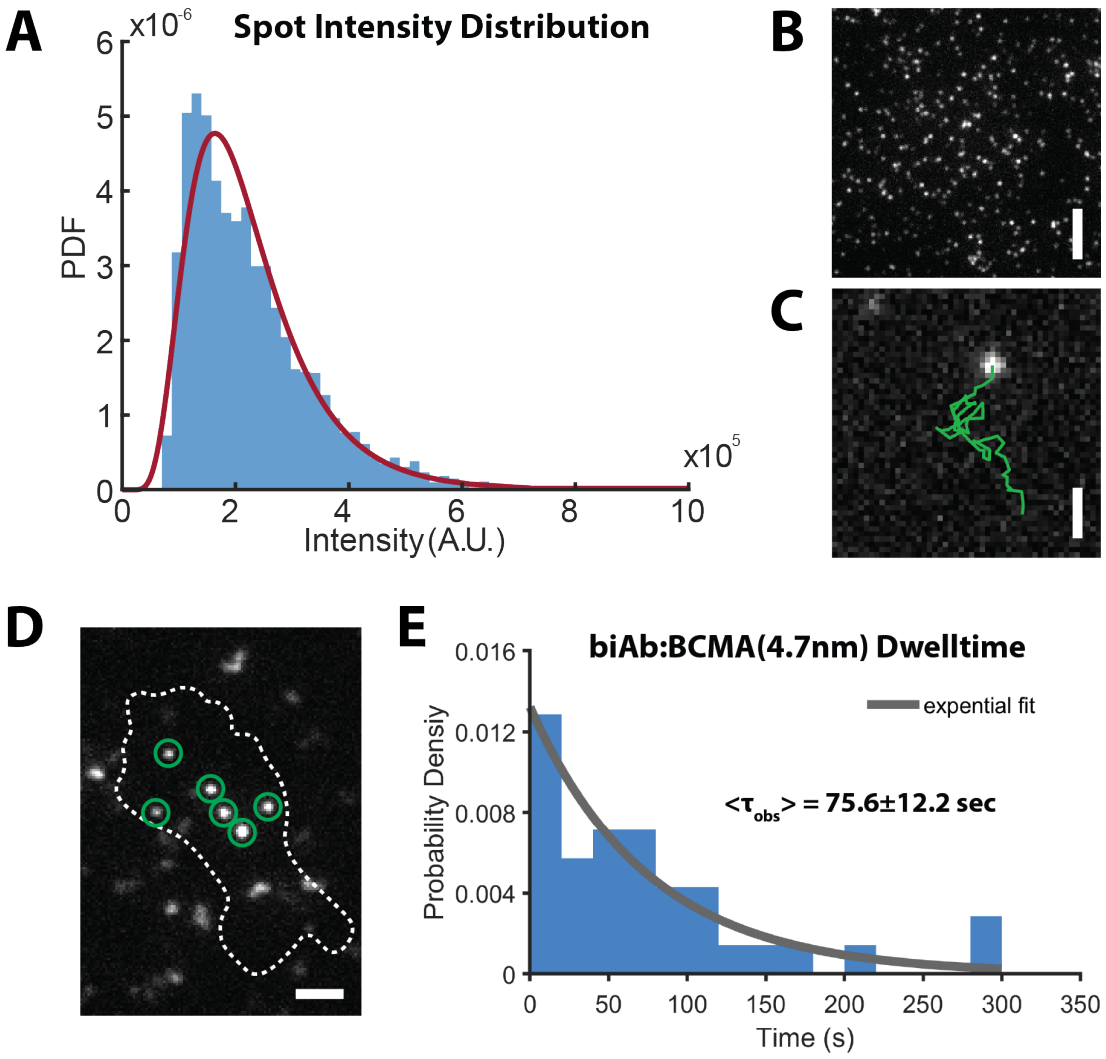

Figure 4-9: Atto647N-labeled biAb characterization.
(A) Single particle intensity distribution suggests two labeled populations of biAb. TIRF images of biAb(Atto647N) taken at high laser power and short exposure (e.g. such as in B) revealed all single biAb molecules. Spot localization was performed to measure individual spots intensity. The distribution of single spot intensities was fit by a lognormal probability density function. Lognormal was used instead of Poisson, as would be expected, due to unavoidable multiplicative errors introduced by the camera. (B) Single molecule TIRF image of biAb(Atto647N) imaged at high laser power and short exposure. There is significant heterogeneity in the number of Atto647N dye molecules per bispecific antibody, as would be expected with labeling via NHS ester chemistry. Bar is 5μm. (C) Single molecule diffusion trace. Single molecule biAb(Atto647N) exhibited random Brownian diffusion in the supported lipid bilayer in the absence of the cell (i.e., not bound to TCR). To observe unbound diffusion, biAb was imaged with TIRF at high laser power, short exposure (50 ms), and rapid imaging rate (20 ms). The green line represents the diffusion trace of the single biAb molecule as obtained by single particle tracking. Bar is 1μm. (D) BiAb effectively binds TCR upon adding T cells to SLB. Using low laser power and long exposure (500 ms) as described in Chapter 2

*(**Figure 2-2**), individual BCMA:biAb:TCR complexes were readily observed (bright spots in green circles). White dashed line is the outline of the cells. Bar is 2μm. (E). BiAb exhibits a long TCR dwell time. Individual binding events (e.g., such as those imaged in D) were tracked in time from the first moment of binding to unbinding. Binding events that crossed each other, started before the first frame of the acquisition, or unbound after the acquisition ended were not included.*

Height Differences Does Not Affect T Cell Activation by BiAb

We next sought to determine how BCMA height affected cellular activation. We measured activation using the fluorescently tagged NFAT translocation sensor described in Chapter 2, except TCRs were ligated and triggered using biAb instead of pMHC (**Figure 4-10A**). In unactivated cells, the NFAT sensor is excluded from the nucleus (**Figure 4-10B**, bottom row). Following TCR-induced calcium flux, NFAT translocates into the nucleus, resulting in an inversion of fluorescence intensity, with higher intensity in the nucleus relative to the cytosol. BiAb bound to SLB-conjugated BCMA successfully activated T cells, as observed by this method (**Figure 4-10B**, top row). We verified that biAb was incapable of activating T cells from solution. T cells that were incubated with medium to high concentrations of biAb and then placed on ICAM-1 only bilayers showed no net increase over biAb-free control (**Figure 4-10C**). Including null peptide T102E-MHC on the supported membrane, which does not activate cells, likewise did not increase activation probability, verifying that biAb has no crossreactivity with MHC (**Figure 4-10C**). In fact, the probability of activation significantly decreased in the presence of T102E-MHC, as has been observed that antagonistic pMHC can inhibit T cell activation (*167*).

To investigate the effects of modulating intermembrane spacing on T cell activation, we performed a series of density titration experiments with each BCMA ligand to assess the activation profile and threshold for each ligand height. After conjugating BCMA, supported membranes were incubated with excess biAb to ensure BCMA saturation. Each BCMA can only bind a single biAb. NFAT translocation was assessed after cells interacted with stimulatory supported bilayers for 30 min. Much to our surprise, biAb activated T cells at roughly equal rates regardless of ligand height (**Figure 4-10D**). The longest ligand appeared to be the most potent, exhibiting the lowest threshold density (i.e., the ligand density resulting in half-maximal population activation). This stands in stark contrast with previous studies, demonstrating that activation strongly depends on intermembrane distance. Also unanticipated, the activation thresholds for all but one BCMA construct were higher than MCC-MHC (~0.5-1.1 molecules/μm^2 verse ~0.2 molecules/μm^2, respectively) despite the fact that biAb dwell time is nearly 30 seconds longer (**Figure 4-9D**). Typically, off-rate is the strongest indicator of signaling potency (*1*–*3*). Perhaps, this inconsistency is due to the absence of CD4 binding.

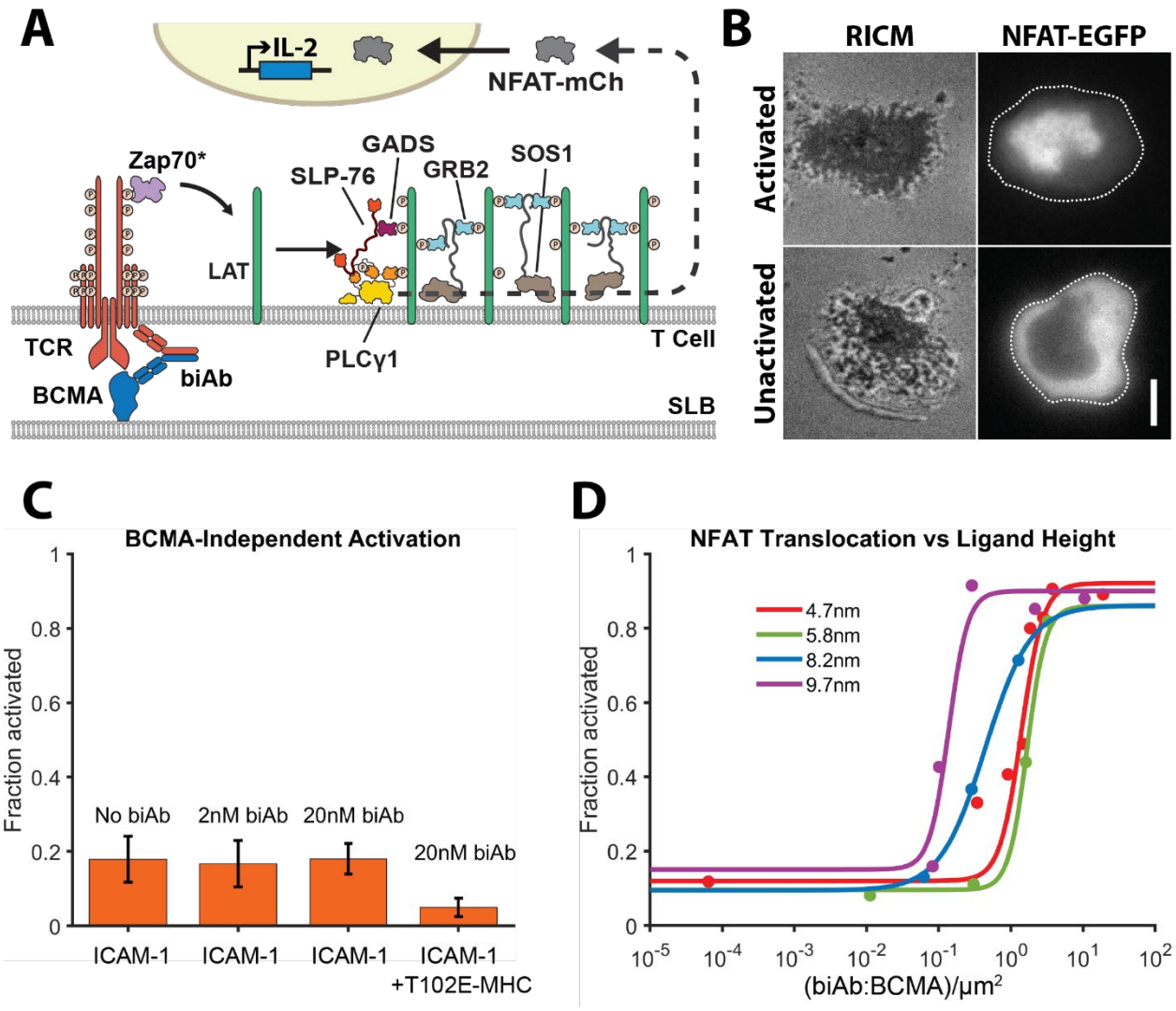

Figure 4-10: Modulating ligand height exhibits no appreciable effect on cellular activation.
*(A) Schematic of T cell activation assay by biAb stimulation using the NFAT translocation sensor described in Chapter 2 (**Figure 2-10**). BiAb triggered TCR by crosslinking a TCR to membrane-tethered BCMA. Whole cell activation was determined by the translocation of NFAT into the nucleus. (B) Representative epifluorescence images of primary murine T cells expressing NFAT-EGFP (right) alongside corresponding RICM images of cell footprint (left). T cells were placed on SLBs containing ICAM-1 and biAb. Epifluorescence images were taken 3μm above the plane of the SLB. (Top) Example of an activated T cell showing more NFAT intensity localized inside the nucleus than the cytosol. (Bottom) Example of an unactivated T cell showing NFAT intensity largely excluded from the nucleus. The white dash lines represent the plasma membrane. Bar is 5μm. (C) BiAb does not activate T cells in solution. T cells were incubated with biAb in solution at different concentrations for ~30 min, after which they were placed on ICAM-1 or ICAM-1 plus null peptide T102E-MHC containing bilayers as indicated. On ICAM-1 only bilayers, ~18% T cells activated. BiAb is solution did not increase the activation rate within the concentration range tested. Error bars represent the standard error of the mean (D) NFAT activation titration curves with BCMA of varying heights. The density of BCMA on SLBs was titrated for each BCMA construct of different heights. After 30 min, the NFAT translocation state was measured. Data points were fitted with a sigmoid curve.*

BiAb Activates T Cells Regardless of TCR Clonal Background

As mentioned, the ability to bind and trigger TCR regardless of clonal background offers immense experimental and medicinal benefit. We recently demonstrated the synthesis and signaling of a universal agonist using an anti-TCR Fab tethered to SLBs through DNA hybridization (*167*). However, to date, this approach has not been tested on a polyclonal T cell population. To test the universality of biAb, we harvested $CD4^+$ T cells from mice with a polyclonal TCR repertoire, transduced them with the NFAT reporter, and placed them on membranes containing biAb bound to BCMA(4.7 nm). The polyclonal T cell population exhibited an identical activation threshold as monoclonal TCR(AND) T cells (**Figure 4-11A**). Therefore, bispecific antibody effectively activates T cells at similar rates regardless of TCR clonotype.

Finally, we tested a bispecific antibody containing a TCR-binding Fab derived from the anti-human CD3ϵ antibody, UCHT1. The other Fab was targeted to human BCMA as before. We labeled the human biAb with Atto647N dye using the same protocol. Upon adding Jurkat T cells to SLBs containing human ICAM-1 and human BCMA:biAb, we observed robust binding between human biAb and Jurkat TCR (**Figure 4-11B**). Human biAb:TCR binding events also induced LAT condensation and PLCγ1 recruitment events (**Figure 3-2**, bottom panel). This further validates that bispecific antibodies can effectively trigger and activate T cells irrespective of TCR clonotype.

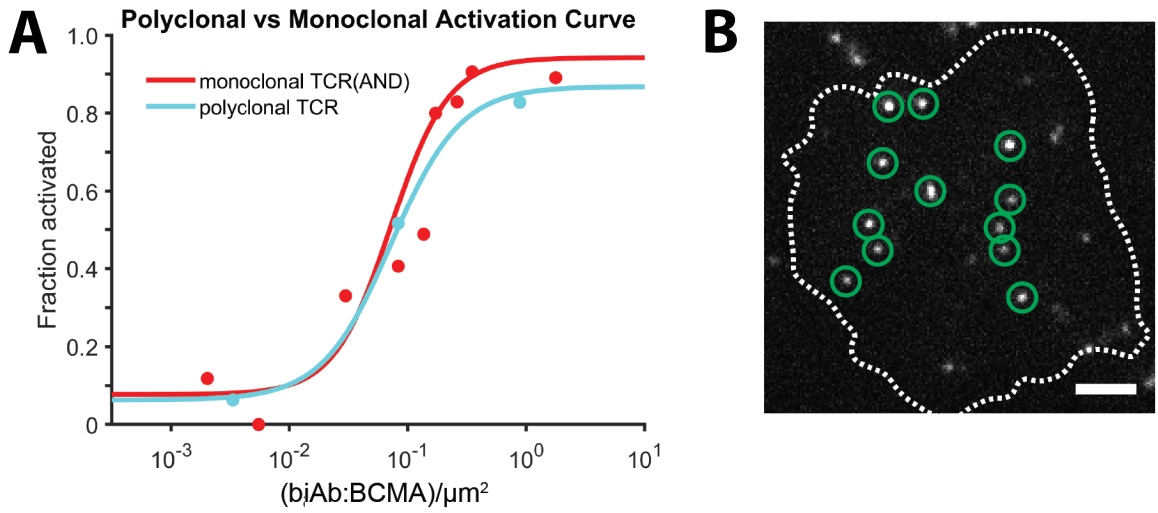

Figure 4-11: Bispecific antibody effectively binds and activates polyclonal T cells.
(A) NFAT translocation titration curve of monoclonal vs. polyclonal TCR T cells. BCMA(4.7 nm) density was titrated on SLBs to which was added primary murine monoclonal AND TCR T cells or polyclonal TCR T cells for 30 min. AND TCR T cells (red data points and sigmoidal fit) and polyclonal TCR T cells (light blue data points and sigmoidal fit) showed near identical NFAT activation rates and threshold density (~0.8-0.9 molecules/μm²). The polyclonal T cells were the $Csk^{AS+/+}$ cells discussed in the next section. (B) TIRF image of BCMA-bound single molecule anti-human CD3ϵ biAb(Atto647N) binding to TCR on a Jurkat cell. TIRF image, taken at 500 ms exposure, showed labeled human biAb molecules binding TCR of the surface of a parental Jurkat T cell. White dashed line is the outline of the cell. Bar is 3μm.

Discussion

There is significant evidence that intermembrane spacing is important for TCR triggering and T cell activation (*155*, *157–160*). Surprisingly, the data presented here seem to suggest that intermembrane spacing dependence is not prevalent at the single TCR level when bound by biAb. A new study recently published from our laboratory using anti-TCR Fabs bound to supported membranes with tethers of varying heights showed that T cell activation does, in fact, have a strong dependence on intermembrane spacing (*168*). The reason for these discrepancies is not fully understood. It is likely that the spacing induced by BCMA:biAb:TCR is not large enough to observe dimensional effects, even with the longest BCMA ligand. The longest BCMA construct is estimated to be 9.7 nm by DLS. Even combined with the predicted size of biAb (15 nm), this is significantly less than the ectodomain of CD45 (28-50 nm). As mentioned above, since DLS approximates particles as spheres, the expected length of BCMA is longer than that measured by DLS. However, it is most likely not long enough to induce phosphatase exclusion from the TCR. Alternatively, it is possible that BCMA does not stand vertical on the supported membrane. Therefore, the intermembrane spacing caused by BCMA requires more precise measurement.

The utility of bispecific antibodies as a cancer therapy has many advantages over traditional treatments. This work highlights their universality to activate polyclonal T cell populations. Additionally, this study demonstrates the wealth of information that the supported lipid bilayer platform offers for investigating tumor immunotherapeutics. We are interested in using this signaling platform to study other types of immunotherapies, such as CAR T cells.

Cortical actin actively accumulates at spontaneous LAT condensates and is depolarized by CD28 triggering

Introduction

T cells are single molecule sensors for agonist pMHC ligand. Maintaining this sensitivity requires fine-tuned balance of opposing signaling forces. The homeostatic distribution of active Lck is critical for properly dialed sensitivity. Lck initiates TCR signaling by phosphorylating ITAMs and subsequently Zap70 (*169*). Lck activity regulation is a function of its phosphorylation state. Phosphorylation at Lck Y505 by the Src-family kinase Csk leads to intramolecular binding to the SH2 domain, resulting in an autoinhibited "closed" conformation. (**Figure 4-12**) (*170*, *171*). Transautophosphorylation of Y394 in the activation loop enables Lck to adopt an active "open" conformation (*172*). Therefore, Csk helps maintain the balance of active versus inactive Lck in the cell. Interestingly, a large fraction of Lck (~40%) is phosphorylated at Y394 and is, therefore, active in resting cells (*173*). How T cells maintain a resting state with a large population of active Lck is not fully understood.

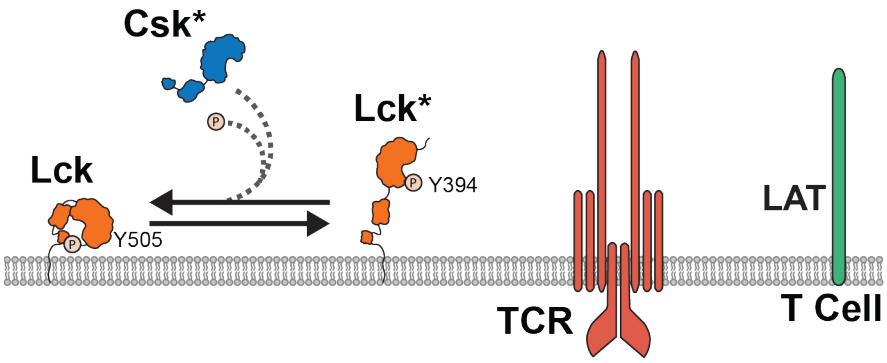

Figure 4-12: Csk regulates active Lck population.
Csk helps maintain the homeostatic activation state of Lck in the plasma membrane. Csk phosphorylates Lck at Y505, which binds intramolecularly to the SH2 domain of Lck, causing a closed, autoinhibited conformation. Y505 is dephosphorylated by CD45. Transautophosphorylation at Y394 releases autoinhibition leading to an active, open conformation. In resting T cells, a large proportion of Lck (~40%) is in a catalytically active phosphorylation state.

To study how perturbing the fraction of active Lck affects TCR signaling, researchers developed a method to selectively inhibit Csk. Mutating the "gatekeeper" residue T266 to the small amino acid glycine allows for specific inhibition of Csk by the bulky small molecule 3-IB-PP1, which is derived from the nonselective kinase inhibitor PP1 (*174*, *175*). Csk(T266G) is referred to as Csk-analog sensitive (Csk^{AS}). Treating $Csk^{AS(+/+)}$ primary T cells with 3-IB-PP1 results in spontaneous phosphorylation of ITAMs, Zap70, and LAT but fails to cause calcium flux (**Figure 4-13**) (*176*). Full cellular activation by 3-IB-PP1 treatment can only be achieved by remodeling the actin cytoskeleton, either

by inhibiting actin polymerization with cytochalasin D (CytoD) or by CD80:CD28 triggering, which activates actin signaling pathways. It was concluding that, in resting T cells, the cortical actin network precludes PLCγ1 from accessing PIP_2 substrate in the membrane. Therefore, actin remodeling loosens the cortical network and allows PLCγ1 to cleave PIP_2. It has long been recognized that actin plays an important role in T cell signaling, activation, and regulation (*177–180*).

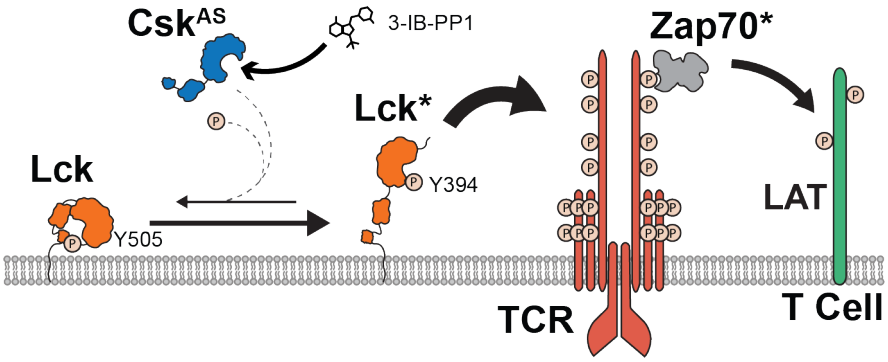

Figure 4-13: Csk^{AS} inhibition causes pMHC-independent LAT phosphorylation but not Ca^{2+} flux. *The Csk mutation T266G enlarges the ATP-binding pocket of Csk, allowing for specific inhibition by the bulky inhibitor 3-IB-PP1. Inhibiting Csk^{AS} presumably increases the proportion of active Lck. 3-IB-PP1 treatment in the absence of TCR ligand causes spontaneous phosphorylation of ITAMs, Zap70, and LAT but fails to propagate to calcium flux. Downstream signaling requires some form of actin reorganization.*

Recapitulating Csk^{AS} Results with Supported Lipid Bilayer System

Given that LAT indirectly recruits actin remodeling proteins such Vav1 (*181*, *182*), we were interested in understanding how LAT condensates influence local actin reorganization, particularly in “orphan” condensates, which are formed in the absences of TCR stimulation. Orphan condensates may require regulation against spurious signaling. We utilized Csk$^{AS(+/+)}$ transgenic mice expressing the F-actin sensor Lifeact-mCh to allow us to image local cortical actin polymerization by TIRF (*183*). First, we tested the Csk^{AS} system on our SLB signaling platform. Since Csk^{AS} transgenic mice express polyclonal TCR, we took advantage of the bispecific antibody method described in the previous section. Titrating BCMA:biAb density, we determined the threshold density for Csk$^{AS(+/+)}$ T cells using the NFAT translocation reporter. The threshold density of BCMA:biAb was identical to TCR(AND) T cells (~1 molecule/μm^2) (**Figure 4-11A**). We then stimulated cells on supported membranes containing threshold BCMA:biAb density and measured the dose-response of 3-IB-PP1 (**Figure 4-14A**). Treating cells with 10μM 3-IB-PP1 increased the NFAT activation rate by thirty percentage points, indicating successful Csk^{AS} inhibition. Next, we used CytoD or CD80 to promote actin reorganization. In the absence of TCR stimulation, actin remodeling plus 10μM 3-IB-PP1 significantly increased the proportion of activated cells (**Figure 4-14B**). NFAT translocation probability also increased, though much lower in magnitude, in 3-IB-PP1 treated cells on ICAM-1 only containing SLBs. This is likely due to LFA-1 triggering lower levels of actin stimulation. Taken together, these results confirm the conclusion that actin protects cells from spontaneous activation (*176*).

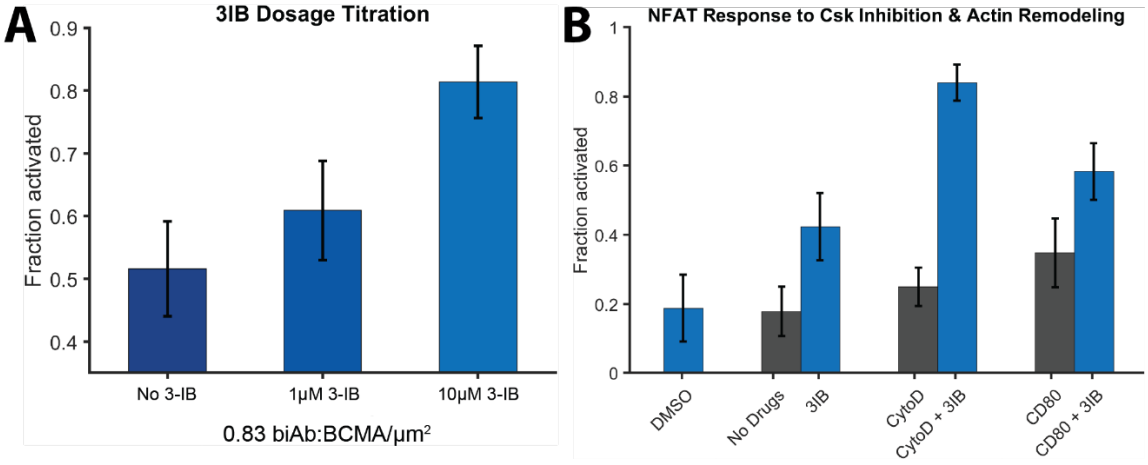

Figure 4-14: T cells require actin remodeling for activation by 3-IB-PP1.
(A) TCR-induced T cell activation rate increases with 3-IB-PP1 dosage. Primary murine Csk$^{AS(+/+)}$ T cells were added to SLBs containing threshold density of BCMA:biAb, which causes ~50% of cells to translocate NFAT into the nucleus. Titrating the dosage of 3-IB-PP1 monotonically increases the probability of cellular activation. (B) 3-IB-PP1 plus actin remodeling robustly activated T cells. Primary murine Csk$^{AS(+/+)}$ T cells were added to SLBs containing only ICAM-1 and were treated either with or without 10μM 3-IB-PP1 and actin-modulating agents (i.e., CytoD and CD80). Treating with 3-IB-PP1 plus actin remodeling resulted in a significant increase in NFAT activation frequency. All bars represent the standard error of the mean (SE).

Actin Locally Accumulates at Spontaneous LAT Condensates and is Attenuated by CD28 Stimulation

To test the hypothesis that actin blocks PLCγ1 assess to PIP_2, we imaged local actin activity relative to LAT condensation. Csk$^{AS(+/+)}$/Lifeact-mCh primary T cells transduced with LAT-EGFP were placed on supported bilayers containing only ICAM-1 and imaged with TIRF microscopy to specifically visualize cortical actin. Filamentous structures of actin were not observable in these conditions; however, dynamic accumulations (or “clouds”) of actin were visible proximal to LAT condensates, as seen in the TIRF images and intensity line profiles in **Figure 4-15A**. Actin clouds began very diffuse at the beginning of the LAT condensate lifetime and gradually concentrated around the condensate over time (**Figure 4-15C**). We then added these cells to bilayers containing ICAM-1 and CD80. CD80 binds to CD28 in the T cell membrane and is known to reenforce TCR-signaling as well as activate Vav1, leading to actin cytoskeleton reorganization (*184*, *185*). Interestingly, stimulating CD28 resulted in the loss of the local actin polarization around LAT condensates (**Figure 4-15B** and **D**). These data are consistent with the hypothesis that actin occludes membrane access from PLCγ1 unless further cytoskeletal remodeling occurs, such as through CD80:CD28 stimulation. Our results reveal that instead of a uniform cortical actin network blocking membrane entry, actin appears to actively accumulate specifically at sites of non-TCR-induced LAT condensation. Further signaling input from CD28 (and possibly pMHC:TCR) depolarizes actin accumulation around to LAT condensates to allow signal propagation (**Figure 4-14B**).

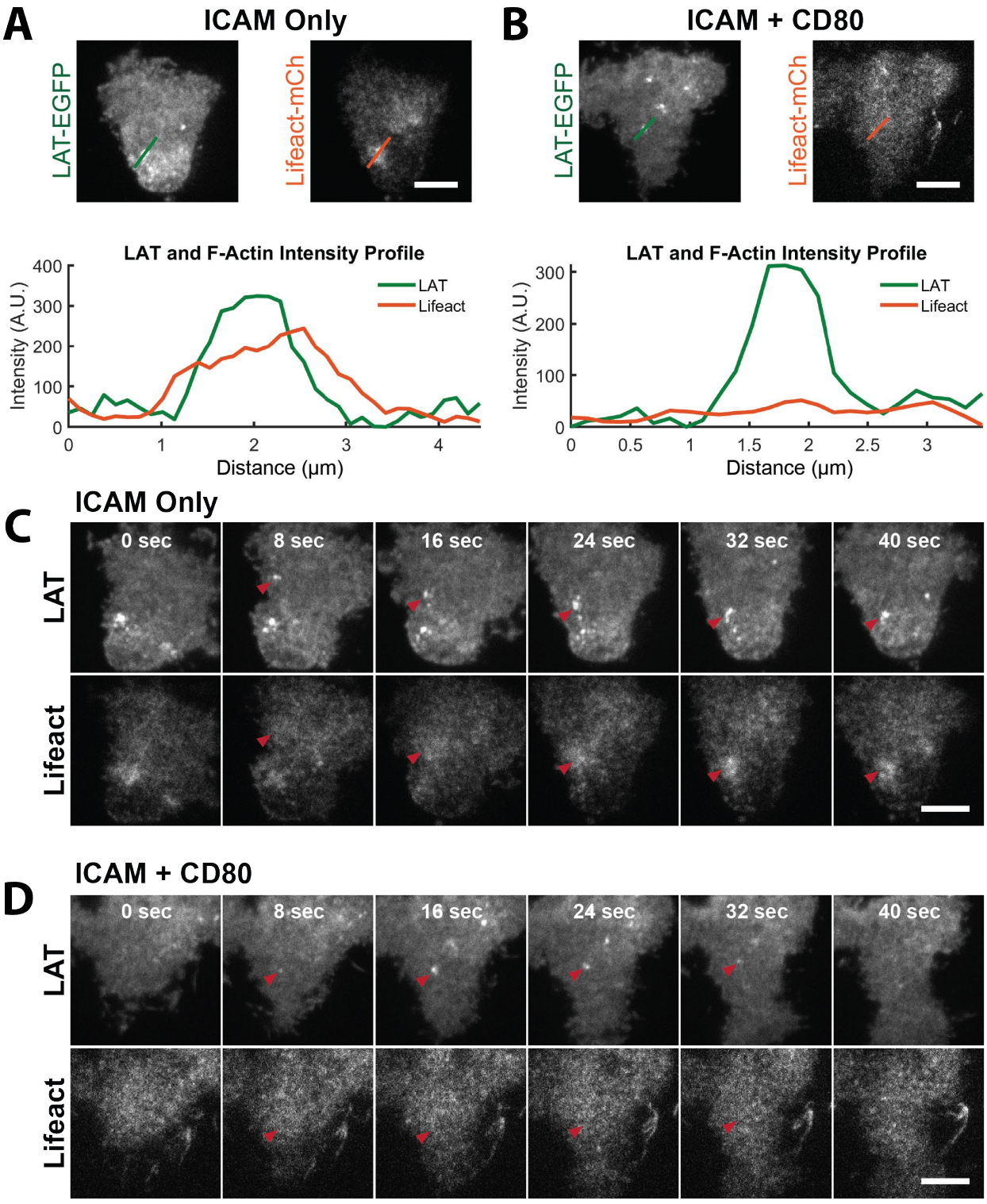

Figure 4-15: Actin accumulation at non-TCR induced LAT condensates is mitigated by CD28. *(A) Actin accumulates around non-TCR-induced LAT condensates. Primary murine T cells co-expressing Lifeact-mCh and LAT-EGFP were placed on supported membranes containing only ICAM-1 and imaged with TIRF. (Top) Representative TIRF images of LAT (left) and Lifeact (right). (Bottom) Intensity line scan plots show the pixel intensity along the green and orange lines in the top TIRF images for LAT-EGFP (green plot) and Lifeact-mCh (orange plot). (B) Actin fails to accumulate around non-TCR-induced LAT*

condensates with CD28 stimulation. Primary murine T cells co-expressing Lifeact-mCh and LAT-EGFP were placed on SLBs containing ICAM-1 and CD80 and imaged with TIRF. (Top) Representative TIRF images of LAT (left) and Lifeact (right). (Bottom) Intensity line scan plots show the pixel intensity along the green and orange lines in the top TIRF images for LAT-EGFP (green plot) and Lifeact-mCh (orange plot). (C) TIRF image time series of a T cell expressing LAT-EGFP (top) and Lifeact-mCh (bottom) on an SLB containing only ICAM-1. (D) TIRF image time series of a T cell expressing LAT-EGFP (top) and Lifeact-mCh (bottom) on an SLB containing ICAM-1 and CD80. Bars for all TIRF images are 5μm. The primary murine T cells used in these experiments were $Csk^{AS(+/+)}$, though 3-IB-PP1 was not used.

Discussion

Avoiding spurious T cell activation in the absence of antigen is critical for proper adaptive immune function. T cells that trigger on self-antigen cause a range of autoimmune diseases (*186*). To minimize this, T cell signaling has evolved to become extremely precise by including various regulatory mechanisms that attenuate or altogether block TCR signaling. These include inhibitory co-receptors (e.g., PD-1 and CLTA-4), regulatory T cells, and kinases-phosphatase balance.

The actin cytoskeleton plays a vital role in facilitating cellular mobility, T cell interrogation of APCs for agonist pMHC, mechanical force generation, and regulation of T cell activation (*177–180*). LAT clusters are known to recruit various actin modifying proteins such as Nck, WASP, and Vav1 (*181*, *182*, *187*, *188*). CD28 signaling is also known to augment TCR signaling and activate actin machinery (*184*, *185*). In fact, the intracellular signaling domains of CD28 are included in many CAR T cell designs (*127–129*). Phenotypically, T cells on SLBs containing CD80 and ICAM-1 spread and crawl more robustly and quickly compared to ICAM-1 only containing bilayers. Our data suggest that one way CD28 enhances TCR signaling is by redistributing actin away from LAT condensates (**Figure 4-16**). Since CD80 is present at higher densities, it likely provides a more uniform actin stimulating force across the SLB:T cell interface, thus inducing a global instead of localized remodeling force. We observed that T cells on ICAM-1 and CD80-containing SLBs exhibited a higher basal activation rate (without 3-IB-PP1 treatment) compared to ICAM-1 only bilayers (**Figure 4-14B**). This is likely due to spurious LAT clusters successfully signaling, thanks to the actin remodeling provided by CD80:CD28. Additionally, the fact of CD28 attenuates condensate-proximal actin polarization suggests potential compositional differences between LAT condensates formed in the presence versus absence of CD28 triggering. In future experiments, we plan to test how single molecule TCR stimulation affects local actin activity, particularly at TCR-induced LAT condensates with and without CD28 activation. Additionally, we aim to investigate how inhibitory co-receptors such as CTLA-4, which also binds CD80, and PD-1 act on local cortical actin and proximal TCR signaling.

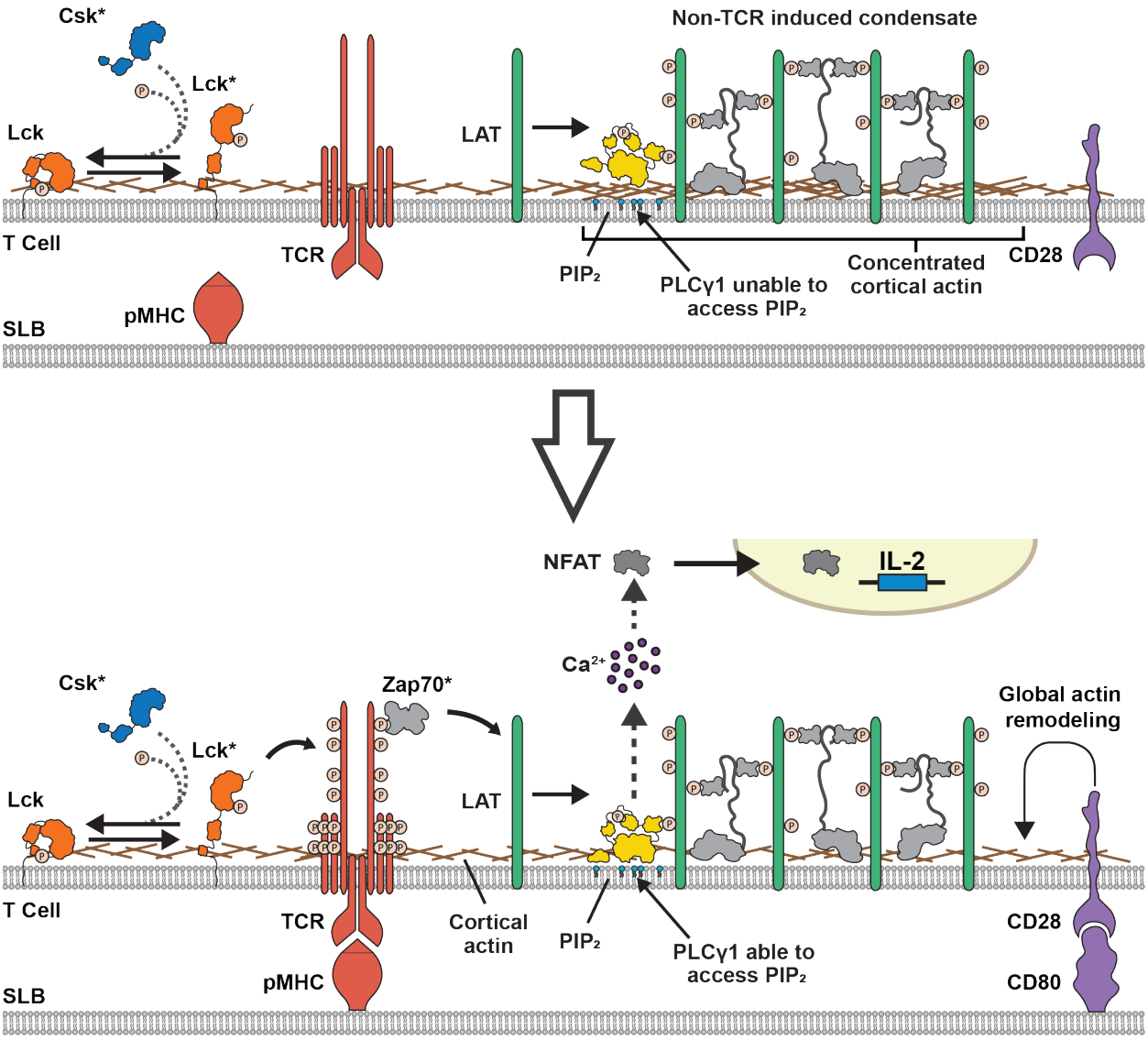

Figure 4-16: Model for actin-mediated regulation of non-TCR-Induced LAT condensates.
(Top) In the absence of TCR stimulation, occasional rare LAT condensates form spontaneously or as a result of ICAM-1:LFA-1 triggering. To prevent these spurious condensates from activating T cells, cortical actin cytoskeleton actively accumulates at sites of LAT condensation to block PLCγ1 from gaining access to PIP_2. (Bottom) Actin remodeling provided by CD28 signaling (or possibly TCR ligation) causes cortical actin to redistribute more uniformly across the plasma membrane regardless of LAT condensation. This effective dilution of actin proximal to LAT condensates allows PLCγ1 to engage and cleave PIP_2 resulting in downstream signaling and cellular activation.

5 | Methods and Analyses

Methods

T cell Culture and Transduction

The mice used in this study were the cross of (B10.Cg-Tg(TcrAND)53Hed/J) x(B10.BR-H2k2 H2-T18a/SgSnJ) from Jackson Laboratory. All animal work was performed with prior approval by the IACUC committee, Lawrence Berkeley National Laboratory Animal Welfare and Research Committee, under the approved protocol 17703. Lymph nodes and spleens of 6- to 20-week-old mice were stimulated with 1μM MCC peptide in vitro. Both male and female mice were used within this study and were monitored for clean health prior to organ harvest. Activated T cells were retrovirally transduced using Platinum-Eco cell–derived supernatants. Platinum-Eco cells (Cell Biolabs, San Diego, CA) were transfected with the desired plasmid using linear, polycationic polyethylenimine (Sigma-Aldrich). After 48 hours, retrovirus-containing supernatant was used to spinfect T cells in the presence of polybrene (4 mg/ml) on day 3 after activation. Typical transduction efficiencies ranged from 10-30%. The entire population was used for imaging experiments; 0.5 million to 2 million cells were deposited onto each bilayer. Positive fluorescent cells were easily distinguished from negative cells. Overall phenotypic behavior of crawling and spreading were comparable between the two populations using RICM to ensure transduction of the various constructs did not alter basic T cell behavior.

Protein Purification

Histidine-tagged MHC class II I-E^K and ICAM-1 were expressed and purified as previously described (*75*). MHC II with C-terminal hexahistidine tags on both α and β chains were expressed using a baculovirus expression system in S2 cells and purified using a Ni–nitrilotriacetic acid (NTA) agarose column (Qiagen). The histidine-tagged MHC bacmid (*189*) was a gift of L. Teyton (Scripps Research Institute) and M. Davis (Stanford University). The bacmid for ICAM-1 with a C-terminal decahistidine was synthesized, and it was similarly expressed and purified in High Five cells (Invitrogen) (*75*).

DNA Constructs

The murine stem cell virus (MSCV) backbone was used (similar to AddGene #91975) for retroviral transduction of primary murine T cells. Plasmids were constructed using Gibson Assembly (*190*) and cloned using XL-1 BLUE (Fischer Scientific) E. coli.

MSCV-NFAT-EGFP was constructed from a plasmid containing a GFP fusion to the regulatory domain of the murine NFAT1 (NFATc2) protein in a murine stem cell virus vector (*92*) and was a gift of F. Marangoni (Harvard Medical School). This truncated form of NFAT1 [pMSCV-NFAT1(1–460)-GFP] contains the regulatory domain that controls the nucleocytoplasmic shuttling of NFAT but lacks the DNA binding domain. A second version of the plasmid was generated to replace the GFP coding sequence with mCherry.

MSCV-mNG-GRB2 was constructed from a plasmid containing human GRB2 that was a gift from Neal Shah (*50*). An mNeonGreen license and plasmid stock was purchased from Allele Biotechnology.

MSCV-LAT-EGFP was constructed from a plasmid containing cDNA for Mus Musculus Linker for Activation of T cells (NM_010689.3).

MSCV-LAT-EGFP-P2A-mSci-GRB2 was cloned from the constructs above with the addition of the P2A sequence that was ordered as an oligonucleotide from Elim Biopharmaceuticals, Hayward, CA.

MSCV-NFAT-mCh-P2A-LAT-EGFP was cloned from the constructs above with the addition of the P2A sequence that was ordered as an oligonucleotide from Elim Biopharmaceuticals, Hayward, CA.

MSCV-PLCγ1-mNG/HaloTag was constructed from mouse PLCγ1 cDNA obtained from Horizon Discovery (Catalog#: MMM1013-202859869) (Accession: BC057161) and cloned into the MSCV vector with mNG. HaloTag was obtained as a gift from the Orion Weiner Lab. TMR fluorophore for HaloTag was obtained from Promega (G8251).

MSCV-PLCγ1(Y775/783F)-mNG (i.e., PLCγ1(Y2F)-mNG) was made from the wild type construct above using the Q5 Site-Directed Mutagenesis Kit from New England

BioLabs (Catalog#: E0554S). Primers were purchased from Elim Biopharmaceuticals, Hayward, CA.

All PLCγ1-based truncation constructs (SHarray, SHarrayΔSH3, SHarrayΔcSH2, nSH2, and PLCγ1ΔSH3) were cloned from the original MSCV-PLCγ1-mNG using Gibson Assembly or Q5 Site-Directed Mutagenesis.

MSCV-LAT-EGFP-PA2-nSH2-mSci was cloned from the constructs above with the addition of the P2A sequence that was ordered as an oligonucleotide from Elim Biopharmaceuticals, Hayward, CA.

MSCV-tdSH2(PG)-mNG was obtain by assembling the nSH2 sequence from MSCV-PLCγ1-mNG and the SH2 sequence from MSCV-mNG-GRB2. The linker sequence between the SH2 sequences is the native linker between nSH2 and cSH2 from mouse PLCγ1.

MSCV-tdSH2(GG)-mNG was obtain by assembling two copies of the SH2 sequence from MSCV-mNG-GRB2 in tandem. The linker sequence between the SH2 sequences is the native linker between nSH2 and cSH2 from mouse PLCγ1, identical to MSCV-tdSH2(PG)-mNG.

LAT-mSci-P2A-mNG-VAMP7 was constructed from LAT and mouse VAMP7 cDNA obtained from Horizon Discovery (Catalog#: MMM4769-202763053) and cloned into the MSCV vector.

LAT-mSci-P2A-SKAP1-mSci was constructed from LAT and mouse SKAP1 cDNA obtained from Transomic Technologies (Catalog#: TCM1004) (Accession: BC171961) and cloned into the MSCV vector.

Peptide Synthesis and Labelling

Moth cytochrome C 88–103 peptide (MCC88–103; abbreviated as MCC) and previously characterized variants (*191*) were synthesized and lyophilized on campus (D. King, Howard Hughes Medical Institute Mass Spectrometry Laboratory at University of California, Berkeley) or commercially (Elim Biopharmaceuticals, Hayward, CA). A short flexible linker of three amino acids and terminal cysteine was added to the C terminus for fluorophore labeling. The sequences are as follows: MCC (ANERADLIAYLKQATK), MCC(C) (ANERADLIAYLKQATKGGSC), T102S (ANERADLIAYLKQASK), T102S(C) (ANERADLIAYLKQASKGGSC), and T102E (ANERAELIAYLTQAAEK). For dye conjugation, the cysteine-containing peptide sequences were reacted with the maleimide-containing organic fluorophore of interest (Atto647N, Atto565, or Atto488; Atto-Tec GmbH, Siegen, Germany) in phosphate-buffered saline (PBS) with a trace amount of 1-propanol. The labeled peptides were purified using a H_2O/acetonitrile gradient on a C18 reverse-phase column (Grace Vydac, Deerfield, IL) in the AKTA Explorer 100 FPLC

system (Amersham Pharmacia Biotech, Piscataway, NJ). Mass spectrometry was used to confirm the peptide identity after purification.

Bilayer Preparation

Glass-supported lipid bilayer membranes were prepared in imaging chambers and functionalized with proteins in a manner similar to prior experiments (Lin et al., 2009; O'Donoghue et al., 2013)(*12*, *13*). At 18 to 24 hours before imaging, MCC and variant peptides were loaded onto MHC II I-E^K at $37°C$ in peptide-loading buffer [PLB - 1% (w/v) bovine serum albumin (BSA) in PBS (pH 4.5) with citric acid]. Just before exposure to bilayers, dye-peptide-MHC complexes in PLB were purified using a 10,000–molecular weight cutoff spin concentrator (Vivaspin 500, GE Healthcare, Pittsburgh, PA) and 1x TBS wash [TBS; 19.98 mM tris and 136 mM NaCl (pH 7.4); Mediatech Inc., Herndon, VA], and resuspended to 300 uL. Small unilamellar vesicles (SUVs) are formed using tip sonication with the composition of 98 mole percent (mol %) 1,2-dioleoyl-snglycero-3-phosphocholine and 2 mol % 1,2 dioleoyl-sn-glycero-3-[(N(5-amino-1-carboxypentyl) iminodiacetic acid) succinyl] (nickel salt) (Ni2+-NTA-DOGS) (Avanti Polar Lipids, Alabaster, AL) in Milli-Q water (EMD Millipore, Billerica, MA). In addition, #1.5 25-mm-diameter round coverslips (Thomas Scientific #1217N82) were ultrasonicated in 1:1 isoporopyl/H_2O or 2% Hellmanex solution and then etched for 5 min in piranha solution (3:1 H_2SO_4/H_2O_2). 35-mm AttoFluor chambers (Fischer Scientific #A7816) were used to house the etched coverslips. A 1:1 mixture of SUVs and 1x TBS was introduced into the chambers, and bilayers were allowed to form through vesicle rupture for at least 30 min. After rinsing, the bilayer was activated with 100 mM $NiCl_2$ for 5 min. Samples were exchanged to a live T cell imaging buffer [LCB - 1 mM $CaCl_2$, 2 mM $MgCl_2$, 20 mM Hepes, 137 mM NaCl, 5 mM KCl, 0.7 mM Na_2HPO_4, 6 mM D-glucose, and 0.1% (w/v) BSA] and incubated for 30 min to allow BSA blocking of bilayer defects. Immediately before imaging, the bilayer was incubated for 25 min with His-ICAM-1 (≈ 10 nM) and His-pMHC (≈ 10 pM) or His-BCMA ($\approx 0.001 - 100$ nM) in LCB. The bilayer was rinsed with imaging buffer after the incubation, and the His-tagged/Ni-NTA– bound proteins were allowed to equilibrate on the bilayer for 20 min. For bilayers containing BCMA, bilayers were incubated with 3X molar excess (relative to BCMA incubation concentration) of bispecific antibody followed by rinsing with imaging buffer. The resulting supported membranes typically display ICAM-1 at 100 to 200 μm^{-2}, pMHC at 0.1 to 2 μm^{-2}, and BCMA:biAb at 0.01-10 μm^{-2}. The chamber was equilibrated to $37°C$, and T cells resuspended in T cell imaging buffer were introduced. All imaging was done in $37°C$.

Imaging

All imaging experiments were performed on a motorized inverted microscope (Nikon Eclipse Ti-E; Technical Instruments, Burlingame, CA) with a motorized Epi/TIRF illuminator, a motorized Intensilight mercury lamp (Nikon C-HGFIE), and a motorized stage (MS-2000; Applied Scientific Instrumentation, Eugene, OR). A laser launch with 488-, 560-, and 640-nm diode lasers (Coherent OBIS, Santa Clara, CA) was aligned into

a custom-built fiber launch (Solamere Technology Group Inc., Salt Lake City, UT). For TIRF imaging, laser illumination was reflected through the appropriate dichroic beam splitter (ZT488/ 647rpc, Z561rdc with ET575LP) to the objective lens [Nikon (1.47, numerical aperture; 100×), TIRF; Technical Instruments, Burlingame, CA]. RICM and epifluorescent excitation were filtered through a 50/50 beam splitter or band-pass filters (D546/10×, ET470/40×, ET545/30×, and ET620/60×). All emissions were collected through the appropriate emission filters (ET525/50M, ET600/50M, and ET700/75M) and captured on an EM-CCD (iXon 897DU; Andor Inc., South Windsor, CT). All filters were from Chroma Technology Corp. (Bellows Falls, VT). All microscope hardware was controlled using μManager (*192*).

Single-molecule TIRF images are taken at the same power dosage, either by high laser illumination intensity ($8\ \mathrm{mW\ cm^{-2}}$) and short exposure time (20 ms) or by low laser illumination intensity ($0.2\ \mathrm{mW\ cm^{-2}}$) and long exposure time (500 ms). Single-molecule TIRF images of long exposure time (500 ms) were collected every 2 to 4 s to localize single pMHC-TCR using a laser illumination intensity of $0.2\ \mathrm{mW\ cm^{-2}}$. Fluorescent protein tagged constructs (e.g., LAT-EGFP, PLCγ1-derived constructs, VAMP7-mNG, SKAP1-mNG, mNG-Grb2, etc.) were monitored at $0.2\ \mathrm{mW\ cm^{-2}}$ every 2 to 4 s. When cells were imaged to measure LAT condensation only, the cells were imaged as they landed, or within 5 minutes of landing, for a duration of 300 seconds. Cells imaged for NFAT-mCherry/EGFP was done by epifluorescence using 150-ms exposure time every 10-50 sec at 3 and 6 μm above the coverslip to monitor NFAT dynamics. NFAT monitoring continued for 30 minutes for live acquisition. For endpoint population statistics, T cells interacted with supported membranes for ~30 min before NFAT translocation was assessed.

Single Particle Tracking

A combination of the standard TrackMate plugin (*193*) for ImageJ and a custom in-house TrackMate plugin was used. The custom plugin was specifically developed to account for the centripetal motion observed by pMHC:TCR binding events. Despite the improved accuracy, each binding event still required manual inspection, using TrackMate's built-in track inspection tools, to eliminate occasional tracking / detection artifacts. Single-molecule trajectories were verified using single-step unbinding determined by a Bayesian change point detection algorithm (*194*).

A binding event trajectory and dwell time was considered valid if it had no branching (i.e. no splits or merges) and began and end with the of the acquisition. Delay time was considered valid if its associated pMHC binding event did not have any branching (i.e. no splits or merges).

Antibody Coating on Glass Coverslips

Glass coverslips were first clean by 30-45 minutes of sonication in 2% Hellmanex III (Fisher Scientific, Catalog#: 14-385-864) solution at 40°C. Etching in piranha solution for 5 minutes can increase protein adsorption but is not necessary. After thorough washing with MilliQ water, the clean coverslips were incubated for 5 min in a 1:100 PBS dilution of fibronectin stock solution (Sigma-Aldrich, Catalog#: F1141-2MG). After thorough washing with PBS, coverslips were incubated with anti-TCRβ antibody (H57-597) (BioLegend, Catalog#: 109217) at 100μg/μL for 30 min followed by washing with PBS. Before adding cells and imaging, the buffer was exchanged to live cell imaging buffer.

EGTA Treatment.

Prior to imaging, T cells were incubated in calcium-free imaging buffer containing 1mM EGTA for 20 min. Cells were then washed three times with calcium-free imaging buffer to remove EGTA and then added to imaging chambers containing calcium-free imaging buffer. Failure to adequately remove EGTA results in gradual desorption of His-ICAM-1 and His-pMHC from Ni-chelating lipids.

PP2 and GGTI Treatment

T cells were incubated with either PP2 or GGTI for 30-45 min prior to being added to imaging chambers. Imaging chambers were filled with imaging buffer plus the respective pharmaceutical agent at the same concentration the cells were incubated with. GGTI was added to chamber solutions immediately prior to addition of cells since GGTI caused blebbing of the supported bilayer (**Figure 4-4B**).

Pervanadate Preparation

Sodium orthovanadate was mixed with H_2O_2 to yield a final concentration of 1mM orthovanadate in 3% H_2O_2. The reaction was incubated for 15 min at room temperature, then quenched by the addition of catalase (200μg/mL final catalase concentration). Note that addition of catalase causes rapid release of gaseous oxygen (O_2). Therefore, the reaction should take place in a sufficiently large container. Cells were then incubated with pervanadate prior to imaging, or pervanadate was added partway through an imaging acquisition to observe its effects more directly.

PLCγ1 Knock-down in Jurkats

Pre-cloned shRNA construct targeted against human PLCγ1 (Sigma-Aldrich, (shRNA MISSION®, TRCN0000218478) was introduced into Jurkats using lentivirus

retroviral transduction and confirmed by western blot using an anti-human PLCγ1 antibody (See **Figure 5-1**).

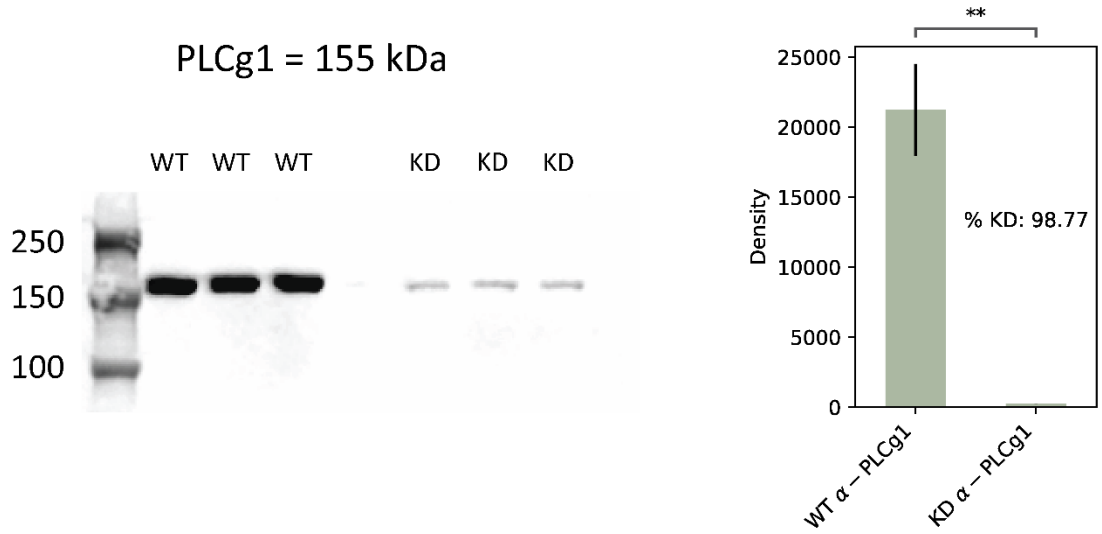

Figure 5-1: Western blot of PLCγ1 abundance in J.P1 (PLCγ1-knock Down) Jurkats.

Quantification and Statistical Analysis

Statistics

Data expressed as $x \pm y$ (SD) represents a mean (μ) of x and standard deviation of y. While (SE) refers to y as the standard error of the mean. The meaning of the sample size, *n*, is specified in relevant figure legends. Quantification and statistical analysis were done using Matlab as well as Python with the following libraries – scikit-image, scipy, pandas, and numpy.

The SE for binary data sets, such NFAT translocation experiments and TCR productivity (**Figure 2-7**, bottom), was calculated using Bernoulli standard deviation. The equation for standard error is (p is the probability of success):

$$SE = (p(1-p)/n)^{1/2}$$

Dwell Times

Reported pMHC:TCR dwell times, $\langle \tau_{\mathrm{dwell}} \rangle = \frac{1}{k_{\mathrm{off}}}$, were corrected for photobleaching by measuring the bleach rate of fluorescent pMHC on supported

membranes, k_{bleach}, and fitting the observed dwell time distribution, $f_{obs}(t)$, to the following equation:

$$f_{obs}(t) = (k_{\mathrm{bleach}} + k_{\mathrm{off}})e^{-(k_{\mathrm{bleach}}+k_{\mathrm{off}})t}$$

FRAP of LAT condensates

Many studies of protein condensation phase transitions use FRAP as a technique to estimate the fluidity of the system (*42*, *65*). A feature of LAT condensates in living cells that complicates this measurement is that the condensates have definite growth and decay phases as well as centripetal motion towards the center of the cell. However, by intermittently imaging the cell at a fast frame rate (20 ms) and higher laser power followed by multiple seconds to allow recovery, we were able to see significant recovery in the LAT condensates regardless of whether the condensate was actively growing or decaying (**Figure 2-4**).

NFAT Translocation

NFAT translocation was determined by measuring the fluorescence intensity in the cytosol and nucleus. All images with the masked regions were inspected. The time point at which the mean nuclear NFAT intensity is first detected to be above the mean cytosolic intensity was set as the time point of initial NFAT translocation.

TCR Productivity Input-Response Function and LAT Delay Times

Productive binding events are those that meet the criteria of isolation (> 1 μm from all other binding events) and produce local (< 300 nm) LAT condensation. Single pMHC:TCR dwell times of all complete binding events were partitioned into temporal bins. From each bin, we extracted the number of pMHC:TCR events that were productive and divided the number of productive events by the total number of events in each respective bin to give the probability of producing a LAT condensation in that bin time interval. The probability values for each bin were plotted and fitted to give the single pMHC:TCR productivity input-response function. This was done for both MCC-MHC and T102S-MHC ligands.

Delay time was extracted from all production binding events by measuring the time from pMHC:TCR binding to the earliest detection of condensation. In order to quality as a delay time, binding of pMHC to TCR must be observed, and pMHC:TCR must remain isolated for the duration of the delay period. Any pMHC:TCR events that come within 1μm of another condensate are excluded. Additionally, condensates must be stable for at least 8 seconds to avoid spontaneous density fluctuations.

Quantitative Fluorescence

To estimate the number of LAT-EGFP molecules within the discrete condensates we first calculate the number of fluorescent LAT molecules, N_{LAT}^{Fl} , by determining the mean integrated intensity of *single* LAT-EGFP molecules on the plasma membrane (S_I). This can be done either by finding a low-expressing cell or bleaching the cell down to single molecule densities. Ideally, we could divide the cluster intensity (C_I) by the mean PSF intensity:

$$N_{LAT}^{Fl} = \frac{C_I}{S_I}$$

However, there are a few caveats. First, it is often the case that S_I is imaged at different power, exposure, and EMCCD gain conditions than for bulk clusters C_I. This is done to stay within the dynamic range of the camera at both expression levels.

Fortunately, for many imaging systems, linear changes in power, exposure, and gain result in linear changes in intensity, but this must be verified. For example, the Andor iXon887 feature RealGain™ technology allows linear inference in the number of incident photoelectrons from fluorescent photons. And LED lasers allow for precise control of power input.

Once linearity in power, gain, and exposure is established then the following normalization will account for the shifting intensity values recorded under different conditions:

$$N_{LAT}^{Fl} = \frac{C_I \,/C_{\text{gain}} C_{\text{power}} C_{\text{exposure}}}{S_I / S_{\text{gain}} S_{\text{power}} S_{\text{exposure}}}$$

For example, a given cluster intensity C_I recorded at $C_{\text{power}} = 2$ will represent half the number of molecules if the same intensity value is recorded with $C_{\text{power}} = 4$.

The second caveat is to consider how much of the cellular background LAT is participating within the cluster. If there exists an equal density of free LAT within the cluster region as there does outside the cluster region, then one should use the net cluster intensity to determine the number of extra molecules that exist within the cluster region. However, if the density of free LAT within the cluster region is zero, then the total intensity of the cluster should be used to calculate the number of clustered molecules.

In practice, we used the midpoint between the net intensity and the total intensity.

$$C_I = \frac{1}{2}(C_{\text{total}} + C_{\text{net}})$$

Next, quantification of the western blot will reveal the ratio of exogenous to endogenous LAT (Figure S2F), $\alpha = \frac{\text{endo}}{\text{exo}}$. In this study, α was determined to be 0.60, and the resulting expression for total LAT is:

$$N_{LAT} = (1 + \alpha)N_{LAT}^{Fl}$$

Faction LAT Clustered Calculation from Ilastik Probability Matrices

TIRF image of LAT-EGFP taken from Jurkat cells (either wild type or PLCγ1 knock-down) were processed by an ilastik model that was trained to identify LAT condensate features. The output of the model was a set of three probability matrices for each TIRF image corresponding to condensates, cell background, and image background (cell void areas). Each TIRF image pixel is assigned a probability value (from zero to one) for being one the three features (condensate, cell background, and image background).

To approximate the fraction clustered for each cell, the condensate and cell background probability matrices were first filtered to remove low probability pixels using an arbitrary threshold (≤ 0.2 removed). The filtered probability matrices were then summed in both dimensions to yield a single value for each matrix denoted as: $s_{clustered}$ and $s_{cell\ BG}$. The fraction clustered was then estimated using the following equation:

$$Fraction\ clustered = \frac{s_{clustered}}{s_{clustered} + s_{cell\ BG}}$$

Estimating Cellular Concentration

Using the protein abundance measured by Voisinne and colleagues (*117*), we calculated the cellular concentration by approximating T cells as spheres that are 10μm in diameter. Therefore, the cellular volume is ~524 μm^3 (or 5.24×10^{-13} L). Cellular concentration is then simply calculated dividing the protein abundance (in moles) by the cell volume.

Rinat Calibrations

Before labeling biAb with Atto647N, we performed the NFAT titration experiments for all BCMA constructs of different heights using dark biAb. Since the density was unknown, our preliminary NFAT titration curves were a function of the BCMA solution concentration used during the protein incubation adsorption step (See **Figure 5-2**). We did this to avoid causing disruptions to the biAb. After characterizing labeled biAb on supported bilayers (**Figure 4-9**), we measured calibration curves to convert the solution concentrations in **Figure 5-2** to molecular density (i.e., molecules/μm^2). To do this, we incubated bilayers with three different concentrations of each BCMA construct, attached

biAb-Atto647N, and measured the resulting single molecule densities. We then plotted and performed linear fits on the calibration data as shown in **Figure 5-3**. Extracting fit parameters, we converted the concentration data in **Figure 5-2** to obtain the density-based BCMA:biAb titration curves shown in **Figure 4-10D**.

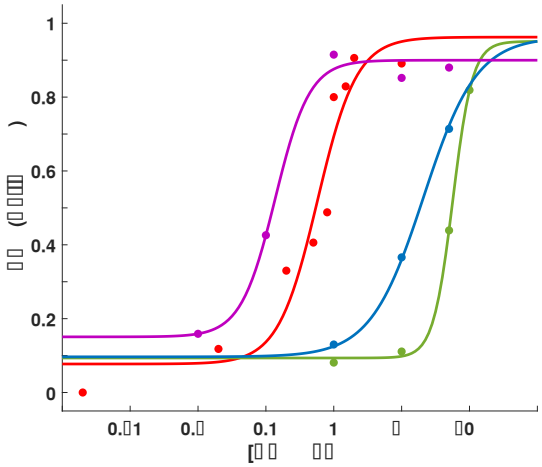

Figure 5-2: NFAT titration curves based on solution incubation concentration.

$$Sigmoidal\ fit = \frac{a}{1 + 10^{b(x-c)}} + d$$

Where a, b, c, and d are fitting parameters. We justified fitting with four parameters since fitting was only used for visualization purposes.

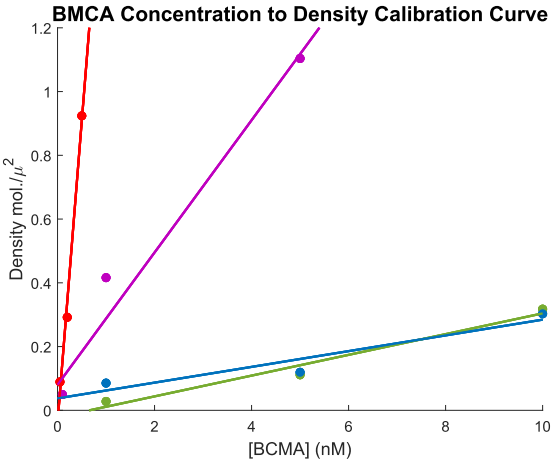

Figure 5-3: Concentration to density calibration curves for BCMA of different heights.

Since the amount of Ni-chelating lipids were in excess to BCMA solution concentration during the membrane adsorption step, BCMA membrane-binding follows pseudo-first order kinetics. This is given by:

$$\rho_{BCMA} = [BCMA]e^{k^*t}$$

Where ρ_{BCMA} is the density of BCMA on the membrane and k^* is the pseudo-first order rate constant. Since BCMA incubation time (t) is the same for all experiments, the term e^{k^*t} is constant. Therefore, the relationship between solution concentration and bilayer density is linear as seen in **Figure 5-3**. We note that the equation above converts molar units, which are three-dimensional, to surface density, which is two-dimensional. Therefore, the more accurate form of the equation would use number of molecules (n) such as:

$$n_{BCMA:bilayer} = n_{BCMA:solution}e^{k^*t}$$

6 | References

1. K. Matsui, J. J. Boniface, P. Steffner, P. A. Reay, M. M. Davis, Kinetics of T-cell receptor binding to peptide/I-E(k) complexes: Correlation of the dissociation rate with T-cell responsiveness. *Proc. Natl. Acad. Sci. U. S. A.* **91**, 12862–12866 (1994).
2. R. J. Fisher, M. Fivash, M. Corr, A. E. Slanetz, L. F. Boyd, M. T. Jelonek, S. Khilko, B. K. Al-Ramadi, Y. S. Kim, S. E. Maher, A. L. M. Bothwell, D. H. Margulies, T cell receptor-MHC class I peptide interactions: Affinity, kinetics, and specificity. *Science.* **268**, 115–117 (1995).
3. M. A. Daniels, E. Teixeiro, J. Gill, B. Hausmann, D. Roubaty, K. Holmberg, G. Werlen, G. A. Holländer, N. R. J. Gascoigne, E. Palmer, Thymic selection threshold defined by compartmentalization of Ras/MAPK signalling. *Nature*. **444**, 724–729 (2006).
4. B. B. Au-Yeung, J. Zikherman, J. L. Mueller, J. F. Ashouri, M. Matloubian, D. A. Cheng, Y. Chen, K. M. Shokat, A. Weiss, A sharp T-cell antigen receptor signaling threshold for T-cell proliferation. *Proc. Natl. Acad. Sci. U. S. A.* **111** (2014), doi:10.1073/pnas.1413726111.
5. P. François, G. Altan-Bonnet, The Case for Absolute Ligand Discrimination: Modeling Information Processing and Decision by Immune T Cells. *J. Stat. Phys.* **162**, 1130–1152 (2016).
6. G. J. Kersh, E. N. Kersh, D. H. Fremont, P. M. Allen, High- and Low-Potency Ligands with Similar Affinities for the TCR. *Immunity*. **9**, 817–826 (1998).
7. D. S. Lyons, S. A. Lieberman, J. Hampl, J. J. Boniface, Y. H. Chien, L. J. Berg, M. M. Davis, A TCR binds to antagonist ligands with lower affinities and faster dissociation rates than to agonists. *Immunity*. **5**, 53–61 (1996).
8. T. W. McKeithan, Kinetic proofreading in T-cell receptor signal transduction. *Proc. Natl. Acad. Sci. U. S. A.* **92**, 5042–5046 (1995).
9. D. Naeher, M. A. Daniels, B. Hausmann, P. Guillaume, I. Luescher, E. Palmer, A constant affinity threshold for T cell tolerance. *J. Exp. Med.* **204**, 2553–2559 (2007).

10. J. Huang, M. Brameshuber, X. Zeng, J. Xie, Q. jing Li, Y. hsiu Chien, S. Valitutti, M. M. Davis, A Single Peptide-Major Histocompatibility Complex Ligand Triggers Digital Cytokine Secretion in CD4+ T Cells. *Immunity*. **39**, 846–857 (2013).
11. D. J. Irvine, M. A. Purbhoo, M. Krogsgaard, M. M. Davis, Direct observation of ligand recognition by T cells. *Nature*. **419**, 845–849 (2002).
12. J. J. Y. Lin, S. T. Low-Nam, K. N. Alfieri, D. B. McAffee, N. C. Fay, J. T. Groves, Mapping the stochastic sequence of individual ligand-receptor binding events to cellular activation: T cells act on the rare events. *Sci. Signal.* **12** (2019), doi:10.1126/SCISIGNAL.AAT8715.
13. G. P. O'Donoghue, R. M. Pielak, A. A. Smoligovets, J. J. Lin, J. T. Groves, Direct single molecule measurement of TCR triggering by agonist pMHC in living primary T cells. *Elife*. **2013** (2013), doi:10.7554/ELIFE.00778.
14. R. M. Pielak, G. P. O'Donoghue, J. J. Lin, K. N. Alfieri, N. C. Fay, S. T. Low-Nam, J. T. Groves, Early T cell receptor signals globally modulate ligand:receptor affinities during antigen discrimination. *Proc. Natl. Acad. Sci. U. S. A.* **114**, 12190–12195 (2017).
15. Y. Sykulev, M. Joo, I. Vturina, T. J. Tsomides, H. N. Eisen, Evidence that a Single Peptide–MHC Complex on a Target Cell Can Elicit a Cytolytic T Cell Response. *Immunity*. **4**, 565–571 (1996).
16. B. B. Au-Yeung, N. H. Shah, L. Shen, A. Weiss, ZAP-70 in Signaling, Biology, and Disease. *Annu. Rev. Immunol.* **36**, 127–156 (2018).
17. A. K. Chakraborty, A. Weiss, Insights into the initiation of TCR signaling. *Nat. Immunol.* **15**, 798–807 (2014).
18. S. M. Alam, P. J. Travers, J. L. Wung, W. Nasholds, S. Redpath, S. C. Jameson, N. R. J. Gascoigne, T-cell-receptor affinity and thymocyte positive selection. *Nature*. **381**, 616–620 (1996).
19. R. S. Ganti, W.-L. Lo, D. B. McAffee, J. T. Groves, A. Weiss, A. K. Chakraborty, How the T cell signaling network processes information to discriminate between self and agonist ligands. *Proc. Natl. Acad. Sci. U. S. A.* **117**, 26020–26030 (2020).
20. M. Iwashima, B. Irving, N. van Oers, A. Chan, A. Weiss, Sequential interactions of the TCR with two distinct cytoplasmic tyrosine kinases. *Science.* **263**, 1136–1139 (1994).
21. S. Deindl, T. A. Kadlecek, T. Brdicka, X. Cao, A. Weiss, J. Kuriyan, Structural Basis for the Inhibition of Tyrosine Kinase Activity of ZAP-70. *Cell*. **129**, 735–746 (2007).
22. C. Klammt, L. Novotná, D. T. Li, M. Wolf, A. Blount, K. Zhang, J. R. Fitchett, B. F. Lillemeier, T cell receptor dwell times control the kinase activity of Zap70. *Nat. Immunol.* **16**, 961–969 (2015).
23. H. Wang, T. A. Kadlecek, B. B. Au-Yeung, H. E. S. Goodfellow, L.-Y. Hsu, T. S. Freedman, A. Weiss, ZAP-70: An Essential Kinase in T-cell Signaling. *Cold Spring Harb. Perspect. Biol.* **2**, a002279 (2010).
24. W. Zhang, J. Sloan-Lancaster, J. Kitchen, R. P. Trible, L. E. Samelson, LAT: The ZAP-70 Tyrosine Kinase Substrate that Links T Cell Receptor to Cellular Activation. *Cell*. **92**, 83–92 (1998).

25. N. H. Shah, Q. Wang, Q. Yan, D. Karandur, T. A. Kadlecek, I. R. Fallahee, W. P. Russ, R. Ranganathan, A. Weiss, J. Kuriyan, An electrostatic selection mechanism controls sequential kinase signaling downstream of the T cell receptor. *Elife*. **5** (2016), doi:10.7554/ELIFE.20105.
26. L. Balagopalan, R. L. Kortum, N. P. Coussens, V. A. Barr, L. E. Samelson, The Linker for Activation of T Cells (LAT) Signaling Hub: From Signaling Complexes to Microclusters *. *J. Biol. Chem.* **290**, 26422–26429 (2015).
27. R. J. Brownlie, R. Zamoyska, T cell receptor signalling networks: branched, diversified and bounded. *Nat. Rev. Immunol.* **13**, 257–269 (2013).
28. T. S. Finco, T. Kadlecek, W. Zhang, L. E. Samelson, A. Weiss, LAT Is Required for TCR-Mediated Activation of PLCγ1 and the Ras Pathway. *Immunity*. **9**, 617–626 (1998).
29. L. E. Samelson, Signal Transduction Mediated by the T Cell Antigen Receptor: The Role of Adapter Proteins*. *Annu. Rev. Immunol.* **20**, 371–394 (2003).
30. W. Zhang, R. P. Trible, L. E. Samelson, LAT Palmitoylation: Its Essential Role in Membrane Microdomain Targeting and Tyrosine Phosphorylation during T Cell Activation. *Immunity*. **9**, 239–246 (1998).
31. W. Zhang, R. P. Trible, M. Zhu, S. K. Liu, C. J. McGlade, L. E. Samelson, Association of Grb2, Gads, and phospholipase C-γ1 with phosphorylated LAT tyrosine residues: Effect of LAT tyrosine mutations on T cell antigen receptor-mediated signaling. *J. Biol. Chem.* **275**, 23355–23361 (2000).
32. J. Lin, A. Weiss, Identification of the Minimal Tyrosine Residues Required for Linker for Activation of T Cell Function. *J. Biol. Chem.* **276**, 29588–29595 (2001).
33. M. Zhu, E. Janssen, W. Zhang, Minimal Requirement of Tyrosine Residues of Linker for Activation of T Cells in TCR Signaling and Thymocyte Development. *J. Immunol.* **170**, 325–333 (2003).
34. J. C. D. Houtman, Y. Higashimoto, N. Dimasi, S. Cho, H. Yamaguchi, B. Bowden, C. Regan, E. L. Malchiodi, R. Mariuzza, P. Schuck, E. Appella, L. E. Samelson, Binding Specificity of Multiprotein Signaling Complexes Is Determined by Both Cooperative Interactions and Affinity Preferences†. *Biochemistry*. **43**, 4170–4178 (2004).
35. W. Y. C. Huang, J. A. Ditlev, H.-K. Chiang, M. K. Rosen, J. T. Groves, Allosteric Modulation of Grb2 Recruitment to the Intrinsically Disordered Scaffold Protein, LAT, by Remote Site Phosphorylation. *J. Am. Chem. Soc.* **139**, 18009–18015 (2017).
36. J. E. Smith-Garvin, G. A. Koretzky, M. S. Jordan, T Cell Activation. *Annu. Rev. Immunol.* **27**, 591–619 (2009).
37. S. M. Stanford, N. Rapini, N. Bottini, Regulation of TCR signalling by tyrosine phosphatases: from immune homeostasis to autoimmunity. *Immunology*. **137**, 1–19 (2012).
38. J. C. D. Houtman, H. Yamaguchi, M. Barda-Saad, A. Braiman, B. Bowden, E. Appella, P. Schuck, L. E. Samelson, Oligomerization of signaling complexes by the multipoint binding of GRB2 to both LAT and SOS1. *Nat. Struct. Mol. Biol.* **13**, 798–805 (2006).

39. R. L. Kortum, L. Balagopalan, C. P. Alexander, J. Garcia, J. M. Pinski, R. K. Merrill, P. H. Nguyen, W. Li, I. Agarwal, I. O. Akpan, C. L. Sommers, L. E. Samelson, The Ability of Sos1 to Oligomerize the Adaptor Protein LAT Is Separable from Its Guanine Nucleotide Exchange Activity in Vivo. *Sci. Signal.* **6**, ra99–ra99 (2013).
40. A. Nag, M. I. Monine, J. R. Faeder, B. Goldstein, Aggregation of Membrane Proteins by Cytosolic Cross-Linkers: Theory and Simulation of the LAT-Grb2-SOS1 System. *Biophys. J.* **96**, 2604–2623 (2009).
41. S. C. Bunnell, D. I. Hong, J. R. Kardon, T. Yamazaki, C. J. McGlade, V. A. Barr, L. E. Samelson, T cell receptor ligation induces the formation of dynamically regulated signaling assemblies. *J. Cell Biol.* **158**, 1263–1275 (2002).
42. X. Su, J. A. Ditlev, E. Hui, W. Xing, S. Banjade, J. Okrut, D. S. King, J. Taunton, M. K. Rosen, R. D. Vale, Phase separation of signaling molecules promotes T cell receptor signal transduction. *Science.* **352**, 595–599 (2016).
43. W. Y. C. Huang, Q. Yan, W.-C. Lin, J. K. Chung, S. D. Hansen, S. M. Christensen, H.-L. Tu, J. Kuriyan, J. T. Groves, Phosphotyrosine-mediated LAT assembly on membranes drives kinetic bifurcation in recruitment dynamics of the Ras activator SOS. *Proc. Natl. Acad. Sci. U. S. A.* **113**, 8218–8223 (2016).
44. W. Y. C. Huang, S. Alvarez, Y. Kondo, Y. K. Lee, J. K. Chung, H. Y. M. Lam, K. H. Biswas, J. Kuriyan, J. T. Groves, A molecular assembly phase transition and kinetic proofreading modulate Ras activation by SOS. *Science.* **363**, 1098–1103 (2019).
45. T. O. Eichmann, A. Lass, DAG tales: the multiple faces of diacylglycerol—stereochemistry, metabolism, and signaling. *Cell. Mol. Life Sci.* **72**, 3931–3952 (2015).
46. E. Kania, G. Roest, T. Vervliet, J. B. Parys, G. Bultynck, IP3 Receptor-Mediated Calcium Signaling and Its Role in Autophagy in Cancer. *Front. Oncol.* **0**, 140 (2017).
47. A. Gresset, J. Sondek, T. K. Harden, The Phospholipase C Isozymes and Their Regulation. *Subcell. Biochem.* **58**, 61–94 (2012).
48. N. Hajicek, N. C. Keith, E. Siraliev-Perez, B. R. S. Temple, W. Huang, Q. Zhang, T. K. Harden, J. Sondek, Structural basis for the activation of PLC-γ isozymes by phosphorylation and cancer-associated mutations. *Elife*. **8**, 1–25 (2019).
49. J. C. D. Houtman, R. A. Houghtling, M. Barda-Saad, Y. Toda, L. E. Samelson, Early Phosphorylation Kinetics of Proteins Involved in Proximal TCR-Mediated Signaling Pathways. *J. Immunol.* **175**, 2449–2458 (2005).
50. W.-L. Lo, N. H. Shah, S. A. Rubin, W. Zhang, V. Horkova, I. R. Fallahee, O. Stepanek, L. I. Zon, J. Kuriyan, A. Weiss, Slow phosphorylation of a tyrosine residue in LAT optimizes T cell ligand discrimination. *Nat. Immunol.* **20**, 1481–1493 (2019).
51. N. Cruz-Orcutt, A. Vacaflores, S. F. Connolly, S. C. Bunnell, J. C. D. Houtman, Activated PLC-γ1 is catalytically induced at LAT but activated PLC-γ1 is localized at both LAT- and TCR-containing complexes. *Cell. Signal.* **26**, 797–805 (2014).
52. D. Beach, R. Gonen, Y. Bogin, I. G. Reischl, D. Yablonski, Dual Role of SLP-76 in Mediating T Cell Receptor-induced Activation of Phospholipase C-γ1. *J. Biol. Chem.* **282**, 2937–2946 (2007).

53. Y. Bogin, C. Ainey, D. Beach, D. Yablonski, SLP-76 mediates and maintains activation of the Tec family kinase ITK via the T cell antigen receptor-induced association between SLP-76 and ITK. *Proc. Natl. Acad. Sci. U. S. A.* **104**, 6638–6643 (2007).
54. D. Yablonski, T. Kadlecek, A. Weiss, Identification of a Phospholipase C-γ1 (PLC-γ1) SH3 Domain-Binding Site in SLP-76 Required for T-Cell Receptor-Mediated Activation of PLC-γ1 and NFAT. *Mol. Cell. Biol.* **21**, 4208–4218 (2001).
55. A. Gresset, S. N. Hicks, T. K. Harden, J. Sondek, Mechanism of Phosphorylation-induced Activation of Phospholipase C-γ Isozymes. *J. Biol. Chem.* **285**, 35836–35847 (2010).
56. N. Hajicek, T. H. Charpentier, J. R. Rush, T. K. Harden, J. Sondek, Autoinhibition and Phosphorylation-Induced Activation of Phospholipase C-γ Isozymes. *Biochemistry*. **52**, 4810–4819 (2013).
57. B. J. Irvin, B. L. Williams, A. E. Nilson, H. O. Maynor, R. T. Abraham, Pleiotropic Contributions of Phospholipase C-γ1 (PLC-γ1) to T-Cell Antigen Receptor-Mediated Signaling: Reconstitution Studies of a PLC-γ1-Deficient Jurkat T-Cell Line. *Mol. Cell. Biol.* **20**, 9149–9161 (2000).
58. L. Zeng, I. Palaia, A. Šarić, X. Su, PLCγ1 promotes phase separation of T cell signaling components. *J. Cell Biol.* **220** (2021), doi:10.1083/JCB.202009154.
59. G. Campi, R. Varma, M. L. Dustin, Actin and agonist MHC–peptide complex–dependent T cell receptor microclusters as scaffolds for signaling. *J. Exp. Med.* **202**, 1031–1036 (2005).
60. V. T. Chang, R. A. Fernandes, K. A. Ganzinger, S. F. Lee, C. Siebold, J. McColl, P. Jönsson, M. Palayret, K. Harlos, C. H. Coles, E. Y. Jones, Y. Lui, E. Huang, R. J. C. Gilbert, D. Klenerman, A. R. Aricescu, S. J. Davis, Initiation of T cell signaling by CD45 segregation at "close contacts." *Nat. Immunol.* **17**, 574–582 (2016).
61. A. Grakoui, S. K. Bromley, C. Sumen, M. M. Davis, A. S. Shaw, P. M. Allen, M. L. Dustin, The Immunological Synapse: A Molecular Machine Controlling T Cell Activation. *Science.* **285**, 221–227 (1999).
62. J. B. Huppa, M. Axmann, M. A. Mörtelmaier, B. F. Lillemeier, E. W. Newell, M. Brameshuber, L. O. Klein, G. J. Schütz, M. M. Davis, TCR–peptide–MHC interactions in situ show accelerated kinetics and increased affinity. *Nature*. **463**, 963–967 (2010).
63. Y. Ma, E. Pandzic, P. R. Nicovich, Y. Yamamoto, J. Kwiatek, S. V. Pageon, A. Benda, J. Rossy, K. Gaus, An intermolecular FRET sensor detects the dynamics of T cell receptor clustering. *Nat. Commun.* **8**, 1–11 (2017).
64. E. M. Schmid, M. H. Bakalar, K. Choudhuri, J. Weichsel, H. S. Ann, P. L. Geissler, M. L. Dustin, D. A. Fletcher, Size-dependent protein segregation at membrane interfaces. *Nat. Phys.* **12**, 704–711 (2016).
65. M. J. Taylor, K. Husain, Z. J. Gartner, S. Mayor, R. D. Vale, A DNA-Based T Cell Receptor Reveals a Role for Receptor Clustering in Ligand Discrimination. *Cell*. **169**, 108-119.e20 (2017).
66. Y. Zhao, D. L. Harrison, Y. Song, J. Ji, J. Huang, E. Hui, Antigen-Presenting Cell-Intrinsic PD-1 Neutralizes PD-L1 in cis to Attenuate PD-1 Signaling in T Cells. *Cell Rep.* **24**, 379-390.e6 (2018).

67. J. T. Groves, M. L. Dustin, Supported planar bilayers in studies on immune cell adhesion and communication. *J. Immunol. Methods*. **278**, 19–32 (2003).
68. M. L. Dustin, J. T. Groves, Receptor Signaling Clusters in the Immune Synapse. *Annu. Rev. Biophys.* **41**, 543–556 (2012).
69. B. N. Manz, B. L. Jackson, R. S. Petit, M. L. Dustin, J. Groves, T-cell triggering thresholds are modulated by the number of antigen within individual T-cell receptor clusters. *Proc. Natl. Acad. Sci. U. S. A.* **108**, 9089–9094 (2011).
70. J. Yi, L. Balagopalan, T. Nguyen, K. M. McIntire, L. E. Samelson, TCR microclusters form spatially segregated domains and sequentially assemble in calcium-dependent kinetic steps. *Nat. Commun.* **10**, 1–13 (2019).
71. K. H. Biswas, J. T. Groves, Hybrid Live Cell–Supported Membrane Interfaces for Signaling Studies. *Annu. Rev. Biophys.* **48**, 537–562 (2019).
72. A. A. Brian, H. M. McConnell, Allogeneic stimulation of cytotoxic T cells by supported planar membranes. *Proc. Natl. Acad. Sci. U. S. A.* **81**, 6159–6163 (1984).
73. P. F. Céspedes, D. Beckers, M. L. Dustin, E. Sezgin, Model membrane systems to reconstitute immune cell signaling. *FEBS J.* **288**, 1070–1090 (2021).
74. K. D. Mossman, G. Campi, J. T. Groves, M. L. Dustin, Altered TCR Signaling from Geometrically Repatterned Immunological Synapses. *Science.* **310**, 1191–1193 (2005).
75. J. A. Nye, J. T. Groves, Kinetic Control of Histidine-Tagged Protein Surface Density on Supported Lipid Bilayers. *Langmuir*. **24**, 4145–4149 (2008).
76. J. Kaye, M.-L. Hsu, M.-E. Sauron, S. C. Jameson, N. R. J. Gascoigne, S. M. Hedrick, Selective development of CD4+ T cells in transgenic mice expressing a class II MHC-restricted antigen receptor. *Nature*. **341**, 746–749 (1989).
77. S. Morita, T. Kojima, T. Kitamura, Plat-E: an efficient and stable system for transient packaging of retroviruses. *Gene Ther.* **7**, 1063–1066 (2000).
78. J. H. Kim, S.-R. Lee, L.-H. Li, H.-J. Park, J.-H. Park, K. Y. Lee, M.-K. Kim, B. A. Shin, S.-Y. Choi, High Cleavage Efficiency of a 2A Peptide Derived from Porcine Teschovirus-1 in Human Cell Lines, Zebrafish and Mice. *PLoS One*. **6**, e18556 (2011).
79. L. Limozin, K. Sengupta, Quantitative Reflection Interference Contrast Microscopy (RICM) in Soft Matter and Cell Adhesion. *ChemPhysChem*. **10**, 2752–2768 (2009).
80. J. Zlatanova, K. van Holde, Single-Molecule Biology: What Is It and How Does It Work? *Mol. Cell*. **24**, 317–329 (2006).
81. J. K. Jaiswal, S. M. Simon, Imaging single events at the cell membrane. *Nat. Chem. Biol.* **3**, 92–98 (2007).
82. A. D. Douglass, R. D. Vale, Single-Molecule Microscopy Reveals Plasma Membrane Microdomains Created by Protein-Protein Networks that Exclude or Trap Signaling Molecules in T Cells. *Cell*. **121**, 937–950 (2005).
83. L. Balagopalan, J. Yi, T. Nguyen, K. M. McIntire, A. S. Harned, K. Narayan, L. E. Samelson, Plasma membrane LAT activation precedes vesicular recruitment defining two phases of early T-cell activation. *Nat. Commun.* **9**, 1–17 (2018).
84. M. Huse, L. O. Klein, A. T. Girvin, J. M. Faraj, Q. J. Li, M. S. Kuhns, M. M. Davis, Spatial and Temporal Dynamics of T Cell Receptor Signaling with a Photoactivatable Agonist. *Immunity*. **27**, 76–88 (2007).

85. A. Muhammad, H. B. Schiller, F. Forster, P. Eckerstorfer, R. Geyeregger, V. Leksa, G. J. Zlabinger, M. Sibilia, A. Sonnleitner, W. Paster, H. Stockinger, Sequential Cooperation of CD2 and CD48 in the Buildup of the Early TCR Signalosome. *J. Immunol.* **182**, 7672–7680 (2009).
86. A. L. DeMond, K. D. Mossman, T. Starr, M. L. Dustin, J. T. Groves, T Cell Receptor Microcluster Transport through Molecular Mazes Reveals Mechanism of Translocation. *Biophys. J.* **94**, 3286–3292 (2008).
87. Y. Yu, N. C. Fay, A. A. Smoligovets, H.-J. Wu, J. T. Groves, Myosin IIA Modulates T Cell Receptor Transport and CasL Phosphorylation during Early Immunological Synapse Formation. *PLoS One*. **7**, e30704 (2012).
88. T. Yokosuka, K. Sakata-Sogawa, W. Kobayashi, M. Hiroshima, A. Hashimoto-Tane, M. Tokunaga, M. L. Dustin, T. Saito, Newly generated T cell receptor microclusters initiate and sustain T cell activation by recruitment of Zap70 and SLP-76. *Nat. Immunol. 2005 612*. **6**, 1253–1262 (2005).
89. H. Soares, R. Henriques, M. Sachse, L. Ventimiglia, M. A. Alonso, C. Zimmer, M.-I. Thoulouze, A. Alcover, Regulated vesicle fusion generates signaling nanoterritories that control T cell activation at the immunological synapse. *J. Exp. Med.* **210**, 2415–2433 (2013).
90. M. Raab, Y. Lu, K. Kohler, X. Smith, K. Strebhardt, C. E. Rudd, LFA-1 activates focal adhesion kinases FAK1/PYK2 to generate LAT-GRB2-SKAP1 complexes that terminate T-cell conjugate formation. *Nat. Commun.* **8**, 1–15 (2017).
91. T. J. Crites, K. Padhan, J. Muller, M. Krogsgaard, P. R. Gudla, S. J. Lockett, R. Varma, TCR Microclusters Pre-Exist and Contain Molecules Necessary for TCR Signal Transduction. *J. Immunol.* **193**, 56–67 (2014).
92. F. Marangoni, T. T. Murooka, T. Manzo, E. Y. Kim, E. Carrizosa, N. M. Elpek, T. R. Mempel, The Transcription Factor NFAT Exhibits Signal Memory during Serial T Cell Interactions with Antigen-Presenting Cells. *Immunity*. **38**, 237–249 (2013).
93. H. J. Melichar, J. O. Ross, P. Herzmark, K. A. Hogquist, E. A. Robey, Distinct Temporal Patterns of T Cell Receptor Signaling During Positive Versus Negative Selection in Situ. *Sci. Signal.* **6**, ra92–ra92 (2013).
94. M. Podtschaske, U. Benary, S. Zwinger, T. Höfer, A. Radbruch, R. Baumgrass, Digital NFATc2 Activation per Cell Transforms Graded T Cell Receptor Activation into an All-or-None IL-2 Expression. *PLoS One*. **2**, e935 (2007).
95. O. Stepanek, A. S. Prabhakar, C. Osswald, C. G. King, A. Bulek, D. Naeher, M. Beaufils-Hugot, M. L. Abanto, V. Galati, B. Hausmann, R. Lang, D. K. Cole, E. S. Huseby, A. K. Sewell, A. K. Chakraborty, E. Palmer, Coreceptor Scanning by the T Cell Receptor Provides a Mechanism for T Cell Tolerance. *Cell*. **159**, 333–345 (2014).
96. D. K. Tischer, O. D. Weiner, Light-based tuning of ligand half-life supports kinetic proofreading model of T cell signaling. *Elife*. **8** (2019), doi:10.7554/ELIFE.42498.
97. O. S. Yousefi, M. Günther, M. Hörner, J. Chalupsky, M. Wess, S. M. Brandl, R. W. Smith, C. Fleck, T. Kunkel, M. D. Zurbriggen, T. Höfer, W. Weber, W. W. A. Schamel, Optogenetic control shows that kinetic proofreading regulates the activity of the T cell receptor. *Elife*. **8** (2019), doi:10.7554/ELIFE.42475.

98. E. Sherman, V. Barr, S. Manley, G. Patterson, L. Balagopalan, I. Akpan, C. K. Regan, R. K. Merrill, C. L. Sommers, J. Lippincott-Schwartz, L. E. Samelson, Functional Nanoscale Organization of Signaling Molecules Downstream of the T Cell Antigen Receptor. *Immunity*. **35**, 705–720 (2011).
99. E. Sherman, V. A. Barr, R. K. Merrill, C. K. Regan, C. L. Sommers, L. E. Samelson, Hierarchical nanostructure and synergy of multimolecular signalling complexes. *Nat. Commun.* **7**, 1–13 (2016).
100. G. Gross, Z. Eshhar, Therapeutic Potential of T Cell Chimeric Antigen Receptors (CARs) in Cancer Treatment: Counteracting Off-Tumor Toxicities for Safe CAR T Cell Therapy. *Annu. Rev. Pharmacol. Toxicol.* **56**, 59–83 (2016).
101. A. F. Labrijn, M. L. Janmaat, J. M. Reichert, P. W. H. I. Parren, Bispecific antibodies: a mechanistic review of the pipeline. *Nat. Rev. Drug Discov.* **18**, 585–608 (2019).
102. G. P. Linette, E. A. Stadtmauer, M. V. Maus, A. P. Rapoport, B. L. Levine, L. Emery, L. Litzky, A. Bagg, B. M. Carreno, P. J. Cimino, G. K. Binder-Scholl, D. P. Smethurst, A. B. Gerry, N. J. Pumphrey, A. D. Bennett, J. E. Brewer, J. Dukes, J. Harper, H. K. Tayton-Martin, B. K. Jakobsen, N. J. Hassan, M. Kalos, C. H. June, Cardiovascular toxicity and titin cross-reactivity of affinity-enhanced T cells in myeloma and melanoma. *Blood*. **122**, 863–871 (2013).
103. J. Hellmeier, R. Platzer, A. S. Eklund, T. Schlichthaerle, A. Karner, V. Motsch, M. C. Schneider, E. Kurz, V. Bamieh, M. Brameshuber, J. Preiner, R. Jungmann, H. Stockinger, G. J. Schütz, J. B. Huppa, E. Sevcsik, DNA origami demonstrate the unique stimulatory power of single pMHCs as T cell antigens. *Proc. Natl. Acad. Sci. U. S. A.* **118** (2021), doi:10.1073/PNAS.2016857118.
104. C. L. Bonifant, H. J. Jackson, R. J. Brentjens, K. J. Curran, Toxicity and management in CAR T-cell therapy. *Mol. Ther. - Oncolytics*. **3**, 16011 (2016).
105. C. H. J. Lamers, S. Sleijfer, S. Van Steenbergen, P. Van Elzakker, B. Van Krimpen, C. Groot, A. Vulto, M. Den Bakker, E. Oosterwijk, R. Debets, J. W. Gratama, Treatment of Metastatic Renal Cell Carcinoma With CAIX CAR-engineered T cells: Clinical Evaluation and Management of On-target Toxicity. *Mol. Ther.* **21**, 904–912 (2013).
106. B. Salzer, C. M. Schueller, C. U. Zajc, T. Peters, M. A. Schoeber, B. Kovacic, M. C. Buri, E. Lobner, O. Dushek, J. B. Huppa, C. Obinger, E. M. Putz, W. Holter, M. W. Traxlmayr, M. Lehner, Engineering AvidCARs for combinatorial antigen recognition and reversible control of CAR function. *Nat. Commun.* **11**, 1–16 (2020).
107. A. I. Salter, A. Rajan, J. J. Kennedy, R. G. Ivey, S. A. Shelby, I. Leung, M. L. Templeton, V. Muhunthan, V. Voillet, D. Sommermeyer, J. R. Whiteaker, R. Gottardo, S. L. Veatch, A. G. Paulovich, S. R. Riddell, Comparative analysis of TCR and CAR signaling informs CAR designs with superior antigen sensitivity and in vivo function. *Sci. Signal.* **14**, eabe2606 (2021).
108. M. Trebak, J.-P. Kinet, Calcium signalling in T cells. *Nat. Rev. Immunol.* **19**, 154–169 (2019).
109. J. C. Stone, Regulation and Function of the RasGRP Family of Ras Activators in Blood Cells: *Genes Cancer*. **2**, 320–334 (2011).

110. A. Manna, H. Zhao, J. Wada, L. Balagopalan, H. D. Tagad, E. Appella, P. Schuck, L. E. Samelson, Cooperative assembly of a four-molecule signaling complex formed upon T cell antigen receptor activation. *Proc. Natl. Acad. Sci. U. S. A.* **115**, E11914–E11923 (2018).
111. C. Wu, M. H. Ma, K. R. Brown, M. Geisler, L. Li, E. Tzeng, C. Y. H. Jia, I. Jurisica, S. S.-C. Li, Systematic identification of SH3 domain-mediated human protein–protein interactions by peptide array target screening. *Proteomics*. **7**, 1775–1785 (2007).
112. C. Sommer, C. Straehle, U. Kothe, F. A. Hamprecht, Ilastik: Interactive learning and segmentation toolkit. *Proc. - Int. Symp. Biomed. Imaging*, 230–233 (2011).
113. C. J. Serrano, L. Graham, K. DeBell, R. Rawat, M. C. Veri, E. Bonvini, B. L. Rellahan, I. G. Reischl, A New Tyrosine Phosphorylation Site in PLCγ1: The Role of Tyrosine 775 in Immune Receptor Signaling. *J. Immunol.* **174**, 6233–6237 (2005).
114. B. Stoica, K. E. DeBell, L. Graham, B. L. Rellahan, M. A. Alava, J. Laborda, E. Bonvini, The amino-terminal Src homology 2 domain of phospholipase C gamma 1 is essential for TCR-induced tyrosine phosphorylation of phospholipase C gamma 1. *J. Immunol.* **160**, 1059–66 (1998).
115. A. Braiman, M. Barda-Saad, C. L. Sommers, L. E. Samelson, Recruitment and activation of PLCγ1 in T cells: A new insight into old domains. *EMBO J.* **25**, 774–784 (2006).
116. Y. Liu, T. D. Bunney, S. Khosa, K. Macé, K. Beckenbauer, T. Askwith, S. Maslen, C. Stubbs, T. M. de Oliveira, K. Sader, M. Skehel, A. C. Gavin, C. Phillips, M. Katan, Structural insights and activating mutations in diverse pathologies define mechanisms of deregulation for phospholipase C gamma enzymes. *EBioMedicine*. **51**, 102607 (2020).
117. G. Voisinne, K. Kersse, K. Chaoui, L. Lu, J. Chaix, L. Zhang, M. Goncalves Menoita, L. Girard, Y. Ounoughene, H. Wang, O. Burlet-Schiltz, H. Luche, F. Fiore, M. Malissen, A. Gonzalez de Peredo, Y. Liang, R. Roncagalli, B. Malissen, Quantitative interactomics in primary T cells unveils TCR signal diversification extent and dynamics. *Nat. Immunol.* **20**, 1530–1541 (2019).
118. B. Rossboth, A. M. Arnold, H. Ta, R. Platzer, F. Kellner, J. B. Huppa, M. Brameshuber, F. Baumgart, G. J. Schütz, TCRs are randomly distributed on the plasma membrane of resting antigen-experienced T cells. *Nat. Immunol.* **19**, 821–827 (2018).
119. M. Brameshuber, F. Kellner, B. K. Rossboth, H. Ta, K. Alge, E. Sevcsik, J. Göhring, M. Axmann, F. Baumgart, N. R. J. Gascoigne, S. J. Davis, H. Stockinger, G. J. Schütz, J. B. Huppa, Monomeric TCRs drive T cell antigen recognition. *Nat. Immunol.* **19**, 487–496 (2018).
120. A. Manna, H. Zhao, J. Wada, L. Balagopalan, H. D. Tagad, E. Appella, P. Schuck, L. E. Samelson, Cooperative assembly of a four-molecule signaling complex formed upon T cell antigen receptor activation. *Proc. Natl. Acad. Sci. U. S. A.* **115**, E11914–E11923 (2018).
121. C. D. Thanos, K. E. Goodwill, J. U. Bowie, Oligomeric Structure of the Human EphB2 Receptor SAM Domain. *Science.* **283**, 833–836 (1999).

122. A. J. Peterson, M. Kyba, D. Bornemann, K. Morgan, H. W. Brock, J. Simon, A domain shared by the Polycomb group proteins Scm and ph mediates heterotypic and homotypic interactions. *Mol. Cell. Biol.* **17**, 6683–6692 (1997).
123. H. Liu, Y. R. Thaker, L. Stagg, H. Schneider, J. E. Ladbury, C. E. Rudd, SLP-76 Sterile α Motif (SAM) and Individual H5 α Helix Mediate Oligomer Formation for Microclusters and T-cell Activation *. *J. Biol. Chem.* **288**, 29539–29549 (2013).
124. N. P. Coussens, R. Hayashi, P. H. Brown, L. Balagopalan, A. Balbo, I. Akpan, J. C. D. Houtman, V. A. Barr, P. Schuck, E. Appella, L. E. Samelson, Multipoint Binding of the SLP-76 SH2 Domain to ADAP Is Critical for Oligomerization of SLP-76 Signaling Complexes in Stimulated T Cells. *Mol. Cell. Biol.* **33**, 4140–4151 (2013).
125. M. M. Tremblay, T. Ollinger, J. C. D. Houtman, The membrane proximal proline-rich region and correct order of C-terminal tyrosines on the adaptor protein LAT are required for TCR-mediated signaling and downstream functions. *Cell. Signal.* **76**, 109790 (2020).
126. R. C. Sterner, R. M. Sterner, CAR-T cell therapy: current limitations and potential strategies. *Blood Cancer J.* **11**, 1–11 (2021).
127. R. C. Larson, M. V. Maus, Recent advances and discoveries in the mechanisms and functions of CAR T cells. *Nat. Rev. Cancer*. **21**, 145–161 (2021).
128. S. Feins, W. Kong, E. F. Williams, M. C. Milone, J. A. Fraietta, An introduction to chimeric antigen receptor (CAR) T-cell immunotherapy for human cancer. *Am. J. Hematol.* **94**, S3–S9 (2019).
129. C. H. June, R. S. O'Connor, O. U. Kawalekar, S. Ghassemi, M. C. Milone, CAR T cell immunotherapy for human cancer. *Science.* **359**, 1361–1365 (2018).
130. J. P. Vaqué, G. Gómez-López, V. Monsálvez, I. Varela, N. Martínez, C. Pérez, O. Domínguez, O. Graña, J. L. Rodríguez-Peralto, S. M. Rodríguez-Pinilla, C. González-Vela, M. Rubio-Camarillo, E. Martín-Sánchez, D. G. Pisano, E. Papadavid, T. Papadaki, L. Requena, J. A. García-Marco, M. Méndez, M. Provencio, M. Hospital, D. Suárez-Massa, C. Postigo, D. San Segundo, M. López-Hoyos, P. L. Ortiz-Romero, M. A. Piris, M. Sánchez-Beato, PLCG1 mutations in cutaneous T-cell lymphomas. *Blood*. **123**, 2034–2043 (2014).
131. K. Kataoka, Y. Nagata, A. Kitanaka, Y. Shiraishi, T. Shimamura, J. Yasunaga, Y. Totoki, K. Chiba, A. Sato-Otsubo, G. Nagae, R. Ishii, S. Muto, S. Kotani, Y. Watatani, J. Takeda, M. Sanada, H. Tanaka, H. Suzuki, Y. Sato, Y. Shiozawa, T. Yoshizato, K. Yoshida, H. Makishima, M. Iwanaga, G. Ma, K. Nosaka, M. Hishizawa, H. Itonaga, Y. Imaizumi, W. Munakata, H. Ogasawara, T. Sato, K. Sasai, K. Muramoto, M. Penova, T. Kawaguchi, H. Nakamura, N. Hama, K. Shide, Y. Kubuki, T. Hidaka, T. Kameda, T. Nakamaki, K. Ishiyama, S. Miyawaki, S.-S. Yoon, K. Tobinai, Y. Miyazaki, A. Takaori-Kondo, F. Matsuda, K. Takeuchi, O. Nureki, H. Aburatani, T. Watanabe, T. Shibata, M. Matsuoka, S. Miyano, K. Shimoda, S. Ogawa, Integrated molecular analysis of adult T cell leukemia/lymphoma. *Nat. Genet.* **47**, 1304–1315 (2015).
132. L. Balagopalan, V. A. Barr, C. L. Sommers, M. Barda-Saad, A. Goyal, M. S. Isakowitz, L. E. Samelson, c-Cbl-Mediated Regulation of LAT-Nucleated Signaling Complexes. *Mol. Cell. Biol.* **27**, 8622–8636 (2007).

133. L. Balagopalan, H. Malik, K. M. McIntire, J. A. Garvey, T. Nguyen, A. B. Rodriguez-Peña, L. E. Samelson, Bypassing ubiquitination enables LAT recycling to the cell surface and enhanced signaling in T cells. *PLoS One*. **15**, e0229036 (2020).
134. M. Hong, T. W. Moody, Vasopressin elevates cytosolic calcium in small cell lung cancer cells. *Peptides*. **12**, 1315–1319 (1991).
135. M. V. Ellis, S. R. James, O. Perisic, C. P. Downes, R. L. Williams, M. Katan, Catalytic Domain of Phosphoinositide-specific Phospholipase C (PLC): MUTATIONAL ANALYSIS OF RESIDUES WITHIN THE ACTIVE SITE AND HYDROPHOBIC RIDGE OF PLCδ1 *. *J. Biol. Chem.* **273**, 11650–11659 (1998).
136. P. S. Huang, L. Davis, H. Huber, P. J. Goodhart, R. E. Wegrzyn, A. Oliff, D. C. Heimbrook, An SH3 domain is required for the mitogenic activity of microinjected phospholipase C-γ1. *FEBS Lett.* **358**, 287–292 (1995).
137. Z. Kouchi, T. Shikano, Y. Nakamura, H. Shirakawa, K. Fukami, S. Miyazaki, The Role of EF-hand Domains and C2 Domain in Regulation of Enzymatic Activity of Phospholipase Cζ *. *J. Biol. Chem.* **280**, 21015–21021 (2005).
138. D. Zhang, L. Aravind, Identification of novel families and classification of the C2 domain superfamily elucidate the origin and evolution of membrane targeting activities in eukaryotes. *Gene*. **469**, 18–30 (2010).
139. D. Dutta, V. A. Barr, I. Akpan, P. R. Mittelstadt, L. I. Singha, L. E. Samelson, J. D. Ashwell, Recruitment of calcineurin to the TCR positively regulates T cell activation. *Nat. Immunol.* **18**, 196–204 (2016).
140. A. C. Chan, M. Dalton, R. Johnson, G. H. Kong, T. Wang, R. Thoma, T. Kurosaki, Activation of ZAP-70 kinase activity by phosphorylation of tyrosine 493 is required for lymphocyte antigen receptor function. *EMBO J.* **14**, 2499–2508 (1995).
141. E. Bilkova, R. Pleskot, S. Rissanen, S. Sun, A. Czogalla, L. Cwiklik, T. Róg, I. Vattulainen, P. S. Cremer, P. Jungwirth, Ü. Coskun, Calcium Directly Regulates Phosphatidylinositol 4,5-Bisphosphate Headgroup Conformation and Recognition. *J. Am. Chem. Soc.* **139**, 4019–4024 (2017).
142. R. T. Abraham, A. Weiss, Jurkat T cells and development of the T-cell receptor signalling paradigm. *Nat. Rev. Immunol.* **4**, 301–308 (2004).
143. J. H. Hanke, J. P. Gardner, R. L. Dow, P. S. Changelian, W. H. Brissette, E. J. Weringer, B. A. Pollok, P. A. Connelly, Discovery of a Novel, Potent, and Src Family-selective Tyrosine Kinase Inhibitor: STUDY OF Lck- AND FynT-DEPENDENT T CELL ACTIVATION. *J. Biol. Chem.* **271**, 695–701 (1996).
144. K. Katagiri, M. Hattori, N. Minato, S. Irie, K. Takatsu, T. Kinashi, Rap1 Is a Potent Activation Signal for Leukocyte Function-Associated Antigen 1 Distinct from Protein Kinase C and Phosphatidylinositol-3-OH Kinase. *Mol. Cell. Biol.* **20**, 1956–1969 (2000).
145. E. C. Lernert, Y. Qian, A. D. Hamilton, S. M. Sebti, Disruption of Oncogenic K-Ras4B Processing and Signaling by a Potent Geranylgeranyltransferase I Inhibitor. *J. Biol. Chem.* **270**, 26770–26773 (1995).
146. G. Huyer, S. Liu, J. Kelly, J. Moffat, P. Payette, B. Kennedy, G. Tsaprailis, M. J. Gresser, C. Ramachandran, Mechanism of Inhibition of Protein-tyrosine Phosphatases by Vanadate and Pervanadate *. *J. Biol. Chem.* **272**, 843–851 (1997).

147. V. Imbert, J. Peyron, D. F. Far, B. Mari, P. Auberger, B. Rossi, Induction of tyrosine phosphorylation and T-cell activation by vanadate peroxide , an inhibitor of protein tyrosine phosphatases. *Biochem. J.* **173**, 163–173 (1994).
148. Z. Ahmed, Z. Timsah, K. M. Suen, N. P. Cook, G. R. Lee, C.-C. Lin, M. Gagea, A. A. Marti, J. E. Ladbury, Grb2 monomer–dimer equilibrium determines normal versus oncogenic function. *Nat. Commun.* **6**, 1–11 (2015).
149. C. B. McDonald, K. L. Seldeen, B. J. Deegan, M. S. Lewis, A. Farooq, Grb2 adaptor undergoes conformational change upon dimerization. *Arch. Biochem. Biophys.* **475**, 25–35 (2008).
150. T. Shi, M. Niepel, J. E. McDermott, Y. Gao, C. D. Nicora, W. B. Chrisler, L. M. Markillie, V. A. Petyuk, R. D. Smith, K. D. Rodland, P. K. Sorger, W. J. Qian, H. S. Wiley, Conservation of protein abundance patterns reveals the regulatory architecture of the EGFR-MAPK pathway. *Sci. Signal.* **9** (2016), doi:10.1126/SCISIGNAL.AAF0891.
151. K. Yasuma-Mitobe, M. Matsuoka, The Roles of Coinhibitory Receptors in Pathogenesis of Human Retroviral Infections. *Front. Immunol.* **0**, 2755 (2018).
152. L. Chen, D. B. Flies, Molecular mechanisms of T cell co-stimulation and co-inhibition. *Nat. Rev. Immunol.* **13**, 227–242 (2013).
153. K. G. Anderson, I. M. Stromnes, P. D. Greenberg, Obstacles Posed by the Tumor Microenvironment to T cell Activity: A Case for Synergistic Therapies. *Cancer Cell*. **31**, 311–325 (2017).
154. C. Robert, A decade of immune-checkpoint inhibitors in cancer therapy. *Nat. Commun.* **11**, 1–3 (2020).
155. J. R. James, R. D. Vale, Biophysical mechanism of T-cell receptor triggering in a reconstituted system. *Nature*. **487**, 64–69 (2012).
156. O. Dushek, J. Goyette, P. A. van der Merwe, Non-catalytic tyrosine-phosphorylated receptors. *Immunol. Rev.* **250**, 258–276 (2012).
157. S. J. Davis, P. A. van der Merwe, The kinetic-segregation model: TCR triggering and beyond. *Nat. Immunol.* **7**, 803–809 (2006).
158. S. J. Davis, P. A. Van Der Merwe, The structure and ligand interactions of CD2: implications for T-cell function. *Immunol. Today*. **17**, 177–187 (1996).
159. V. T. Chang, R. A. Fernandes, K. A. Ganzinger, S. F. Lee, C. Siebold, J. McColl, P. Jönsson, M. Palayret, K. Harlos, C. H. Coles, E. Y. Jones, Y. Lui, E. Huang, R. J. C. Gilbert, D. Klenerman, A. R. Aricescu, S. J. Davis, Initiation of T cell signaling by CD45 segregation at “close contacts.” *Nat. Immunol.* **17**, 574–582 (2016).
160. K. Choudhuri, D. Wiseman, M. H. Brown, K. Gould, P. A. van der Merwe, T-cell receptor triggering is critically dependent on the dimensions of its peptide-MHC ligand. *Nature*. **436**, 578–582 (2005).
161. M. N. McCall, D. M. Shotton, A. N. Barclay, Expression of soluble isoforms of rat CD45. Analysis by electron microscopy and use in epitope mapping of anti-CD45R monoclonal antibodies. *Immunology*. **76**, 310 (1992).
162. G. R. Woollett, A. F. Williams, D. M. Shotton, Visualisation by low-angle shadowing of the leucocyte-common antigen. A major cell surface glycoprotein of lymphocytes. *EMBO J.* **4**, 2827–2830 (1985).

163. D. N. Garboczi, P. Ghosh, U. Utz, Q. R. Fan, W. E. Biddison, D. C. Wiley, Structure of the complex between human T-cell receptor, viral peptide and HLA-A2. *Nature*. **384**, 134–141 (1996).
164. K. C. Garcia, M. Degano, L. R. Pease, M. Huang, P. A. Peterson, L. Teyton, I. A. Wilson, Structural Basis of Plasticity in T Cell Receptor Recognition of a Self Peptide-MHC Antigen. *Science.* **279**, 1166–1172 (1998).
165. T. A. Springer, Adhesion receptors of the immune system. *Nature*. **346**, 425–434 (1990).
166. J. P. Landry, Y. Ke, G. L. Yu, X. D. Zhu, Measuring affinity constants of 1450 monoclonal antibodies to peptide targets with a microarray-based label-free assay platform. *J. Immunol. Methods*. **417**, 86–96 (2015).
167. J. J. Lin, G. P. O'Donoghue, K. B. Wilhelm, M. P. Coyle, S. T. Low-Nam, N. C. Fay, K. N. Alfieri, J. T. Groves, Membrane Association Transforms an Inert Anti-TCRβ Fab' Ligand into a Potent T Cell Receptor Agonist. *Biophys. J.* **118**, 2879–2893 (2020).
168. K. B. Wilhelm, S. Morita, D. B. McAffee, S. Kim, M. K. O'Dair, J. T. Groves, Height, but not binding epitope, affects the potency of synthetic TCR agonists. *Biophys. J.* (2021), doi:10.1016/J.BPJ.2021.08.027.
169. M. Iwashima, B. A. Irving, N. S. C. Van Oers, A. C. Chan, A. Weiss, Sequential interactions of the TCR with two distinct cytoplasmic tyrosine kinases. *J. Immunol.* **193**, 4279–4282 (2014).
170. T. J. Boggon, M. J. Eck, Structure and regulation of Src family kinases. *Oncogene*. **23**, 7918–7927 (2004).
171. L. M. L. Chow, M. Fournel, D. Davidson, A. Veillette, Negative regulation of T-cell receptor signalling by tyrosine protein kinase p50csk. *Nature*. **365**, 156–160 (1993).
172. H. Yamaguchi, W. A. Hendrickson, Structural basis for activation of human lymphocyte kinase Lck upon tyrosine phosphorylation. *Nature*. **384**, 484–489 (1996).
173. K. Nika, C. Soldani, M. Salek, W. Paster, A. Gray, R. Etzensperger, L. Fugger, P. Polzella, V. Cerundolo, O. Dushek, T. Höfer, A. Viola, O. Acuto, Constitutively Active Lck Kinase in T Cells Drives Antigen Receptor Signal Transduction. *Immunity*. **32**, 766–777 (2010).
174. J. R. Schoenborn, Y. X. Tan, C. Zhang, K. M. Shokat, A. Weiss, Feedback circuits monitor and adjust basal Lck-dependent events in T cell receptor signaling. *Sci. Signal.* **4** (2011), doi:10.1126/SCISIGNAL.2001893.
175. A. C. Bishop, J. A. Ubersax, D. T. Petsch, D. P. Matheos, N. S. Gray, J. Blethrow, E. Shimizu, J. Z. Tsien, P. G. Schultz, M. D. Rose, J. L. Wood, D. O. Morgan, K. M. Shokat, A chemical switch for inhibitor-sensitive alleles of any protein kinase. *Nature*. **407**, 395–401 (2000).
176. Y. X. Tan, B. N. Manz, T. S. Freedman, C. Zhang, K. M. Shokat, A. Weiss, Inhibition of the kinase Csk in thymocytes reveals a requirement for actin remodeling in the initiation of full TCR signaling. *Nat. Immunol.* **15**, 186–194 (2013).
177. H. Colin-York, Y. Javanmardi, M. Skamrahl, S. Kumari, V. T. Chang, S. Khuon, A. Taylor, T. L. Chew, E. Betzig, E. Moeendarbary, V. Cerundolo, C. Eggeling, M. Fritzsche, Cytoskeletal Control of Antigen-Dependent T Cell Activation. *Cell Rep.* **26**, 3369-3379.e5 (2019).

178. D. D. Billadeau, J. C. Nolz, T. S. Gomez, Regulation of T-cell activation by the cytoskeleton. *Nat. Rev. Immunol.* **7**, 131–143 (2007).
179. J. K. Burkhardt, E. Carrizosa, M. H. Shaffer, The Actin Cytoskeleton in T Cell Activation. *Annu. Rev. Immunol.* **26**, 233–259 (2008).
180. N. H. Roy, J. K. Burkhardt, The Actin Cytoskeleton: A Mechanical Intermediate for Signal Integration at the Immunological Synapse. *Front. Cell Dev. Biol.* **0**, 116 (2018).
181. K.-D. Fischer, Y.-Y. Kong, H. Nishina, K. Tedford, L. E. M. Marengère, I. Kozieradzki, T. Sasaki, M. Starr, G. Chan, S. Gardener, M. P. Nghiem, D. Bouchard, M. Barbacid, A. Bernstein, J. M. Penninger, Vav is a regulator of cytoskeletal reorganization mediated by the T-cell receptor. *Curr. Biol.* **8**, 554–562 (1998).
182. L. J. Holsinger, I. A. Graef, W. Swat, T. Chi, D. M. Bautista, L. Davidson, R. S. Lewis, F. W. Alt, G. R. Crabtree, Defects in actin-cap formation in Vav-deficient mice implicate an actin requirement for lymphocyte signal transduction. *Curr. Biol.* **8**, 563–573 (1998).
183. J. Riedl, A. H. Crevenna, K. Kessenbrock, J. H. Yu, D. Neukirchen, M. Bista, F. Bradke, D. Jenne, T. A. Holak, Z. Werb, M. Sixt, R. Wedlich-Soldner, Lifeact: a versatile marker to visualize F-actin. *Nat. Methods*. **5**, 605–607 (2008).
184. O. Acuto, F. Michel, CD28-mediated co-stimulation: a quantitative support for TCR signalling. *Nat. Rev. Immunol.* **3**, 939–951 (2003).
185. P. Riha, C. E. Rudd, CD28 co-signaling in the adaptive immune response. *Self. Nonself.* **1**, 231–240 (2010).
186. U. Khan, H. Ghazanfar, T Lymphocytes and Autoimmunity. *Int. Rev. Cell Mol. Biol.* **341**, 125–168 (2018).
187. J. A. Ditlev, A. R. Vega, D. V. Köster, X. Su, T. Tani, A. M. Lakoduk, R. D. Vale, S. Mayor, K. Jaqaman, M. K. Rosen, A composition-dependent molecular clutch between T cell signaling condensates and actin. *Elife*. **8** (2019), doi:10.7554/ELIFE.42695.
188. L. Wunderlich, A. Faragó, F. Faragó, J. Downward, L. ´ Aszí O Buday, Association of Nck with tyrosine-phosphorylated SLP-76 in activated T lymphocytes. *Eur. J. Immunol.* **29**, 1068–1075 (1999).
189. L. Malherbe, C. Hausl, L. Teyton, M. G. McHeyzer-Williams, Clonal Selection of Helper T Cells Is Determined by an Affinity Threshold with No Further Skewing of TCR Binding Properties. *Immunity*. **21**, 669–679 (2004).
190. D. G. Gibson, L. Young, R.-Y. Chuang, J. C. Venter, C. A. Hutchison, H. O. Smith, Enzymatic assembly of DNA molecules up to several hundred kilobases. *Nat. Methods*. **6**, 343–345 (2009).
191. E. Corse, R. A. Gottschalk, M. Krogsgaard, J. P. Allison, Attenuated T Cell Responses to a High-Potency Ligand In Vivo. *PLOS Biol.* **8**, e1000481 (2010).
192. A. D. Edelstein, M. A. Tsuchida, N. Amodaj, H. Pinkard, R. D. Vale, N. Stuurman, Advanced methods of microscope control using μManager software. *J. Biol. Methods*. **1**, e10 (2014).
193. J. Y. Tinevez, N. Perry, J. Schindelin, G. M. Hoopes, G. D. Reynolds, E. Laplantine, S. Y. Bednarek, S. L. Shorte, K. W. Eliceiri, TrackMate: An open and extensible platform for single-particle tracking. *Methods*. **115**, 80–90 (2017).

194. D. L. Ensign, V. S. Pande, Bayesian Detection of Intensity Changes in Single Molecule and Molecular Dynamics Trajectories. *J. Phys. Chem. B*. **114**, 280–292 (2009).